Development of advanced optical diagnostics for the study of ultrafast kinetics of oxygen production by nanosecond discharges in atmospheric pressure air

Farah Kaddouri

ÉCOLE CENTRALE DES ARTS ET MANUFACTURES « ÉCOLE CENTRALE PARIS »

THÈSE

présentée par

Melle. Kaddouri Farah

pour l'obtention du

GRADE DE DOCTEUR

Spécialité : Energétique

Laboratoire d'accueil : Laboratoire Energétique Moléculaire et Macroscopique, Combustion (EM2C), CNRS UPR 288

SUJET : ***Développement de diagnostics optiques avancés pour l'étude de la cinétique ultrarapide de production d'oxygène par décharge nanoseconde dans l'air à pression atmosphérique***

Development of advanced optical diagnostics for the study of ultrafast kinetics of oxygen production by nanosecond discharges in atmospheric pressure air

soutenue le : ***26 Septembre 2011***

Devant un jury composé de :

Mme. DESGROUX Pascale	Directrice de Recherche CNRS à l'Université de Lille
M. GHERARDI Nicolas	Chargé de Recherche CNRS au LAPLACE, Toulouse
Melle. LACOSTE Deanna	Ingénieur de Recherche CNRS à l'ECP
M. LAUX Christophe	Professeur Ecole Centrale Paris
M. MACHALA Zdenko	Professeur à l'Université Comenius de Bratislava
M. ODIC Emmanuel	Professeur à SUPELEC
M. STANCU Gabi	Maître de Conférences à l'ECP

A mes très chers parents,
A Samar.

Résumé

Les plasmas à pression atmosphérique sont en constant développement en raison de leur capacité à produire efficacement des espèces actives pour des applications variées comme la combustion assistée par plasma, le contrôle d'écoulements aérodynamiques, la biodécontamination, la synthèse de nanomatériaux ou encore le traitement de surfaces. Au cours de la dernière décennie, les décharges Nanosecondes Répétitives Pulsées (NRP) ont connu un vif succès car elles permettent de produire des densités élevées d'électrons et d'espèces actives avec une efficacité énergétique inégalée dans l'air à la pression atmosphérique.

Cette thèse concerne plus particulièrement l'effet des décharges NRP en combustion assistée par plasma. En effet, les décharges NRP permettent l'utilisation de flammes pauvres, qui produisent moins de NO_x et qui sont par conséquent moins polluantes. Ainsi, plusieurs études ont mis en évidence l'effet significatif des décharges NRP dans la réduction des délais d'allumage ou la stabilisation de mélanges air/carburant pauvres prémélangés. Cependant, peu d'entre elles se sont intéressées au mécanisme d'action de la décharge.

Cette étude est focalisée sur les décharges dans l'air car celles-ci produisent des électrons libres, et espèces excitées et des radicaux, notamment l'oxygène atomique, dont la concentration et l'évolution temporelle ont une influence importante sur la combustion. Nous nous sommes attachés en particulier à étudier le mécanisme cinétique de production de l'oxygène atomique, dit mécanisme « à deux étapes » ou « ultrarapide ». La première étape de ce mécanisme correspond, sur une durée de l'ordre de 10 ns correspondant à la durée d'une impulsion de tension, à l'excitation par impact électronique des états électroniques du diazote (états $A^3\Sigma_u^+$, $B^3\Pi_g$, $C^3\Pi_u$). Puis, dans une deuxième étape, aussi de l'ordre de quelques dizaines de nanosecondes à la pression atmosphérique, les molécules excitées d'azote dissocient l'oxygène, l'excès d'énergie étant converti en chauffage du gaz. En raison de son caractère extrêmement rapide à la pression atmosphérique, ce mécanisme n'a pas été étudié expérimentalement à ce jour.

Un objectif majeur de cette thèse est donc d'étudier l'importance potentielle du mécanisme à deux étapes dans une décharge NRP appliquée à un écoulement d'air à la pression atmosphérique et préchauffé à des températures proches de celles rencontrées dans les applications telles que la

combustion assistée par plasma. Pour cela, différents diagnostics optiques, résolus en temps et en espace sur des échelles de l'ordre de la nanoseconde et de la centaine de micromètres ont été mis en place. Dans un premier temps, les densités des états excités N_2 (B) et N_2 C) ont été déterminées par spectroscopie d'émission quantitative avec une résolution temporelle d'environ 2 ns. Ces densités présentent des valeurs maximales respectives de $5x10^{16}$ et $6x10^{15}$ cm^{-3}, environ 8 ns après le début d'une impulsion. L'état N_2 (A), métastable et donc faiblement radiatif, n'a pu être mesuré par spectroscopie d'émission. Il a donc été nécessaire de faire appel à une technique de détection beaucoup plus sensible, la spectroscopie d'absorption en cavité résonante, plus connue sous le nom de Cavity Ring-Down Spectroscopy ou CRDS. Cette technique a permis d'obtenir la densité moyenne de N_2 (A) sur une durée de 100 ns à partir du début d'une impulsion de tension. La densité moyenne obtenue est d'environ 10^{14} cm^{-3}. Enfin, l'évolution temporelle de la densité d'oxygène atomique a été déterminée par une méthode de fluorescence laser à deux photons (Two-Photon Absorption Laser-Induced Fluorescence ou TALIF), calibrée en valeur absolue au moyen d'une cellule de référence contenant du xenon. La densité d'oxygène atomique a été obtenue avec une résolution temporelle de 7 ns. On a noté jusqu'à 50% de dissociation de l'oxygène moléculaire. Par ailleurs, l'élévation de la température du gaz liée au mécanisme à deux étapes a également été déterminée par spectroscopie d'émission sur les spectres rotationnels de la transition du deuxième système positif de l'azote.

Les résultats obtenus indiquent que l'évolution temporelle de la densité des états excités de l'azote coïncide parfaitement, aux incertitudes expérimentales près, avec l'évolution temporelle de la production de l'oxygène atomique. En outre, l'élévation de température mesurée (environ 1000 K), liée au caractère exothermique des réactions de dissociation de O_2 par les états électroniques excités de N_2, est également en très bon accord avec les prédictions numériques obtenues avec le mécanisme à deux étapes. Les travaux de cette thèse ont donc permis d'obtenir pour la première fois une confirmation expérimentale du mécanisme à deux étapes proposé dans la littérature. A pression atmosphérique, ce mécanisme permet de dissocier plus de 50% de l'oxygène et de chauffer le gaz d'environ 1000 K sur une durée inférieure à quelques dizaines de nanosecondes.

L'efficacité énergétique de ce mécanisme ultrarapide a été déterminée au moyen de mesures électriques de tension et de courant qui ont permis d'estimer l'énergie déposée par chaque impulsion. L'efficacité de dissociation de l'oxygène est estimée à environ 30-40%, et l'efficacité de chauffage à environ 13-20%. Le mécanisme ultrarapide semble donc être une voie prometteuse pour

toutes les applications requérant la production efficace d'oxygène atomique ou un processus de chauffage ultrarapide. En résumé, les travaux de cette thèse ont permis de caractériser et de mieux comprendre les décharges nanoseconde répétitives pulsées dans l'air à pression atmosphérique et de caractériser la production des espèces actives en vue de leur utilisation dans de nombreuses applications industrielles.

Abstract

Plasmas at atmospheric pressure are increasingly developed because of their capacity to efficiently produce active species for various applications such as plasma-assisted combustion, flow control, bio-decontamination and surface treatment. In the last decade, nanosecond repetitively pulsed discharges (NRPD) had became very popular, because they allow to produce high electron densities and active species for an energy efficiency unequaled in air at atmospheric pressure.

This thesis targets more particularly the effect of the NRP discharges in view of applications in plasma-assisted combustion. NRP discharges can stabilize low temperature flames, which produce fewer NO_x and are consequently less polluting. Thus, several studies have brought to light the significant effect of NRP discharges in the reduction of the ignition time or in the stabilization of the fuel / air lean mixtures. Nevertheless, few studies have investigated the mechanism of action of the plasma on flames.

This study is focused on air discharges, because they produce free electrons, excited species and radicals, especially atomic oxygen whose concentration and time evolution have a great influence in combustion.

We have studied more specifically the kinetic mechanism of the atomic oxygen production, known as "two-step" or "ultrafast" mechanism. The first step of this mechanism corresponds, on a time scale of 10 ns which represents the voltage pulse duration, to the electron impact excitation of the nitrogen electronic states (states $A^3\Sigma_u^+$, $B^3\Pi_g$, $C^3\Pi_u$).

Then, in a second step, of duration of tens of nanoseconds at atmospheric pressure, the excited nitrogen molecules dissociate oxygen, the excess in the energy of this process being converted into gas heating. Because these processes are fast at atmospheric pressure, this mechanism has not been studied quantitatively to date .

A major goal of this thesis is to study the potential importance of the two-step mechanism for NRP discharges applied to an air flow at atmospheric pressure preheated to temperatures close to the ones met in applications such as the plasma-assisted combustion.

To this end, various optical diagnostic techniques, with time and space resolution of nanoseconds and hundreds of micrometers, have been set up.

First, densities of the excited states $N_2(B)$ and $N_2(C)$ have been determined by quantitative emission spectroscopy with a time resolution of about 2 ns. These densities present maximum values of $5x10^{16}$ and of $6x10^{15}$ molecules per cm^3 about 8 ns after the pulse. The $N_2(A)$ state is a

metastable state, and therefore it radiates weakly and cannot be easily measured by emission spectroscopy. It was thus necessary so, to use a more sensitive detection technique, Cavity-Ring Down Spectroscopy (CRDS). This technique allowed us to measure a density of $N_2(A)$ averaged over 100 ns starting from the beginning of the voltage pulse. This averaged density was found to be on the order of $10^{14}cm^{-3}$. Finally the time evolution of the density of atomic oxygen was determined by Two-Photon Absorption Laser Induced Fluorescence or TALIF, calibrated in absolute value using a reference xenon cell. The density of atomic oxygen was obtained with a time resolution of 7 ns. We measured up to 50 % of dissociation of molecular oxygen. In addition, an increase of the gas temperature related to the two-step mechanism was determined by emission spectroscopy of the rotational spectra of the nitrogen second positive system.

The results indicate that the temporal evolution of the nitrogen excited state densities coincide, within the range of experimental uncertainties, with the time evolution of the production of atomic oxygen. Moreover, the increase in the measured temperature (about 1000 K) is well explained by the exothermic reactions of O_2 dissociation by the nitrogen excited states, and these add further support to the two-step mechanism. Thus the work of this thesis represents the first experimental confirmation of the two-step mechanism suggested in the literature. At atmospheric pressure, this mechanism is found to dissociate up to 50 % of molecular oxygen and heats the gas by about 1000 K.

The energy efficiency of this ultrafast mechanism has been determined using electrical measurements of the voltage and the current to estimate the energy deposited per pulse. The efficiency of oxygen dissociation is estimated to be about 30-40%, and the efficiency of gas heating is about 13-20%. The ultrafast mechanism seems to be a promising way for all the applications that require an efficient production of atomic oxygen or an ultrafast heating process. As a summary, the work of this thesis allowed characterizing and better understanding nanosecond repetitively pulsed discharges in the air at atmospheric pressure and determining the production on the key active species, atomic oxygen.

Table of contents

Introduction

Ionized gases, particularly plasmas, are very rich in terms of chemistry. They are mainly composed of electrons, ions, excited atoms and molecules, radicals and metastables. This type of medium presents a high reactivity, which makes it ideal for a wide range of applications. In particular, air plasmas at atmospheric pressure are employed in many applications such as plasma-assisted combustion, aerodynamic flow control, bio-decontamination and surface treatment (Becker et al, 2004)

Among the large number of applications of this type of plasmas, the applications related to environmental issues are today one of major societal interest. In this work, our interest was directed to plasma-assisted combustion for the reduction of pollutant emissions. Indeed, new engine development is becoming increasingly subject to strict pollution regulations and to the need to reduce fuel consumption. Obtaining the best compromise between a decrease in toxic emissions and an increase in engine power output without raising production costs becomes a major challenge.

One of the possibilities allowing the reduction of these pollutants consists in using lean premixed combustion systems. However, these systems lead to other problems, such as the occurrence of flame extinction and combustion instabilities, which causes major difficulties for the operation of combustion chambers and poses reliability problems. To resolve these problems, it was shown (Kim et al , 2007) that lean combustion can be enhanced by a local addition of energy that allows a stabilization of the flame by modifying the thermal and reactive mechanisms.

The use of high voltage nanosecond repetitively pulsed (NRP) discharges represents a promising method as an answer to this need since these discharges can produce high electron number densities in atmospheric pressure air with a reduced applied power. Several studies have evidenced that the use of NRP discharges has a significant effect in reducing the ignition delay time in air / fuel mixture (Starikovskyi, 2005. Pancheshnyi et al, 2006). However, fewer studies have focused on plasma- assisted flame stabilization and its mechanism (Qin et al, 2000). In order to understand how NRP discharges improve the combustion process, it is necessary to know what are the active species produced by the discharge, what are their production mechanisms, and how these key species are transported and react in the combustion chamber.

The objective of the present study is to better understand the plasma physics and chemistry generated by NRP discharges in air at atmospheric pressure. To this end; we have investigated the main channels of production of the key species, measured their densities, the gas temperature, and energy deposited by the discharge. For this purpose, advanced optical diagnostics have been implemented and developed and electrical measurements have been performed.

Following the results obtained using a kinetic model (Popov, 2001), it was predicted that atomic oxygen, which is a key species in the combustion process, is produced through a two-step mechanism by the NRP discharges. According to this mechanism, electronically excited molecular nitrogen formed via electron-impact excitation dissociates molecular oxygen, thus generating atomic oxygen which can oxidize the fuel. Our research has thus focused on the experimental validation of the two-step mechanism for atomic oxygen production.

The investigation and the validation of this mechanism encountered several experimental challenges because :

- the diagnostics used must be non-intrusive and *in situ*, in order to avoid perturbation of the discharge and to be able to follow reaction paths;

- the kinetic and dynamic processes are very fast at atmospheric pressure, therefore the development and implementation of diagnostics with nanosecond temporal resolution is required;

- the high electromagnetic (EM) noise generated by the discharge perturbs the diagnostics, and thus adequate EM shielding is necessary;

- the small discharge volumes, of about 1-2 mm^3, require sub-mm spatial resolution;

- in addition, it is necessary to implement complex synchronization schemes of the discharge with the lasers and the spectrometers.

We started our study by characterizing electrically the discharge. For this, measurements of the discharge voltage and current and determination of the energy deposited per pulse were performed. Then, time-resolved Optical Emission Spectroscopy (OES) diagnostics were made to determine the absolute density evolution of the excited molecular nitrogen states $N_2(B)$ and $N_2(C)$. Next, a Cavity Ring-Down Spectroscopy (CRDS) technique was developed to evaluate the density of the metastable state of molecular nitrogen: $N_2(A)$. In addition, time-resolved Two-photon Absorption Laser Induced Fluorescence (TALIF) was used to measure the evolution of the ground state oxygen density. And finally, we measured

the gas temperature evolution during the two-step mechanism, to determine the degree of heat release during the discharge.

The thesis is structured in five chapters as described in the following. Chapter 1 contains a detailed bibliographic review of the recent work in the field of plasmas, selecting the ones relevant to the present research. The focus is on the fundamental aspects of gas discharge plasmas (GDP), atmospheric non-thermal plasmas (ANTP) and the nanosecond repetitively pulsed (NRP) discharges. Chapter 2 deals with the basic principles of the diagnostics used in the thesis. It includes the principle of optical emission spectroscopy (OES), cavity ring-down spectroscopy (CRDS) and two-photon absorption laser-induced fluorescence (TALIF). Chapter 3 describes the experimental set-ups used during the studies conducted in this thesis. This chapter details the technical aspects of the discharge and the diagnostics used. In chapter 4, the main results of the thesis are presented and discussed. The conclusion and perspectives for future investigations are presented in the last part of this work.

The research performed in this thesis has been supported by the Agence Nationale de la Recherche (IPER and PREPA projects) and by the Ministère de l'Enseignement Supérieur et de la Recherche (Chaire d'Excellence programme).

Chapter 1. Atmospheric pressure plasmas and applications

1.1 Fundamental aspects of Gas Discharge Plasmas (GDP)

Plasma is a quasi neutral ionized gas that may contain positive and negative ions, electrons, free radicals, metastables, as well as atoms and molecules in the ground and in excited states (see figure 1.1). Transitions from excited states lead to the production of photons.

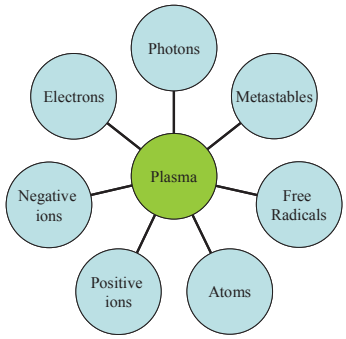

Figure 1.1. Major plasma constituents

Generally, plasmas can be divided into two groups: the high temperature or fusion plasmas and the low temperature or gas discharges. Based on the relative temperatures of the electrons, ions and neutrals, low temperature plasmas are classified as "thermal" or "non-thermal". In thermal plasmas, the electrons, ions and heavy particles have the same temperature, i.e. they are in thermal equilibrium with each other. In non-thermal plasmas, on the other hand, ions and neutrals are at a much lower temperature, (typically room temperature) than electrons. In a more general picture plasmas can be classified according to electron densities and temperatures as shown in figure 1.2.

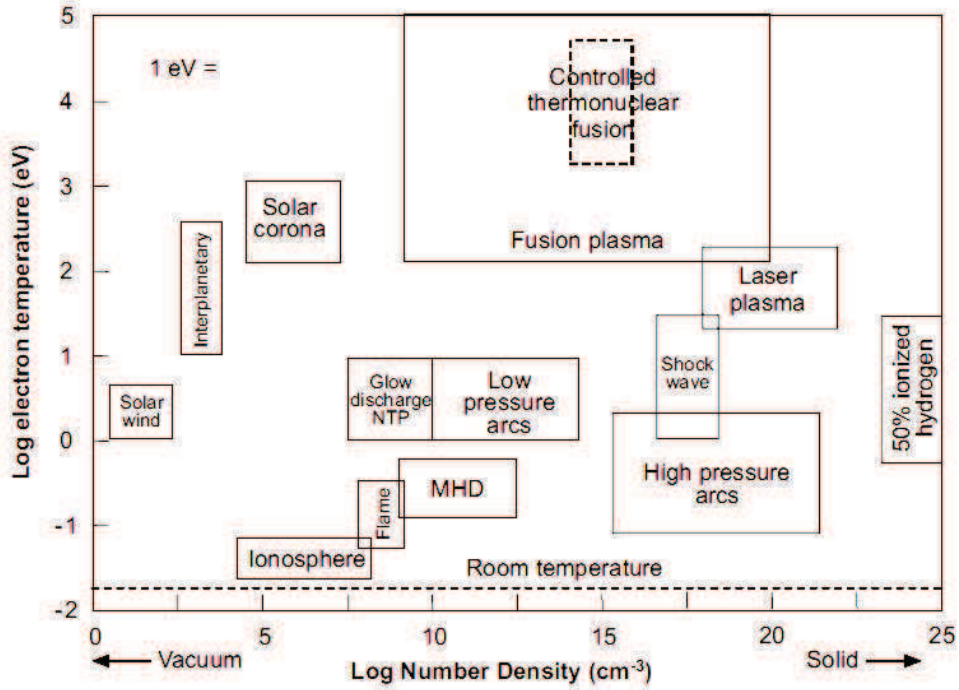

Figure 1.2. Plasma classification depending on electron density and temperature (Kong *et al*., 2006)

Thermal plasmas are characterized by thermal equilibrium, or close equality between electrons, ions and neutrals temperatures. Stationary thermal plasma are generally produced using plasma torches (DC or RF) or microwave devices. A high flux of heat is produced by these sources which are principally used in areas such as in plasma material processing and plasma treatment of waste materials. Even the heaviest wastes including solids, toxic, medical, industrial and nuclear waste, can be processed by high temperature thermal plasmas into smaller fragments such as atoms and small molecules, finally diminishing environmental pollution. However, the high temperature characteristics are not required or desired for a certain number of technological applications such as the treatment of surfaces. It is even prohibited in some cases such as biological tissue plasma treatment where cold plasmas are more appropriate.

In cold plasmas, most of the electrical energy is first coupled to electrons, producing, by that means, energetic electrons instead of heating the whole gas stream; while the plasma ions and neutral components remain at or close to room temperature.

Because the ions and the neutrals remain rather cold, this gives the possibility to use cold plasmas for low temperature plasma chemistry and for the treatment of heat sensitive materials including polymers and biological tissues. The characteristics of

cold plasmas, for example their strong thermodynamic nonequilibrium nature, the low gas temperature, the presence of reactive chemical species and high selectivity make them of great interest for a large range of applications, such as those mentioned previously.

The chemistry occurring in plasma is generally rather complex and involves many reactions (Becker *et al*., 2005). The basic chemical reactions occuring in air plasmas (Kossyi *et al*., 1992) are presented below. Homogeneous and heterogeneous reactions are the principal types of reactions taking place. Homogeneous reactions take place between species in the gaseous phase, resulting from inelastic collisions between electrons and heavy species or collisions between heavy species. Heterogeneous reactions occur between the plasma species and the solid surface immersed or in contact with the plasma. They are especially important in the processing of semiconductor materials. Examples of important homogeneous and heterogeneous reactions in air plasmas are given in Tables 1 and 2.

Table 1. Typical gas phase reactions in air plasmas (M=N_2, O_2, NO, N, O, e, …)

(1) Nitrogen species

Ionization/recombination: $N_2 + M \leftrightarrow N_2^+ + e + M$

Dissociation/recombination: $N_2 + M \leftrightarrow 2N + M$

Dissociative recombination/associative ionization: $e + N_2^+ \leftrightarrow N + N$

Electronic excitation: $N_2 + M \leftrightarrow MN_2^* = N_2$ (A, B, C, ...)

Vibrational excitation: N_2 (v) + M $\leftrightarrow$ N_2 (v'>v) + M

(2) Oxygen species

Ionization/recombination: $O_2 + M \leftrightarrow O_2^+ + e + M$

Dissociation/recombination: $O_2 + M \leftrightarrow 2O + M$

Dissociative attachment: $e + O_2 \leftrightarrow O^- + O$

Three-body attachment: $e + O_2 + M \leftrightarrow O_2^- + M$

Ion-ion recombination: $O^- + O_2^+ \leftrightarrow O + O_2$

Dissociative recombination: $e + O_2^+ \leftrightarrow O + O$

Electronic excitation: $O_2 + M \leftrightarrow MO_2^*$

Table 2. Examples of surface reactions in plasma (Nehra *et al*., 2008)

Surface Process	Reactions	Description
Etching	$AB + C_{solid} \rightarrow A + BC_{vapour}$	Material erosion
Adsorption	$M_g + S \rightarrow M_s$ $R_g + S \rightarrow R$	Molecules or radicals from a plasma come in contact with a surface exposed to the plasma and are adsorbed on the surface
Deposition	$AB \rightarrow A + B$	Thin film formation

1.2 Atmospheric non-thermal plasmas

Although low pressure discharge plasmas are extensively used in the microelectronics industry and materials technology, or in fundamental research, operation at low pressure requires the use of costly air tight enclosures, such as massive vacuum reactors. In addition, the density of active particles is relatively low and processing times tend to be long. For these reasons, significant efforts have been placed recently on the development of new plasma sources capable of operating at atmospheric pressure while maintaining the benefits of low pressure media.

Non-thermal atmospheric pressure plasmas can be obtained by various electrical discharges such as corona discharges, microhollow cathode discharges (MHCD), atmospheric pressure plasma jets (APPJ), gliding arc discharges, Atmospheric Uniform Glow Discharges (AUGD), Dielectric Barrier Discharge (DBD), plasma needles, etc. They all have important technological applications. Table 3 shows some characteristics of these atmospheric plasma sources:

Table 3. Characteristics of various atmospheric plasma sources (Nehra *et al*., 2008)

Parameters	Corona discharge	DBD	APPJ
Method and Type	Sharply pointed electrode	Dielectric barrier cover on electrodes	RF capacitively coupled
Electron Density, cm^{-3}	10^{9}-10^{13}	10^{12} -10^{15}	10^{11}-10^{12}
Temperature T (K)	300	Average gas Temp (300)	400

1.3 Plasmas sources in air atmospheric pressure

We will now review three types of atmospheric non-thermal plasma discharges: DBD, DC, NRP and we will compare their main characteristics in terms of gas temperature and power consumption.

1.3.1. Dielectric Barrier Discharges

Dielectric barrier discharges (DBD) represent a convenient method to generate large-volume non-thermal plasma at atmospheric pressure without expensive vacuum equipments

Development of the understanding of the homogeneous form of DBD was presented by different groups (Massines *et al*., 1998; Kogelschatz *et al*., 1999). DBD's are used in many applications (Chirokov *et al*., 2005), with earlier applications forcused on ozone production, and then on surface treatment and plasmas screens (Boeuf *et al*., 2003)

These discharges are generated at atmospheric pressure in air when ac voltage waveforms or repetitive pulses are applied between two electrodes separated by a dielectric. In air at atmospheric pressure, the gap between the electrodes is typically limited to a few millimetres. In the example illustrated in the figure 1.3, we see that the atmospheric air DBD produced by a repetitive nanosecond-pulse pulse generator is created between two circular plane-parallel aluminium electrodes of 50 mm in diameter. The experiments are carried out with voltage amplitudes from 15-22.5 kV and with air

gap spacing ranging from 1-3 mm. The presence of the insulator between the electrodes prevents the development of arcs.

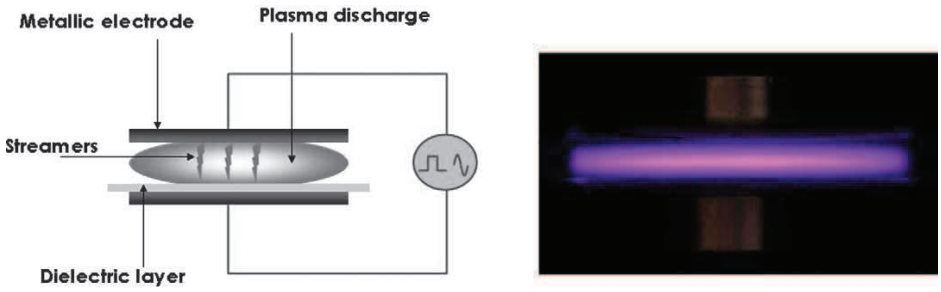

Figure 1.3. Typical setup for DBD discharge (Shao *et al*, 2011)

In recent years, DBD discharges have considered for medical purposes where they are applied to treatment of living cells and tissues (Gutsol, 2005; Peddinghaus *et al*., 2005). These plasmas can be applied directly to a living human tissue, as shown in figure 1.4. In this figure, the plasma is produced between the human tissue, which can be considered as a charge-storage medium, called a Floating Electrode (FE) and the insulated electrode. The effect in tissue treatment is attributed to the active species, radicals, and ultraviolet radiation produced by the discharge. One important point to notice here is that this work clearly shows that the Floating-electrode-DBD generates a non-thermal plasma sustainable at room temperature.

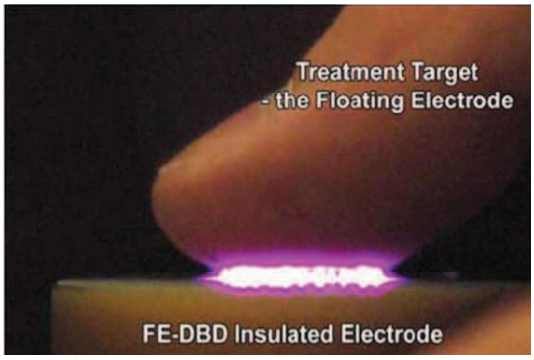

Figure 1.4. Floating electrode DBD applied to living tissue (Peddinghaus *et al*., 2005)

1.3.2. DC discharges

Non-thermal DC discharges are notoriously difficult to obtain in atmospheric pressure, room temperature air, because of their propensity to transition to thermal arcs. In the late 1990s, the Stanford group studied the potential of DC discharges to produce non-thermal plasmas in atmospheric pressure air preheated to 2000 K (Yu *et al*., 2002). Non-thermal discharges were successfully obtained by using ballast resistors to limit the current and a high speed air flow to prevent thermal heating of the flow. Figure 1.5 shows such a discharge obtained between two pin electrodes separated by a distance of 3.5 cm, with a DC discharge voltage of 5.2 kV and discharge current of 200 mA (Yu *et al*., 2002). Figure 1.5 shows images of the DC discharge in a preheated (2000 K) air plasma plume. The electron density measured in the discharge region (bright zone in Figure 1.5b) was found to be about 10^{12} cm^{-3}, i.e. 6 orders of magnitude higher than in equilibrium air at 2000 K. Thus, the discharge was clearly non thermal.

Additional experiments were also conducted by Machala *et al*. (2004), using various electrode configurations and using swirled gas flows, allowing obtaining these types of non-thermal DC discharges on even larger volumes.

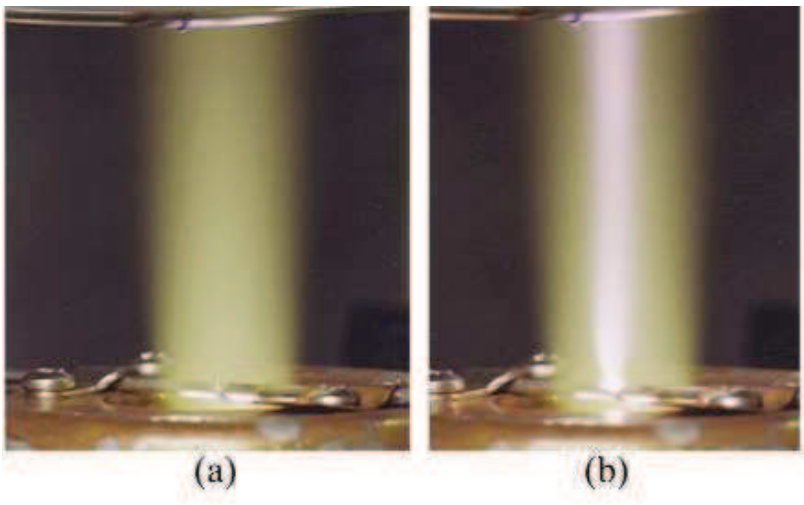

Figure 1.5. Air plasma at 2000 K a) without discharge, b) with DC discharge of 1.4 kV/cm, 200 mA (Yu *et al*., 2002).

A model was developed (Laux *et al*., 1999) taking into account a two

temperature kinetic model of the main reactions taking place in the air discharge. A comparison of the predicted and measured electric fields as a function of the current density, for a gas temperature varied between 1800 and 3000 K is shown in Figure 1.6. As can be seen, good agreement is obtained between the simulations and the experimental values.

Based on this model, the power required to obtain a given electron density can be inferred: the power is obtained by multiplying the current density by the electric field, and the electron density is obtained from the current density, as explained by Ishihara *et al.*, 2005. The results are shown in Figure 1.7. Thus, although it is possible to obtain non thermal air plasmas with DC discharges in air, the power requirements are extremely high. Alternate methods of plasma generation were therefore sought, providing the motivation for the study of Nanosecond Repetitively Pulsed discharges, as discussed in the next subsection.

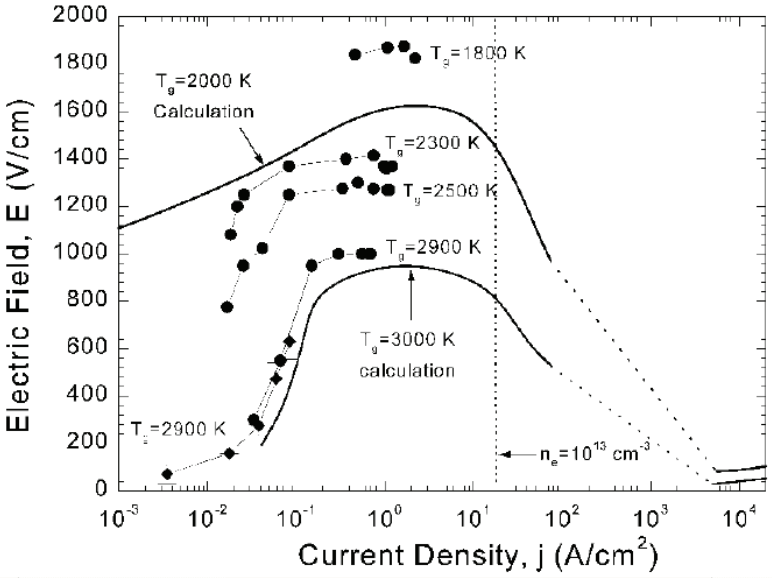

Figure 1.6 Measured (symbols) and predicted (solid lines) characteristics of DC discharges in preheated air at atmospheric pressure (Laux *et al.*, 1999, Ishihara *et al.*, 2005, Sharer *et al.*, 2005).

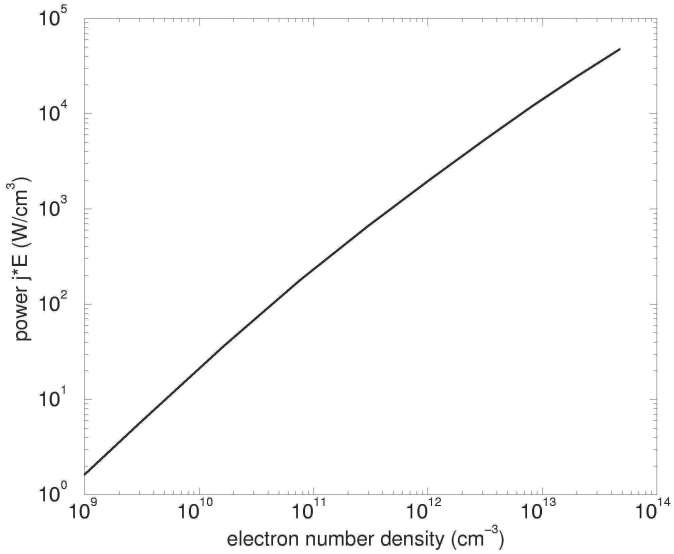

Figure 1.7 Predicted power requirements to produce a non-thermal DC discharge in atmospheric pressure air preheated to 2000 K (Ishihara *et al*., 2005).

1.3.3. Nanosecond Repetitively Pulsed Discharges

In the early 2000's, the Stanford plasma group proposed another technique to produce elevated electron number densities in atmospheric pressure air plasmas preheated at 2000 K. This technique is based on the use of Nanosecond Repetitively Pulsed (NRP) discharges. The principle is to apply short (about 10 ns), high voltage (~10 kV) pulses to ionize the gas efficiently, and at repetition rates high enough (10-100 kHz) so that the electron density does not decay too much between two consecutive pulses. This strategy is illustrated in Figure 1.8. The average electron density obtained with this method depends on the pulse duration, pulse voltage, and the interval between pulses.

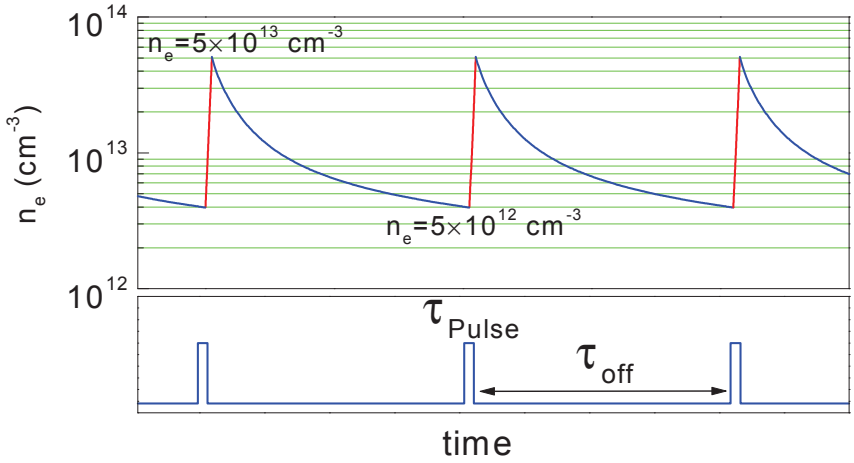

Figure 1.8. Nanosecond Repetitively Pulsed discharge principle

An example of such an NRP discharge in air preheated at 2000 K is shown in the photograph of figure 1.9 (Kruger *et al.*, 2002, Packan, 2003). Figure 1.9 shows the measured temporal variations of the electron density during three cycles of the pulsed discharge. The electron number density varies from $7x10^{11}$ to $1.7x10^{12}$ cm^{-3}, with an average value of about 10^{12} cm^{-3}. The power deposited into the plasma by the repetitive discharge was determined from the pulse current (measured with a Rogowski coil), the voltage between the electrodes (6 kV peak) minus the cathode fall voltage (measured to be 1525 V by varying the gap distance), and the measured discharge diameter. The peak pulse current was 240 mA. The power deposited is found to be 12 W/cm^3, consistent with the theoretical value of 9 W/cm^3 for an optimized pulsed discharge producing 10^{12} electrons/cm^3. It is lower, by a factor of 250, than the power of 3000 W/cm^3 required to sustain 10^{12} electrons/cm^3 with a DC discharge. More details about these experiments and modelling can be found in Packan (2003) and Sharer *et al.* (2005).

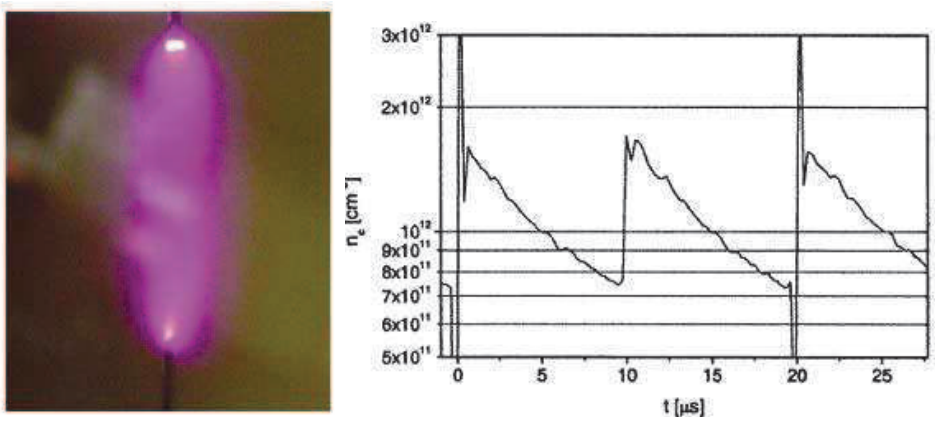

Figure 1.9 Photograph of a Nanosecond Repetitively Pulsed discharge in air at 2000 K, 1 atm (left) and temporal evolution of the measured electron number density . Gap distance: 1 cm, Peak voltage: 6 kV, Pulse Repetition Frequency: 100 kHz (Kruger *et al*., 2002, Packan, 2003).

In summary, Figure 1.10 summarizes the power reductions afforded by NRP discharges relative to DC discharges (Packan, 2003). The experimental point represents the measured power requirement of the NRP experiment presented in the foregoing. Power budget reductions by an additional factor of about 5 are possible with repetitive pulses of 1 nanosecond duration. Such repetitive pulsers are already commercially available. Therefore, power budget reductions by a factor of 250-1000 relative to the DC case at 10^{12} electrons/cm^3 can be readily obtained with a repetitively pulsed technique.

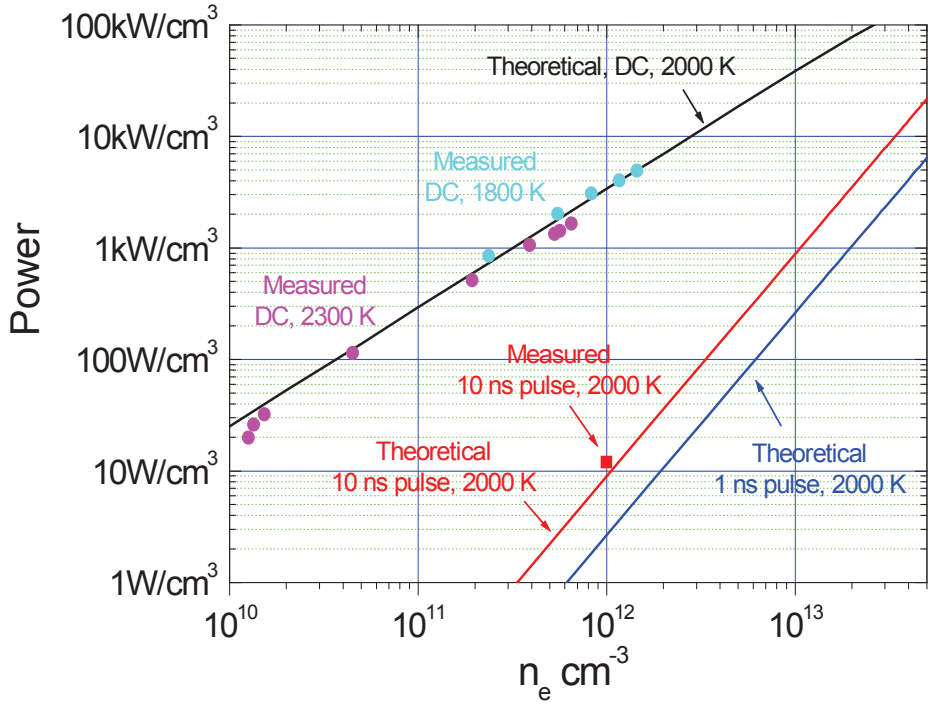

Figure 1.10. Power requirements vs. electron number density for DC and pulsed discharges in air at 1 atm, 2000 K (Packan, 2003, Sharer *et al.*, 2005).

1.3.4. Comparison of various discharges

In his thesis Pai (2010) compared the power requirements of the various types of discharges used to produce air plasmas, as well as the temperature range of operation of these discharges. The results are shown in Figures 1.11 and 1.12. As pointed out by Pai, Nanosecond Repetitively Pulsed (NRP) discharges are the only experimentally proven method to provide high electron number densities together with low power consumption in non-thermal plasmas. As mentioned by Pai, the only more efficient technique is to use an electron beam. However, the latter present an important technological limitation at present: to produce e-beam discharges, accelerated electrons have to pass through a electron transparent windows, under vacuum conditions, to the gas discharge at atmospheric pressure. Owing to thermal dissipations, the window heats up, leading to breakage. Active cooling methods are currently being investigated to circumvent this limitation. Until then, NRP discharges present the best compromise to obtain a high electron number density, and thus a high amount of active species, with low energy consumption.

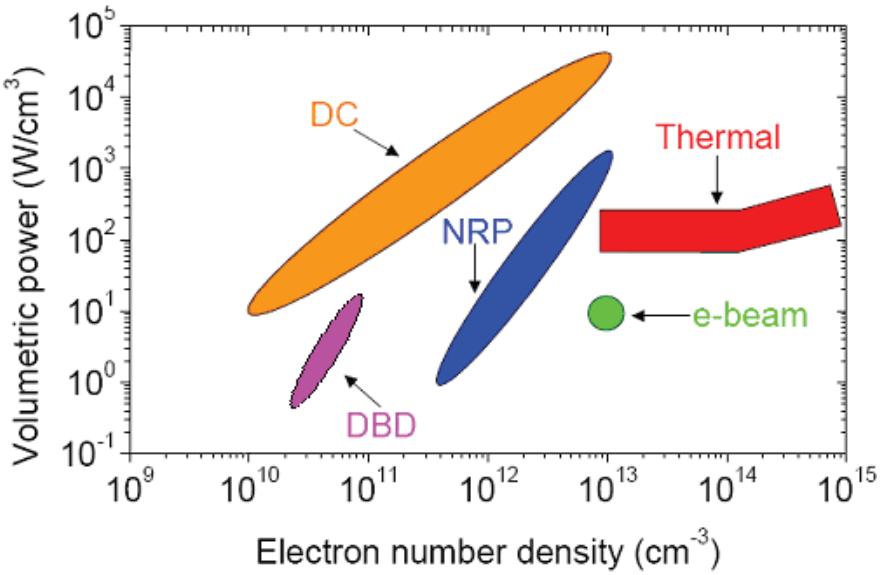

Figure 1.11 Power budgets of plasmas produced by different plasma sources as a function of electron number density (Pai, 2010).

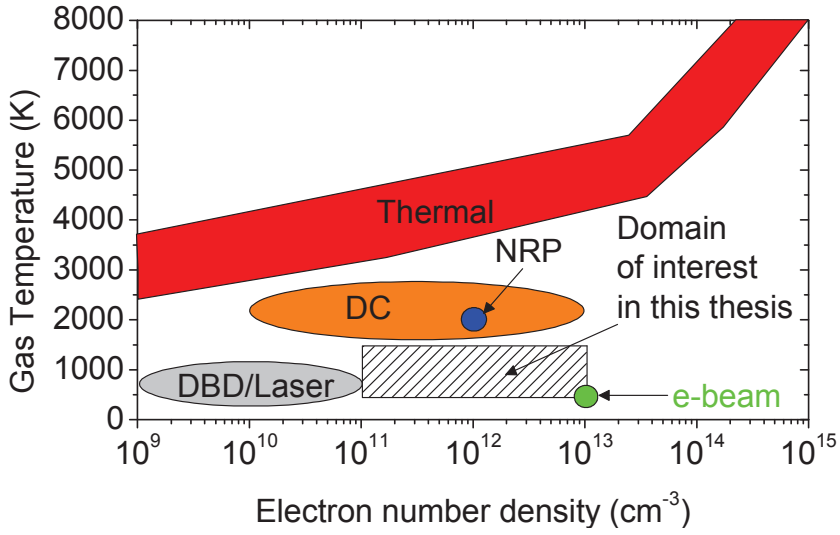

Figure 1.12. Gas temperatures of plasmas generated by various plasma discharges as a function of electron number density.

In light of the high potential of NRP discharges to produce elevated electron number densities at low power budget in low temperature, atmospheric pressure air, the

Ecole Centrale Plasma Group has sought to extend the applicability of these discharges to temperatures lower than the 2000 K value investigated at Stanford. During his Ph.D. thesis, Pai demonstrated that such discharges can be obtained at temperatures down to 700 K, and he proposed a criterion relating the various discharge parameters (voltage, pulse duration, pulse repetition frequency, gap distance, electrode radius of curvature) allowing to determine under which parameters these discharges can be obtained at room temperature (Pai 2009, Pai 2010a).

He also demonstrated that three NRP regimes can be obtained at atmospheric pressure. In order of increasing voltage, these regimes can be defined as the NRP Corona, NRP Glow, and NRP Spark as shown in figure 1.13. Their main characteristics are summarized in Table 4. The NRP glow regime is found to allow a higher energy deposition than the corona regime, without heating the gas. The spark regime provides even higher energy deposition, but it may significantly heat the gas. These characteristics make the glow an interesting regime for applications where gas heating is not tolerable (for example, sensitive tissue treatment). In the plasma-assisted combustion application discussed next, only the spark regime is found to have a significant effect.

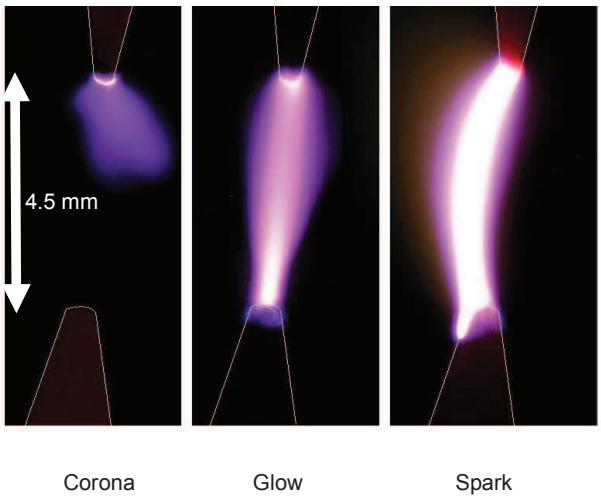

Figure 1.13. Images of the NRP corona, glow, and spark regimes in 1-atm air with T_g=1000 K, *PRF*=10 kHz, *d*=4.5 mm. The anode and cathode are at the top and bottom, respectively, and are outlined in white. From left to right, the images are in order of increasing applied voltage (5, 5.5, and 6 kV, respectively). (Pai, 2009).

Table 4. Classification and measured thermal and electrical characteristics of observed NRP discharge regimes (T_g = 1000 K, *PRF* = 30 kHz, d = 5 mm, v = 2 m/s). Taken from Pai, 2009.

Regime name	Appearance	Energy deposited per pulse	Gas Heating ($+\Delta T_g$)	Conduction current
Corona	Corona	< 1 □J	< 200 K	< 2 A
Glow	Diffuse	1-10 □J	< 200 K	< 2 A
Spark	Filamentary	>100 μJ	>1000	

1.4 Atmospheric plasmas applications

Many applications in different fields can benefit from the use of atmospheric plasmas (Table 5). For these discharges some challenges appear, such as how to identify the physico-chemical mechanisms involved and to optimize them in each specific application. We describe below a few examples of such applications following the classification presented in the reviews of Tendero *et al*. (2006) and Marode *et al*. (2009).

Table 5. Examples of plasma/surface interactions using non-thermal plasmas and the active component of the plasma that contributes to the desired product (Selwyn *et al*., 2001)

Material/ Substrate	**Desired Component**	**Desired Product**
Semiconductor substrate	Active neutral and ionic etching speciesgenerated by electron impact	Thin film deposition, stripping, cleaning
Magnetic storage media	Sputtered atoms generated by ion bombardment of the target	Magnetic thin films,anti-corrosive coatings
Glass	Thin film chemical precursors, neutrals	Energy efficient coatings
Textiles	Ion bombardment, active neutrals	Increased wettability, wear properties

Industrial cleaning	Oxygen atoms, ions	Oxidation and removal of organic films
Food processing/ agents/medical equipment	O, O_2^+, H, OH: chemical reactions initiated by plasma chemistry	Destruction or denature of pathogens, prions;chemical destruction of toxins
Water/ wastewater treatment	O, O_2, O_3, OH: chemical reactions initiated by plasma chemistry	Removal or destruction of water contaminant pathogens, and reduction of biological oxygen demand (BOD)

1.4.1. Ion based applications

These applications consist in producing ions by plasmas which charge suspended particles, used as aerosol nucleation, subsequent coagulation, and powder formation and coating. In this section, we will describe in more details plasma coating applications: two kinds of atmospheric plasma coatings are developed: air plasma sprays and plasma enhanced chemical vapour deposition. Air Plasma Spray coatings have been introduced in industry for many years and mainly developed in the aeronautic field (Fauchais, 1996).

Atmospheric non-thermal plasmas are used as a chemically reactive media to activate the coating reactions. The reactive species are carried to the surface substrate where they adsorb and react, with also desorption as an additional result. The coating grows by a germination-growth phenomenon. Two plasma-enhanced chemical vapour deposition configurations can exist: direct or remote. In the direct mode, the gas plasma and the precursor are injected in the discharge. This mode ensures the complete precursor decomposition. All materials can be deposited assuming that a precursor exists, including oxides, polymers, or carbon coatings. Because the plasma is a very reactive medium, deposition mechanisms are still not clearly explained. Several investigations have been conducted to achieve a better understanding of these phenomena (Babayan *et al*., 2001; Asmann *et al*., 2000). Another interesting application was presented by (Borra., 2005) where atmospheric non-thermal plasmas were used to produce nano-sized particles using plasma nucleation. This is illustrated in figure 1.14.

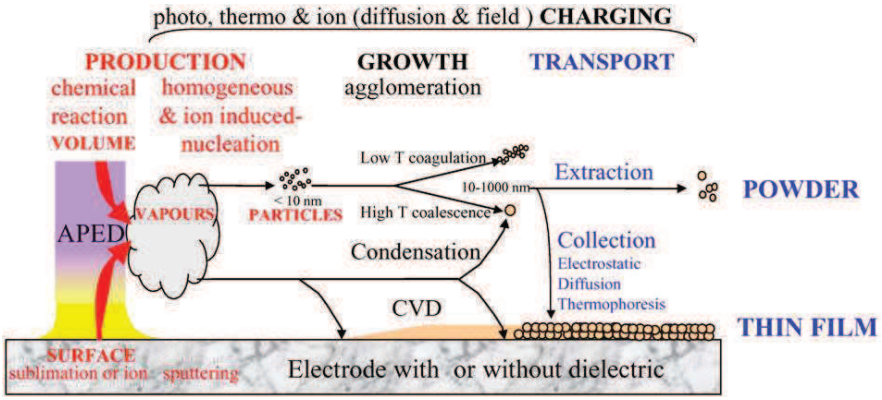

Figure 1.14. Mechanisms of vapour and particle production (nucleation), growth, charging and transport in Atmospheric Pressure Electrical Discharges (APED) (Borra, 2006)

1.4.2. Plasma chemistry, pollution control and ozone removal

For depollution applications, Atmospheric Non-Thermal Plasmas are required to produce active species that react with toxic species, thus reducing their toxicity. The pollutants are found in the chemical industry, in exhaust gases and so on. The main environmental issues are due to the following toxic compounds: nitrogen oxides (NOx), gas volatile organic compounds (VOCS), hydroflurocarbons (HFCs), chlorofluorocarbons (CFCs) and sulfur dioxide (SO_2).

Plasma treatment targets these toxic molecules, breaking them up by collisions with the active species produced by the discharge. This decomposition results in the creation of radicals that combine to form harmless molecules for environmental applications. This is well reviewed in (Mizuno, 2007).

Baeva *et al*. (2002) succeeded in reducing NOx from synthetic exhaust gases. The experiments were carried out at atmospheric pressure with a pulsed microwave source in gas mixtures containing $N_2/O_2/NO$. To avoid creation of an additional NO when N_2 and O_2 react, a pulsed source was used. The temperature increase and the N_2, O_2 reactions were then controlled.

Another environmental issue is the NO rejected in the atmosphere as a component of exhaust gases from fuel plants. It was shown by Leipold *et al*. (2006) that a reduction of NO was noticed in oxygen exhaust gas treated by a DBD nitrogen plasma, illustrated by figure 1.15. It was shown that the NO concentration could

be reduced by 79 % at a discharge power of 468 W and at a given flow rate ratio of N_2 and N_2+NO mixture.

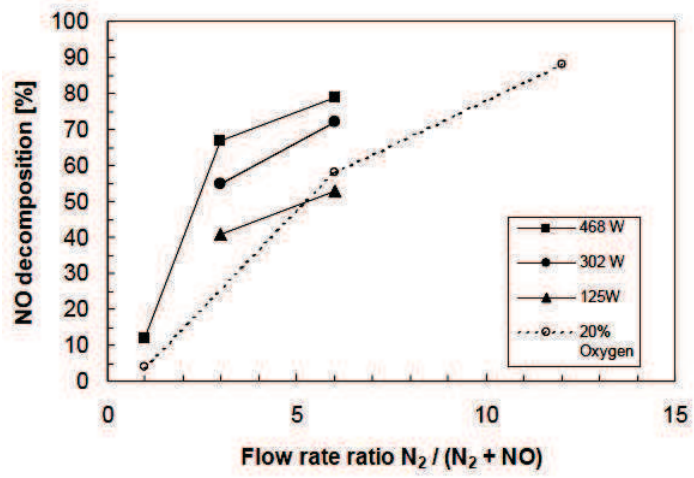

Figure 1.15. NO removal versus the ratio of the N_2 flow rate through the discharge to the synthetic exhaust gas mixture (N_2+NO) flow rate for various power settings (Leipold *et al.*, 2006)

One of the best known chemistry applications of Atmospheric Non-Thermal plasmas is the production of ozone for water treatment and for the food industry (Guzel-Seydim *et al.*, 2004). Ozone can be produced in oxygen, air, or N_2/O_2 plasmas. The plasma generators are generally used for large scale production of ozone. Corona discharge systems produce between 1% and 6% by weight, whereas using a non plasma process which is UV ozone generators, the concentrations of ozone obtained are between 0.1% and 0.001% by weight.

1.4.3. Plasma-assisted combustion

Over the past decade, intense research has taken place to investigate the possibility of sustaining lean flames, which have the advantage of producing reduced levels of nitric oxides, with plasma discharges. The field of Plasma-Assisted Combustion has emerged as a very active field in the worldwide scientific community.

In particular, high voltage nanosecond repetitively pulsed discharges were demonstrated to efficiently stabilize lean turbulent flames, as reported by Pilla *et al.* (2006) or Lou *et al.* (2007), and to significantly reduce the lean extinction limits in a premixed hydrocarbon-air flame. The stabilization region is illustrated in figure 1.16

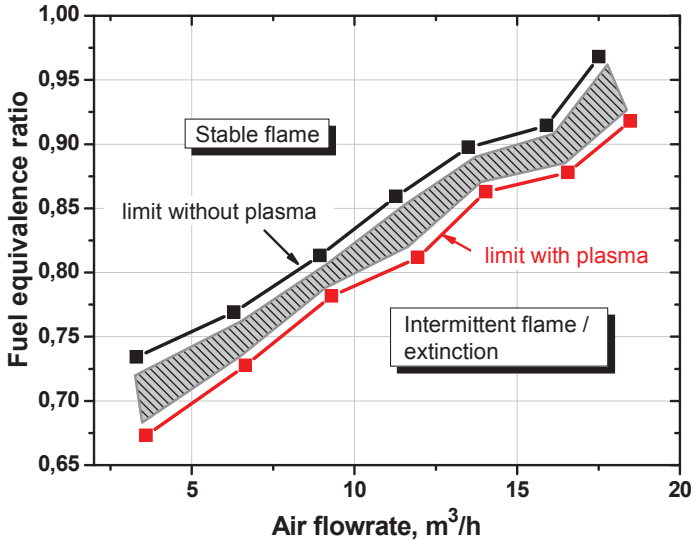

Figure 1.16. Flame regimes with filamentary NRP discharge at 30 kHz (Pilla, 2008))

NRP discharges have also proven to be very efficient in igniting propane air mixture either at stoichiometric or at lean conditions and in mixtures with nitrogen dilution. When applied to diluted mixture, the ignition delay was significantly reduced. Figure 1.17 presents these results (Pancheschnyi *et al*., 2006).

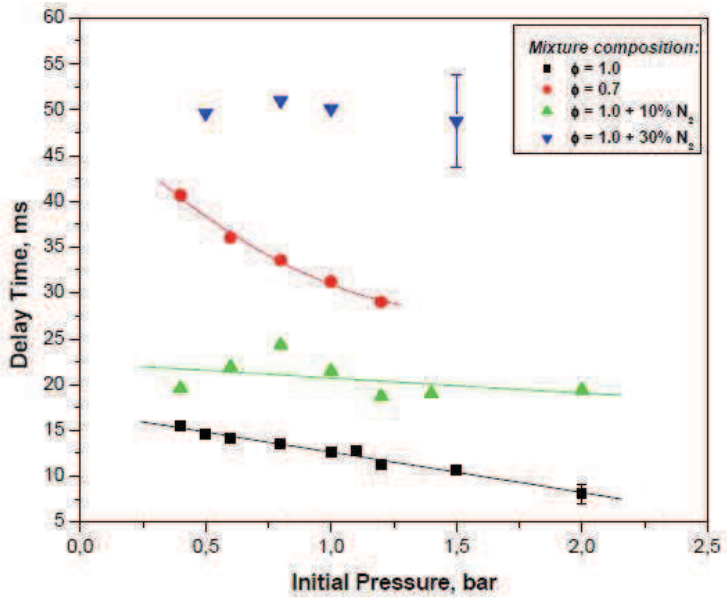

Figure 1.17. Combustion delay time for different dilution (Pancheschnyi *et al*., 2006)

The reduction of the ignition delay time was also observed in other studies (Starikovskii *et al*., 2003). The experiments were made in nanosecond duration discharge pulse, in argon diluted H_2/ air mixtures preheated to ~900 K in a shock tube, Results are shown in figure 1.18.

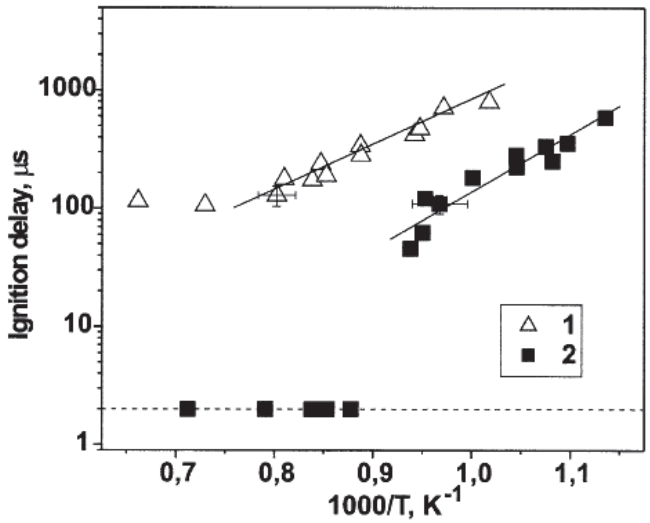

Figure 1.18. Measured ignition delay time in function of gas temperature. Mixture H_2: O_2: N_2: Ar (1) Autoignition, (2) with nanosecond discharge (Starikovskii *et al*., 2003)

Other studies about using plasma discharges to ignite (Matveev *et al*., 2009) show that these plasmas allow a strong interaction in the combustion region, which considerably improves ignition. Figure 1.19 presents one of the plasma igniters applied to an industrial gas turbine.

A fairly comprehensive review of the work on plasma assisted combustion up to 2006 may be found in the review by Starikovskaya (2006).

Figure 1.19. Plasma Igniter in operation (Matveev *et al.*, 2009)

As we have briefly discussed in this section, several investigators have demonstrated that atmospheric non-thermal plasmas in general present a great interest for many applications and that for more specified ones, particularly when atmospheric pressure is needed and non sparking regime is required, NRP discharges are central. We have also seen that filamentary NRP discharge present great potential for many applications, in particular PAC, where a key effect in flame stabilization appears to be the production of oxygen radicals. We will thus investigate in this thesis the mechanism of production of atomic oxygen by NRP discharges. One of the mechanisms proposed in the literature is the so-called two-step mechanism. A better understanding of this phenomenon could lead to a better control and optimization of many applications where atomic oxygen is needed.

1.5 Two step mechanism for oxygen production and gaz heating in air atmospheric pressure discharge

The transfer of energy of the gas electrons is done according to the different modes of gas excitation. The energy of the discharge could be used in various chemical channels. The fractions of power dissipated in each mode of excitation depend on the electric field and the energy of the electrons. Studies show that in air for a reduced electric field (E/N) in a range of10 to 100 Td, the nitrogen vibrational excitation is dominant. To be able reach the excitation, dissociation and ionisation of nitrogen and

oxygen, a reduced field above 100 Td is necessary. In this region the electronic excited states of nitrogen are dominant as shown in figure 1.20. This is the typical conditions of our discharge, where nitrogen excited states will play a key role in the production of important specie for many applications: atomic oxygen

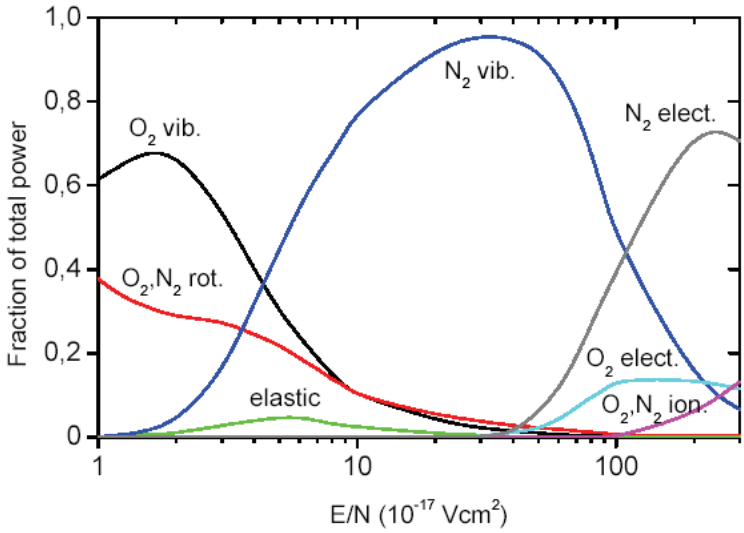

Figure 1.20 Fractions of power dissipated in different modes of excitation for air as a function of reduced electric field (Aleksandrov *et al*, 1981).

Under these conditions in air plasma at atmospheric pressure, Popov, suggested a kinetic model which describes the dynamics of the main components of the discharge. It is assumed that, the gas particles are excited from the ground electronic state mainly by electron impact (Popov, 2001). The rates of the corresponding processes were determined previously and appear in the literature (Aleksendrov *et al*, 1981; Kossyi *et al*, 1992).

According to the model the atomic oxygen, which is the specie of interest, could be produced through two main channels:

-A direct way where molecular oxygen produce by electron impact atomic oxygen or,

-An indirect way where nitrogen produce by electron impact excitation excited electronic states which then reacts with molecular oxygen to create atomic oxygen (see reactions 1 and 7 of the table).

Table 6. Kinetic model suggesting the atomic oxygen production by nitrogen excited states quenched with oxygen. *et al*

No.	Reaction	Rate constant
1	$N_2(A^3\Sigma_u^+) + O_2 \longrightarrow N_2(v) + 2O(^3P) + \varepsilon_1$	1.7×10^{-12} cm^3/s
2	$N_2(A^3\Sigma_u^+) + O_2 \longrightarrow N_2(v) + O_2(b^1\Sigma_g^+, v)$	7.5×10^{-13} cm^3/s
3	$N_2(A^3\Sigma_u^+) + N_2(A^3\Sigma_u^+) \longrightarrow N_2(v) + N_2(B^3\Pi_g)$	7.7×10^{-11} cm^3/s
4	$N_2(A^3\Sigma_u^+) + N_2(A^3\Sigma_u^+) \longrightarrow N_2(v) + N_2(C^3\Pi_u)$	1.6×10^{-10} cm^3/s
5	$N_2(A^3\Sigma_u^+) + N_2(v' > 4) \longrightarrow N_2(v) + N_2(B^3\Pi_g)$	$10^{-10}\exp(-1500/T)$ cm^3/s
6	$N_2(A^3\Sigma_u^+) + O(^3P) \longrightarrow N_2(v) + O(^1S)$	3.0×10^{-11} cm^3/s
7	$N_2(B^3\Pi_g) + O_2 \longrightarrow N_2(v) + 2O(^3P) + \varepsilon_7$	3.0×10^{-10} cm^3/s
8	$N_2(B^3\Pi_g, v = 0) + N_2 \longrightarrow N_2(A^3\Sigma_u^+) + N_2(v)$	1.0×10^{-11} cm^3/s
9	$N_2(a'^1\Sigma_u^-) + O_2 \longrightarrow N_2(v) + O(^3P) + O(^1D) + \varepsilon_9$	2.8×10^{-11} cm^3/s
10	$N_2(a'^1\Sigma_u^-) + N_2 \longrightarrow N_2(v) + N_2(v)$	2.0×10^{-13} cm^3/s

This model suggests also a fast heating of the gas discharge due to the exothermic effect of the nitrogen quenching reactions. Popov shows that this heat release can reach up to about 25% of the discharge power when the reduced electrical field is between 200-250 Td as presented in figure1.21.

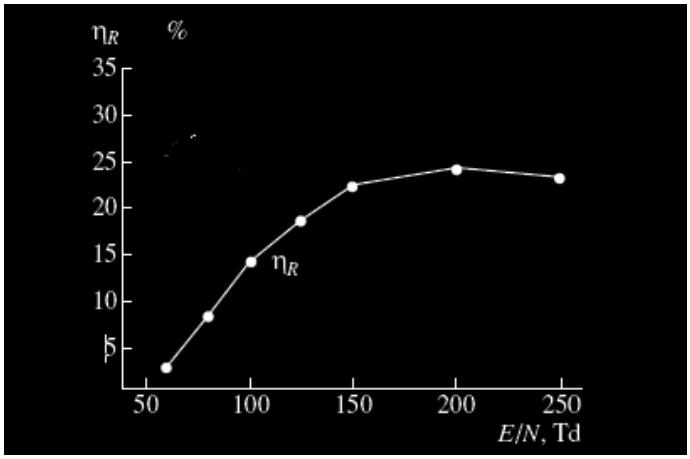

Figure 1.21 The parameter η_R as function of E/N in a discharge in an N2 : O2 = 4 : 1 mixture, where η_R is the fraction of the discharge power that are expended on gas heating

As a summary, our experimental conditions for NRP discharges are run in a reduced electric field of 200-250 Td, this allows to predict that the main heating mechanism for oxygen production is a two step mechanism:

$$\begin{cases} N_2 + e \rightarrow N_2(A,B,C) + e \\ N_2(A,B,C) + O_2 \rightarrow N_2 + 2O + \Delta Q \end{cases}$$

To validate this discharge kinetic, we focused during this work on measuring each parameter of the two step reactions:

-The density of the nitrogen excited states,

-the density of the atomic oxygen produced,

-the evolution of the gas discharge temperature and

-the fraction of energy which goes into the heat release

Chapter 2. Optical Diagnostics Principles

In this chapter, the principles of the spectroscopic methods used for the investigations of the nanosecond repetitively pulsed discharges, i.e. Optical Emission Spectroscopy, Cavity Ring-Down Spectroscopy and Two-Photon Absorption Laser Induced Fluorescence are presented.

2.1 Optical Emission Spectroscopy (OES)

2.1.1 Principle of optical emission spectroscopy

Optical emission spectroscopy is one of the most widely used non-invasive diagnostic techniques for plasma investigations. The emission spectrum represents the intensity emitted by the plasma as a function of the wavelength. Once calibrated in absolute radiance units ($Wcm^{-2}sr^{-1}nm^{-1}$), it can be used to infer the absolute densities of the emitting species, based on spectroscopic and radiative data from the literature (Demtroeder, 2003).

Temporally and spatially resolved measurements can be made of temperatures and of the densities of excited atomic and molecular species, using appropriate detection systems.

The internal energy of atoms is determined by the orbital movement of electrons around the nucleus, which is described by quantized electronic states. The transitions between different excited states are governed by selection rules. The excited states can be either radiative states, meaning their lifetimes are on the order of ns - μs, or metastable states, which have much longer radiative lifetimes, sometimes on the order of hours. Typical atomic spectra recorded by a spectrometer are characterized by narrow spectral lines. The intensity of each line is proportional to the density of the emitting state and to the transition probability (Demtroeder, 2003).

In addition to electronic excited states, molecules have vibrational and rotational levels due to the quantification of the vibrational and rotational motion. The population distribution of molecules over the available internal energy states (rotational,

vibrational, and electronic) is generally determined by the balance of collisional and radiative processes. In the case of thermal equilibrium, the population distributions follow the so-called Boltzmann distribution.

A photon recorded by a spectrometer is in general the result of the spontaneous transition of an atom or a molecule from an upper to a lower internal energy level, as shown in figure 2.1. The emitted photon is characterized by a frequency ν:

$$\nu = \frac{\Delta E}{h} = \frac{1}{h}\left(E_{e'v'J'} - E_{e''v''J''}\right) \qquad \text{eq. 1}$$

where h is the Planck constant, ΔE is the energy difference between the two levels, and $E_{e'v'J'}$ and $E_{e''v''J''}$ represent the energies of the upper and lower level, respectively. The symbols e, *v,* and J stand for the electronic, vibrational and rotational quantum numbers, and the ' and '' designate the upper and lower states, respectively.

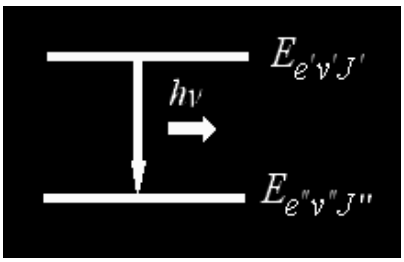

Figure 2.1. Spontaneous emission

The energy of a molecule in a level of quantum numbers (e, *v,* J) is given by the sum:

$$T_{evJ} = T_e + G(v) + F(J) \qquad \text{eq. 2}$$

where T_e is the electronic energy, G(v) is the vibrational energy and F(J) is the rotational energy.

As an example, Figure 2.2 shows a potential energy diagram with the electronic and vibronal levels of the nitrogen molecule (Gilmore, 1965). The excited electronic states investigated by OES in this thesis are $N_2(B^3\Pi_g)$ and $N_2(C^3\Pi_u)$, which will be simply noted $N_2(B)$ and $N_2(C)$ in the rest of this thesis.

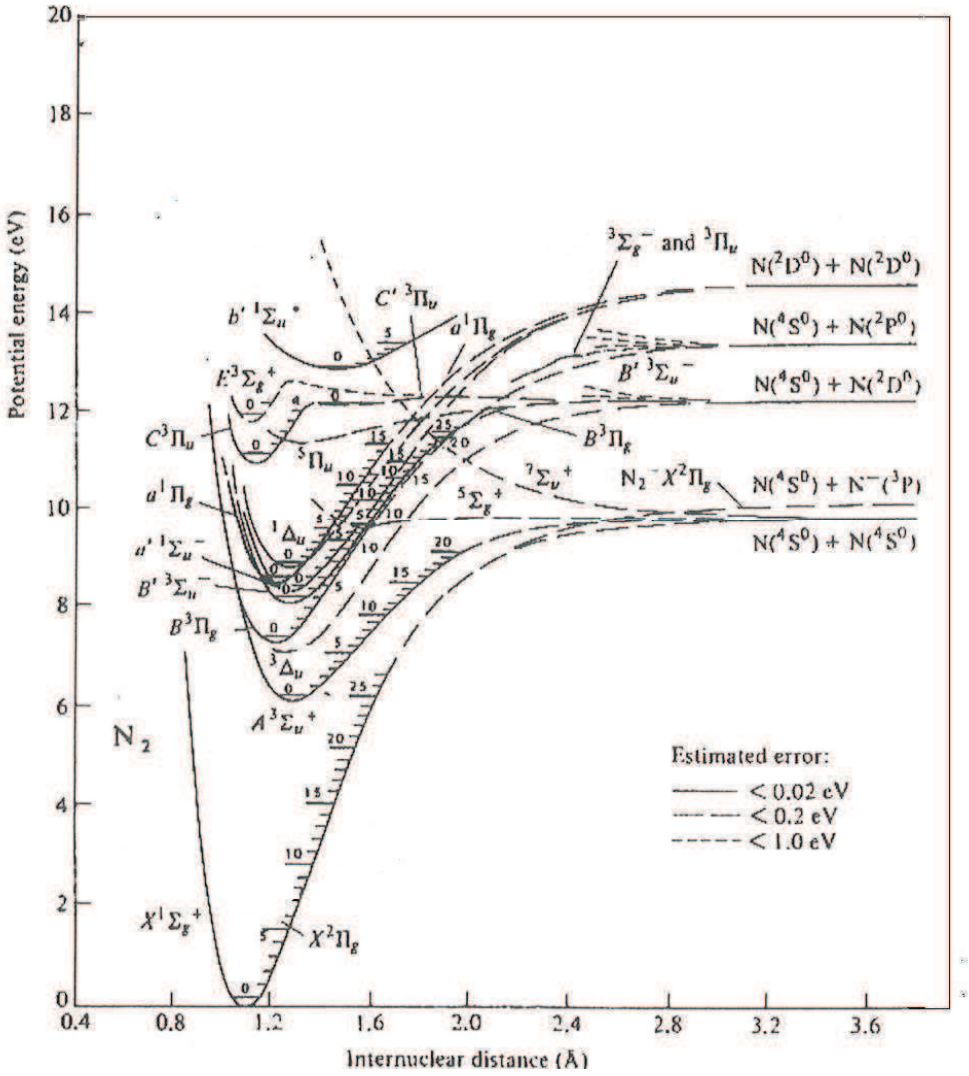

Figure 2.2 The potential energy curves of the nitrogen molecule and the electronic and vibrational levels (Gilmore, 1965).

2.1.2 Density measurements by optical emission spectroscopy (OES)

Optical emission spectroscopy (OES), as we mentioned, provides a non-invasive method to investigate atoms, ions, and molecules in plasmas. It can provide information about such properties as excited state species densities, energy level distributions (hence the translational, electronic, vibrational, rotational temperatures) electron-atom, atom-atom and ion-atom collisional effects, charge transfer between plasma constituents, and electric and magnetic fields to name a few. Its use, as a diagnostic tool for

emitting media, has led to a greater understanding of very complex phenomena such as plasma discharges, the evolution of stellar atmospheres, or of the processes occurring in fusion plasmas.

The local spectral emissivity of a volumetric light source (e.g. plasma) is given by:

$$\varepsilon_\lambda = \frac{1}{4\pi} h\nu A_{21} N_2 \phi(\lambda) \qquad \text{eq. 3}$$

where the emissivity is calculated per unit of solid angle ($1/4\pi$), $h\nu$ (J) is the energy of the emitted photon, A_{21} (s^{-1}) is the Einstein coefficient, N_2 (cm^{-3}) is the population density of the upper state from where spontaneous emission occurs, and $\phi(\lambda)$ (nm^{-1}) is the normalized profile function $\left(\int \phi(\lambda) d\lambda = 1\right)$. We note the lower state 1 and the upper state 2.

The spectral intensity measured using a spectrometer corresponds to the line-of-sight integration of the local spectral emissivity. If the emission volume is uniform, optically thin, and of length L, then the measured line intensity as a function of wavelength is given by:

$$I_\lambda = \int_0^L \varepsilon_\lambda(l)\, dl = \frac{1}{4\pi} L\ h\nu\ A_{21}\ N_2\ \varphi(\lambda) \qquad \text{eq. 4}$$

Natural, Doppler, Stark, pressure and instrumental broadenings are the mechanisms that determine the shape of emission lines in plasmas at atmospheric pressure (see for example Griem 1974 or Laux 2003). We briefly describe them below.

A. Pressure broadening

For an isolated particle (atoms, molecules), the typical natural lifetime is about 10^{-8} s, and the line width is about 5×10^{-4} cm^{-1}. As the pressure increases, the distance between particles decreases and collisions occur. As the molecules get closer, their potential fields overlap and this can change the natural line width. Furthermore, collisions between particles can shorten the lifetime, and hence the line width becomes larger;

The resulting line shape is a Lorentz function (except at very high pressures where the molecular potentials overlap strongly). The line width depends on the collision frequency, i.e. on the number density of molecules (pressure) and on their relative speed (square root of the temperature).

B. Doppler broadening

Doppler broadening is another major source of line broadening. The molecules are in motion when they emit or absorb. This causes a change in the frequency of the incoming radiation as seen in the molecule reference frame. In atmospheric pressure air, molecules move with velocities determined by the Maxwell Boltzmann distribution. In this case, the Doppler broadening produces a Gaussian lineshape with a full width at half maximum that varies as the square root of the gas temperature.

C. Instrumental broadening

The instruments used to measure the emission spectra obtained from the plasma introduce another type of broadening to the spectra lines. This broadening depends on several parameters such: the configuration of the spectrometer, the size of the entrance slit, the detector pixel width, the spectrometer focal length, the grating groove density, the dispersion order, etc. The shape of this function can usually be approximated by a trapezoidal function (which sometimes reduces to a triangular or near Gaussian function) and in most emission experiments (with low resolution spectrometers) is the largest contribution to the broadening. In this case, the function $\phi(\lambda)$ can be measured by recording the spectral line profile of a narrow laser source, such as a typical laboratory HeNe laser.

D. Voigt profile

The overall line shape resulting from the described broadenings can be often described by the Voigt function, which is a convolution of the Lorentz and Gaussian profiles. The Voigt profile shows a Doppler-like behaviour in the line core, and a Lorentz-like behaviour in the line wings. Examples of different emission line profiles are shown in Figure 2.3.

We can now return to the question of how to determine the density of an excited state from emission spectroscopy measurements. The density of an excited state, N_2, can be obtained from equation 2 as:

$$N_2 = \frac{4\pi I \lambda}{L h\nu A_{21} \phi(\lambda)} \qquad \text{eq. 5}$$

Thus we can obtain the average density of the excited state over the slab of length L by measuring the peak intensity of the spectral line, with knowledge of the Einstein coefficient from the literature, and with the line profile function determined as described in the previous paragraphs.

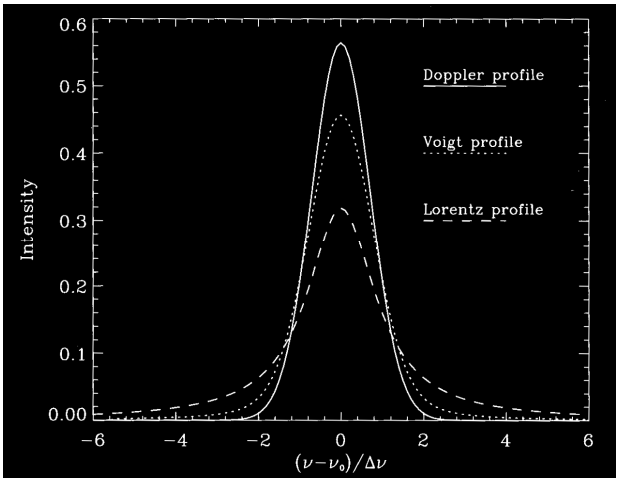

Figure 2.3 Examples of different emission spectral profiles: Doppler, Lorentz and Voigt.

2.1.3 Determination of rotational, vibrational and electronic temperatures using Specair

Several plasma parameters can be obtained from a recorded emission spectrum. In addition to absolute densities we can also get the translational, rotational, vibrational and electronic temperatures of the discharge species. Specair is a program developed to simulate the emission and absorption spectra of plasmas. Using advanced quantum mechanics and spectroscopic data, the program can calculate spectra based on a wide range of input parameters such temperatures, pressure, species densities etc (Laux, 2003).

Specair simulates emission intensities for atoms (N,O,C) and diatomic molecules (N_2, O_2, NO, OH, CN, N_2^+,…ect) which can be in thermal equilibrium (all temperatures are equal) or nonequilibrium. Thermal equilibrium implies a Boltzmann distribution of the population over the internal energy of molecules and atoms at a common temperature $T=T_{rot}=T_{vib}=T_{el}$. Thus, at equilibrium for molecules we will have a Boltzmann distribution of the populations over the electronic, vibrational and rotational levels. Specair can also model non-thermal plasmas with Boltzmann distribution at different temperatures T_{rot}, T_{vib} and T_{el}.

For instance, if we consider the population of the vibrational levels in the electonically excited state $N_2(C)$ of the molecular nitrogen, the density of a specific

vibrational level v' under a Boltzmann distribution is related to the vibrational temperature by the formula:

$$n_{v'} = \frac{\exp\left(-E_{v'}/kT_{vib}\right)}{Q_{vib}} n_{N_2(C)} \qquad \text{eq. 6}$$

with

$$Q_{vib} = \sum_{v'} \exp\left(-E_{v'}/kT_{vib}\right) \qquad \text{eq. 7}$$

where $E_{v'}$ is the energy of the vibrational level, Q_{vib} is the vibrational partition function, and $n_{N2(C)}$ is the density of the N_2 state.

In the same way we can introduce the rotational temperatures which is related to the population distribution over the rotational levels for a given vibrational state, and the electronic temperature which is related to the population distribution over the electronic levels (Laux, 1993).

In practice, if one measures the population of several vibrational levels, $n_{v'}$. The vibrational temperature can be obtained using eq. 4. In the present work the different distributions (rotational, vibrational, electronic) were simulated using Specair by changing T_{rot}, T_{vib}, T_{el} until fitting the measured spectra.

Due to fast rotational-translational energy relaxation at atmospheric pressure, we consider in this work that the rotational and the translational temperatures are in equilibrium. Thus, we used the rotational temperature as an estimate of the gas temperature.

2.1.4 Space resolved OES

In our pin–to-pin electrode configuration, the plasma has cylindrical symmetry. The species have a radial distribution with maximum at the discharge center and with sub-millimetre FWHM. Lateral intensity measurements give the function $I_\lambda(x)$ shown in figure 2.4. An Abel inversion is then applied to obtain the local distribution of the emissivity using equation 8:

$$\varepsilon_\lambda(r) = -\frac{1}{\pi}\int_r^R \frac{I_\lambda'(x)}{\sqrt{x^2 - r^2}} dx \qquad \text{eq. 8}$$

where $I_\lambda'(x) = -\frac{dI_\lambda}{dx}$.

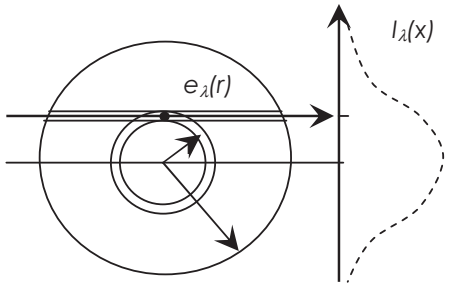

Figure 2.4 Schematic of lateral measurements of the intensity $I_\lambda(x)$. The local emission $\varepsilon_\lambda(r)$ is obtained after Abel inversion.

However the emissivity in absolute units is rather difficult to obtain. Many experimental parameters including the solid angle, collection volume, response of the spectrometer and collection optics, and the quantum efficiency of the detector have to be known. In practice a calibrated light source (e.g. tungsten strip lamp) is used in place of the plasma while keeping all experimental parameters identical. The measured spectra in arbitrary units (usually volts or counts) are then converted in emissivity units (W $cm^{-3}sr^{-1}$ nm^{-1}). For details on the Abel-inversion and absolute calibration procedure, the reader is referred to Laux (1993).

2.2 Cavity Ring-Down Spectroscopy (CRDS)

The CRDS method is an absorption-based technique, which allows the detection of species at very low concentrations. The very high sensitivity is achieved by using multi-pass optical cavities, which increase the effective absorption length. This technique was used in the thesis to determine the density of nitrogen metastable, $N_2(A)$, in the nanosecond repetitively pulsed discharges. The principles of the method are detailed next.

2.2.1 Principle of absorption spectroscopy

Absorption spectroscopy is a simple method for determining the concentration of gas-phase (or liquid phase) species (atoms, molecules, and ions) by measuring the fraction of light absorbed by the species. If the absorption coefficient at the measurement wavelength is known, the absolute concentration can be determined from the fraction of light absorbed.

When using a laser of weak intensity, absorption spectroscopy is a non-invasive

in situ plasma diagnostic. The advantages of absorption spectroscopy are its simplicity of application and the direct interpretation of results. The requirement on the species of interest is that it absorbs some of the incident light. This technique is indeed easier to apply in comparison with laser-induced fluorescence or to emission techniques where an absolute intensity calibration is needed. The difficulty with traditional absorption spectroscopy is that its sensitivity depends on the ability to distinguish a small change in the incident light after it passes through the sample. This small change in the transmitted light can often be overwhelmed by experimental noise or light source fluctuations. Thanks to specific properties such as high intensity, and monochromaticity, laser based absorption techniques have helped improve the detectivity of absorption techniques.

The fraction of light absorbed by a gas sample of uniform temperature, pressure, and density is proportional to the sample path length and the absorption coefficient of the specific species transition. Thus, attenuation of the incident light in a homogeneous media is given by the well-known Beer-Lambert law:

$$I(\nu) = I_0(\nu)\exp\left(-k(\nu)l_{abs}\right) \qquad \text{eq. 9}$$

where $I(\nu)$ is the intensity of the light transmitted through an homogenous absorbing medium of length l_{abs} (units cm) and $I_0(\nu)$ is the incident light intensity. The absorption coefficient, $k(\nu)$, (units cm^{-1}) is given by:

$$k(\nu) = \frac{1}{l_{abs}}\ln\left(\frac{I_0}{I}\right)_\nu, \qquad \text{eq. 10}$$

from which we define the absorbance as:

$$\ln\left(\frac{I_0}{I}\right)_\nu = k(\nu)l_{abs}$$

The absorption coefficient integrated over an absorption line is related to the species density by:

$$\int k(\nu)d\nu = S(T)N \qquad \text{eq. 11}$$

where S(T) (units cm) is the so-called line strength, and N (units cm^{-3}) is the total species density. Thus, if the absorption coefficient is measured and the line strength is known, absolute species densities are obtained.

2.2.2 Classical CRDS

While the absorption technique is robust and widely applied, the primary difficulties encountered with the use of conventional absorption spectrometers for the determination of gaseous species in challenging situations are the insufficient sensitivity and the lack of spectroscopic data. The overlapping of absorption bands of different species limits the selectivity of the method. It is clear from eq.10 that if the measured absorption is very weak, I will be approximately equal to I_0. Thus the problem encountered in determining a very weak absorption line by traditional methods is the difficulty in measuring a small difference between two large numbers, both of which are uncertain as a result of experimental light source fluctuations. If the light source for the absorption measurements is a pulsed laser, the pulse-to-pulse variations in the intensity of the laser can easily mask a very weak absorption, making the use of traditional methods unsatisfactory for this purpose.

Cavity Ring-Down Spectroscopy (CRDS) is an advanced absorption-based technique. It was discovered during attempts to measure the reflectivity of high reflectance mirrors. The principles of CRDS have been presented in many references (Paldus and Zare, O'Keefe and Bush, 1999). We will summarize the principles below.

The technique makes use of an optical cavity composed of two or more mirrors. The mirrors used to form the cavity are an important factor in cavity ring-down spectroscopy. In general, multilayer dielectric mirrors have a higher reflectance (typical reflectivity of 99.99 %) than the best metallic mirrors. In figure 2.5 a typical reflectivity of a dielectric mirror used for CRDS is presented.

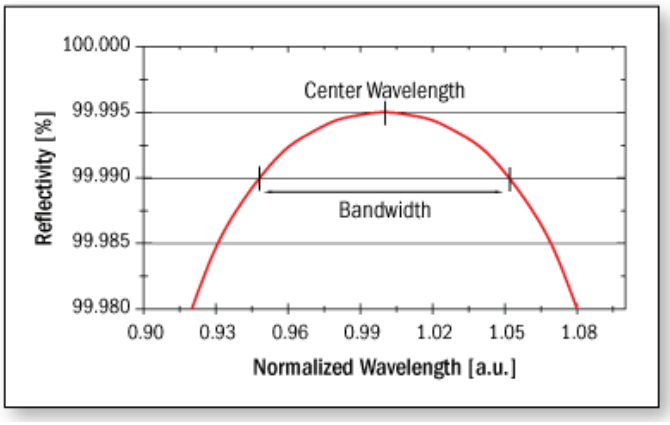

Figure 2.5 Typical reflectivity curve for a high reflectivity dielectric cavity mirror. The bandwidth of the mirror is defined as the region over which (1-R) is within a factor of two of the center wavelength peak reflectivity.

Figure 2.6 presents a typical two mirror cavity setup. The two mirrors M_1 and M_2 have the same radius of curvature R_m, and are spaced by a distance d. The Gaussian laser beam coupled into the optically stable cavity is characterized by the beam waist at the center w_0, and at the cavity mirrors, w_1.

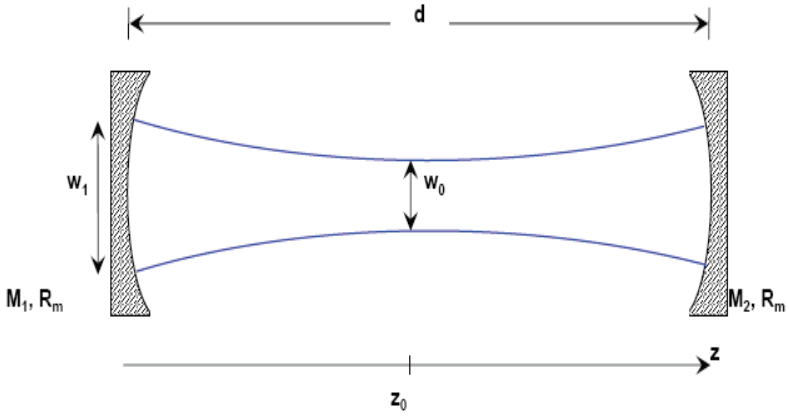

Figure 2.6. Schematic of a two-mirror cavity and the Gaussian laser beam

In figure 2.7, the cavity output intensity is represented during the ring-down cycles of the laser pulse travelling inside the cavity. Each time the laser pulse reaches one of the output cavity mirror a small part of the intensity (I_1, I_2, ...) leaks out, thus using a fast oscilloscope a train of pulses decaying in time will be measured. The envelope of pulse train exhibits an exponential decay as shown in figure 2.7. If we place an absorbing media inside the cavity, the exponential decay will be faster. The decay time difference with and without absorber is proportional to the density of the absorbing species, as will be discussed next.

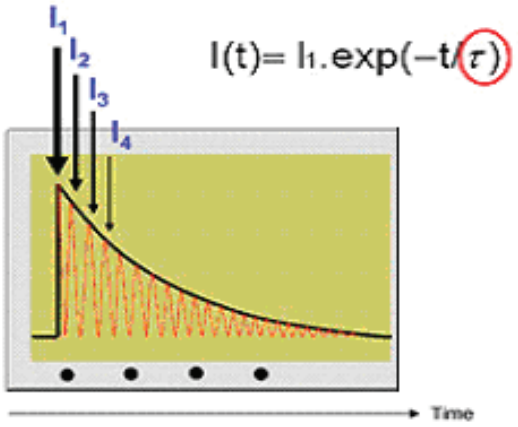

Figure 2.7 Signal intensity ring-down

The loss-per-path of the light intensity, *I*, inside the cavity has mainly two contributions, the loss due to absorption of gas species and the leak-out intensity at one mirror of the cavity. If the absorption per path is very small (fraction of absorbance <<1) then the loss intensity per path is given by,

$$\Delta I = -\left[k(\nu)\, l_{abs} + (1-R) \right] I \qquad \text{eq. 12}$$

where k(ν) is the absorption coefficient, l_{abs} is the length of the absorption volume and R is the reflectivity of the mirrors considered identically. For cavities with very high reflectivity mirrors (typically R > 0.999), the transmission loss is very little. The loss of a single path is therefore negligible small in comparison with the loss during the ring-down process. Thus the loss per path can be in good approximation considered differentially. The loss per unit of length is,

$$\frac{dI}{dl} = -\frac{\left[k(\nu) l_{abs} + (1-R)\right] I}{L} \qquad \text{eq. 13}$$

where L is the length of the cavity.

If no absorption is present inside cavity (k(ν) = 0), by substituting $dl = c\,dt$ (c is the speed of light) in (13) and integrating, one obtains the classical ring down decay intensity for empty cavity, I_1,

$$I_1(t) = I_0 \exp\left[-\frac{c}{L}(1-R)\, t \right] \qquad \text{eq. 14}$$

When an absorbing medium of constant concentration of volume length l_{abs} is introduced inside the cavity, the intensity follows the function, I_2,

$$I_2(t) = I_0 \exp\left\{ -\frac{c}{L}\left[(1-R) + k(\nu) l_{abs} \right] t \right\} \qquad \text{eq. 15}$$

The intensities I_1 and I_2 are well-known results, the typical CRDS single exponential intensity decays. The corresponding decay times (e time loss of intensity) for an empty cavity is:

$$\tau_0 = \frac{L}{c(1-R)} \qquad \text{eq. 16}$$

and for a cavity with absorption:

$$\tau = \frac{L}{c\left[(1-R) + k(\nu) l_{abs} \right]} \qquad \text{eq. 17}$$

Combining Eqs. (16) and (17) the absorption coefficient is obtained as:

$$k(\nu)=\frac{L}{c\,l_{abs}}\left(\frac{1}{\tau}-\frac{1}{\tau_0}\right) \qquad \text{eq. 18}$$

Thus by measuring the decay times with and without absorption one obtains the absorption coefficient and further the species concentration by using equation 11.

2.2.3 Time resolved CRDS

The above description is valid when the probed species densities are constant during the decay time. If the concentration of absorbing species changes during the ring-down time, the absorption coefficient becomes a function of time, k(ν,t) (Stancu et al., 2009) . Integrating Eq. (15), the decay of intensity, I_3, will be:

$$I_3(t)=I_0\exp\left\{-\frac{c}{L}\left[(1-R)\,t+\int_0^t k(\nu,t)\,l_{abs}\,dt\right]\right\} \qquad \text{eq. 19}$$

Combining Eqs. (14) and (19), the time-dependent absorption coefficient is obtained as:

$$k(\nu,t)=\frac{L}{c\,l_{abs}}\frac{d}{dt}\left(\ln\frac{I_1}{I_3}\right) \qquad \text{eq. 20}$$

From Eqs. (11) and (20), the species concentration time evolution will be given by,

$$N(t)=\frac{1}{S(T)f(\nu)}\frac{L}{c\,l_{abs}}\frac{d}{dt}\left(\ln\frac{I_1}{I_3}\right) \qquad \text{eq. 21}$$

where f(ν) is the normalized function of the absorption line profile, i.e. $\int f(\nu)d\nu=1$.

To obtain the time evolution of species concentration, it is necessary to measure the decay intensities I_1 and I_3, with and without absorption, respectively. One should build the time derivative of the logarithm of the intensities ratio, which is directly proportional to the absorption species density.

2.2.4 Space resolved CRDS

Similar to OES, absorption techniques also provide line-of-sight integrated signals. From Eq. (14), the measured absorption coefficient is an average value over the absorption length. Assuming cylindrical symmetry for the plasma (which is the case for the NRP discharge studied in this thesis), an Abel inversion can be used to recover the local absorption coefficients. From lateral absorbance measurements (absorbance, i.e.

$\tau(v) = \ln(I_0/I)_v$, we obtain the function $\tau_v(x)$ shown in figure 2.8 . The local absorption coefficient as a function of the radius, *r*, can be obtained from:

$$k_v(r) = -\frac{1}{\pi}\int_r^R \frac{\tau_v'(x)}{\sqrt{x^2 - r^2}}\,dx \qquad \text{eq. 22}$$

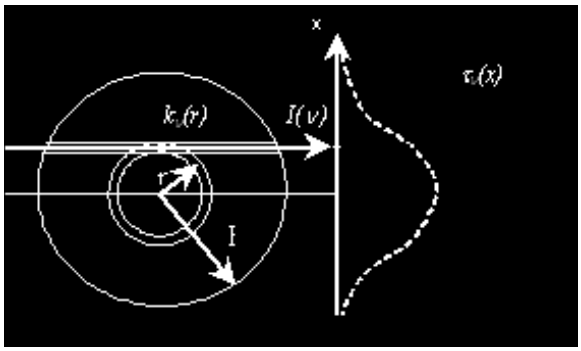

Figure 2.8. Schematic of lateral absorbance measurements $\tau_v(x)$. The local absorption coefficient, $k_v(r)$, is obtained after Abel inversion.

2.2.5 Two-mirror optical cavity and mode formations

In order to perform a CRDS experiment, the design of a stable optical cavity and adequate coupling of the laser beam is essential. Here a few details about the optical cavity and mode formation in cavities are given.

Optical cavities are built by two or more highly reflective optical elements such as mirrors and prisms. Here we limit our discussion to two-mirror cavities, which was the system used in the present work, and which is the most commonly used cavity setup for pulsed CRDS. In figure 2.9, the stability diagram for a two-mirror optical resonator is represented. The optical resonator parameters g is defined as:

$$g_1 = 1 - \frac{L}{R_1}, \quad g_2 = 1 - \frac{L}{R_1} \qquad \text{eq. 23}$$

where L is the length of the cavity, R_1 and R_2 are the radii of curvature of the two mirrors.

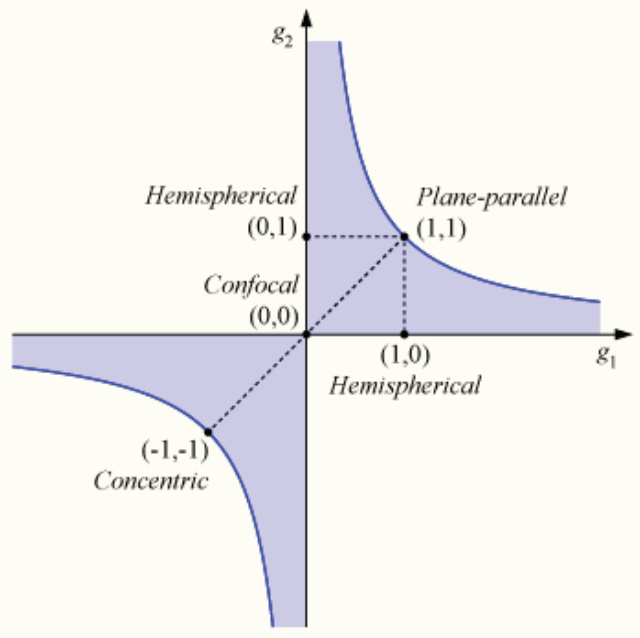

Figure 2.9. Stability diagram of a two-mirror optical resonator

The stability range is defined by the condition $0 \leq g_1 g_2 \leq 1$, which corresponds to the shaded domain in figure 2.9. Along the diagonal axis $g_1 = g_2 = g$, we find the most used optical resonators formed by two identical mirrors. Details about different types of resonators such as planar (g = 1), confocal (g = 0), concentric (g = -1), on how to minimize beam steering caused by temperature gradients, and on the cavity design will be given in chapter 3.

The role of mode formation in cavity ring-down spectroscopy has been discussed extensively in the literature (K.W Busch). When a pulsed laser with very short pulse duration is used, the coherent wave-train emitted during the pulse can be less than the length of the optical cavity. If this is true, mode formation is considered to be unimportant since the returning wave can never overlap the initial wave because the wave-train is too short.

Modes in cavities are classified into two basic types. Longitudinal (or axial) modes determine the resonant oscillation frequencies that satisfy the wavelength requirements of the cavity along a given optical path, meaning that the electric vector of the light is zero at the reflective surfaces of the mirrors. Transverse modes determine the cross-sectional geometry of the beam. When tuning a single-frequency laser, transmission by a cavity shows a periodic pattern of peaks. The intensities of the peaks

depend on alignment and focusing, i.e. on mode matching.

When looking at the profile of the cavity output beam, the different transverse modes are found to be excited at different frequencies.

For a stable optical resonator formed by two identical mirrors, the beam size of the lowest-order transverse mode of the cavity (the Gaussian mode) is defined as (Bush et al, 1999):

$$w_0^2 = \frac{L\lambda}{\pi}\left[\frac{1+g}{4(1-g)}\right]^{0.5} \qquad \text{eq. 24}$$

$$w_1^2 = w_2^2 = \frac{L\lambda}{\pi}\left[\frac{1}{1-g^2}\right]^{0.5} \qquad \text{eq. 25}$$

where w_0 is the beam waist at the center of the cavity, w_1=w_2 are the beam waists at the cavity mirrors, and λ is the laser wavelength.

2.2.6 Mode matching calculations

In order to couple the laser beam into the optical cavity by help of optics such as lenses and mirrors, we performed mode-matching calculations using the so-called ray transfer matrix analysis. In the following, the principle of mode matching and of the ray trace calculation are described.

Mode matching of the lowest-order transverse mode (Gaussian mode) of the cavity is obtained when the waist of the incoming beam equals w_1 and is focused in such a way that in the middle of the cavity the beam waist equals w_0. The quantities w_0 and w_1 are the beam sizes at the center and at the mirrors of the stable symmetrical optical cavity, as given by Eqs.24 and 25.

Ray transfer matrix (RTM) analysis (also known as ABCD matrix analysis) is a type of ray tracing technique used in the design of optical systems, particularly lasers. It involves the construction of a ray transfer matrix, which describes the optical system. Tracing of a light path through the system can then be performed by multiplying this matrix with a vector representing the light ray. The technique uses the paraxial approximation of ray optics, i.e., all rays are assumed to be at a small angle (θ) and a small distance (x) relative to the optical axis of the system. The approximation is valid as long as $\sin(\theta) \approx \theta$ (where θ is measured in radians).

The ray tracing technique is based on two reference planes, called the input and output planes, each perpendicular to the optical axis of the system. Without loss

of generality, the optical axis is defined so that it coincides with the z-axis of a fixed coordinate system. A light ray enters the system when the ray crosses the input plane at a distance x_1 from the optical axis while traveling in a direction that makes an angle θ_1 with the optical axis. Some distance further along, the ray crosses the output plane, this time at a distance x_2 from the optical axis and making an angle θ_2. n_1 and n_2 are the indices of refraction of the medium in the input and output plane, respectively, as illustrated below:

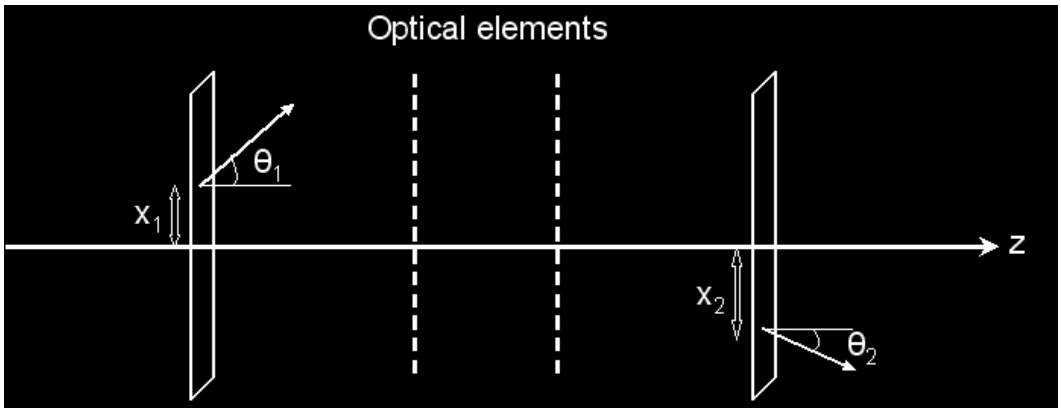

Figure 2.100 Ray tracing technique

These quantities are related by the expression

$$\begin{pmatrix} x_2 \\ \theta_2 \end{pmatrix} = \begin{pmatrix} A & B \\ C & D \end{pmatrix} \begin{pmatrix} x_1 \\ \theta_1 \end{pmatrix},$$

where

$$A = \left.\frac{x_2}{x_1}\right|_{\theta_1=0} \qquad B = \left.\frac{x_2}{\theta_1}\right|_{x_1=0},$$

and

$$C = \left.\frac{\theta_2}{x_1}\right|_{\theta_1=0} \qquad D = \left.\frac{\theta_2}{\theta_1}\right|_{x_1=0}.$$

This relates the ray vectors at the input and output planes by the ray transfer matrix (RTM) M, which represents the optical system between the two reference planes. A thermodynamics argument based on the blackbody radiation can be used to show that the determinant of a RTM is the ratio of the indices of refraction:

$$\det(\mathbf{M}) = AD - BC = \frac{n_1}{n_2}.$$

As a result, if the input and output planes are located within the same medium, or within two different media which happen to have identical indices of refraction, then

the determinant of M is simply equal to 1.

As shown in the following table, each simple optical component has a ray transfer matrix.

Table 2.1. Ray transfer matrices of typical optical components

element	Matrix	Remarks
Propagation in free space or in a medium of constant refractive index	$\begin{pmatrix} 1 & d \\ 0 & 1 \end{pmatrix}$	d = distance
Refraction at a flat interface	$\begin{pmatrix} 1 & 0 \\ 0 & \frac{n_1}{n_2} \end{pmatrix}$	n_1 = initial refractive index n_2 = final refractive index.
Refraction at a curved interface	$\begin{pmatrix} 1 & 0 \\ \frac{n_2-n_1}{R \cdot n_2} & \frac{n_1}{n_2} \end{pmatrix}$	R = radius of curvature, R > 0 for convex (centre of curvature after interface); n_1 = initial refractive index; n_2 = final refractive index.
Reflection from a flat mirror	$\begin{pmatrix} 1 & 0 \\ 0 & 1 \end{pmatrix}$	Identity matrix
Reflection from a curved mirror	$\begin{pmatrix} 1 & 0 \\ -\frac{2}{R} & 1 \end{pmatrix}$	R = radius of curvature, R > 0 for concave
Thin lens	$\begin{pmatrix} 1 & 0 \\ -\frac{1}{f} & 1 \end{pmatrix}$	f = focal length of lens where f > 0 for convex/positive (converging) lens. Valid if and only if the focal length is much greater than the thickness of the lens.

Using the matrix ray trace, the distances and the focal lengths of the lenses needed to do mode matching and spatial filtering can be calculated. Figure 2.11 shows schematics of the laser beam coupled into a semitransparent two-mirror cavity (M_1, M_2). The laser beam first passes a spatial filter (to obtain a Gaussian laser beam), which is

formed by the convergent lens L1, and a pinhole P. Then, using the convergent lenses L_2, L_3 and the mirror M_1 (which acts as a divergent lens for incoming laser beam), matching of the cavity resonator is realized. In practice, there is an infinity of possibilities to realize mode matching using one or a couple of lenses placed at precise positions.

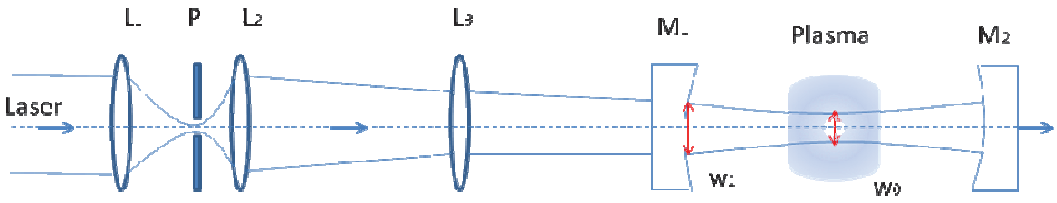

Figure 2.111. Schematic of the optics needed for spatial filtering and mode matching the resonant cavity. L_1, L_2, L_3: thin lenses with different focal lengths, P: pinhole and M_1, M_2: cavity mirrors

We will list in chapter 3 the geometrical and optical parameters chosen for the mode matching system and to optimize cavity stability.

2.3 Two-photon absorption laser induced fluorescence (TALIF)

In the previous sections, the principles of emission and absorption were described. Here; we will describe both the principles and the method for TALIF. This technique was used in the thesis to determine the atomic oxygen (O) density temporal evolution in the nanosecond plasma discharges. In the following, details of the method will be presented.

2.3.1 Principle of TALIF

The spectroscopy of multi-photon transitions has become possible using laser as light sources. TALIF, as the name suggests, is the absorption of two photons followed by emission (fluorescence) of a third photon (Niemi,2005). Two-photon absorption, as a second order effect, is inherently much weaker than single-photon absorption. However, forbidden transition probabilities or VUV laser requirements make TALIF an alternative to single-photon absorption techniques for investigations of ground state species.

A schematic of the electronic states for a TALIF experiment is shown in Figure

2.12. The evolution of the population densities in levels 1 and 2 can be described by a system of rate equations (Bamford, 1986; Udi, 2008).

$$\frac{d N_1(t)}{dt} = -R_\nu(t) N_1(t) \qquad \text{eq. 24}$$

$$\frac{d N_2(t)}{dt} = R_\nu(t) N_1(t) - [A + Q + \Gamma(t)] N_2(t) \qquad \text{eq. 25}$$

where $R_\nu(t)$ is the two-photon excitation rate which is given by:

$$R_\nu(t) = G^{(2)} \sigma^{(2)} g(\Delta\nu) \left(\frac{I_0(t)}{h\nu} \right)^2 \qquad \text{eq. 26}$$

with $G^{(2)}$, the photon statistic factor, $\sigma^{(2)}$, the excitation cross section, $g(\Delta\nu)$, the normalized line profile, $I_0(t)$, the laser intensity and $h\nu$, the photon energy. $\Gamma(t)$ is the ionization rate, given by:

$$\Gamma(t) = \sigma^i \left(\frac{I_0(t)}{h\nu} \right) \qquad \text{eq. 27}$$

where σ^i the ionization cross section.

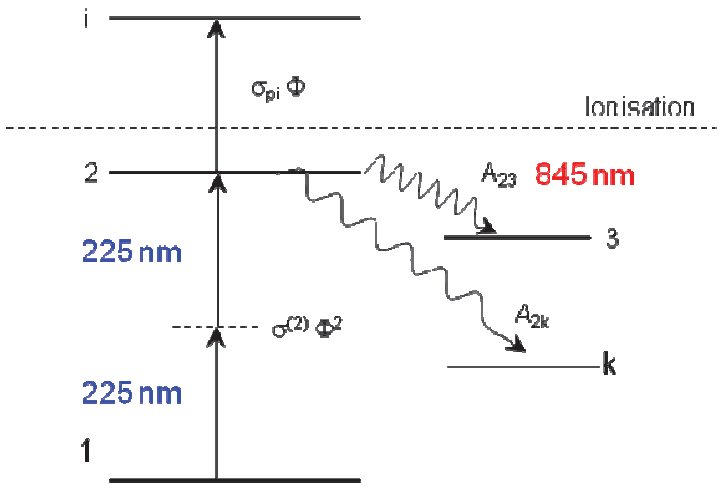

Figure 2.122. Energy level schematic for atomic oxygen in TALIF experiment with the two-photon excitation at 225 nm and the fluorescence at 845 nm.

A is the total fluorescence rate in all possible fluorescence channels, which is given by:

$$A = \sum_k A_{2k} \qquad \text{eq. 28}$$

and Q is the quenching rate:

$$Q = \sum_p k_p n_p \qquad \text{eq. 29}$$

where n_p is the collision partner number density and k_p is the corresponding quenching coefficient (Niemi, 2005).

We note the ground state level 1, the state pumped by two-photon absorption level 2, and level 3 is one of the states where the particles arrive after fluorescence, the transition 2→3 being used for measurement.

The two-photon excitation rate represents the number of electrons per second that are excited from level 1 to level 2, and depends on the effective two-photon absorption cross-section and the square of the photon flux.

The photoionization rate depends on the photon flux and on the excited state photoionization cross section. The fluorescence rate, A, represents the Einstein coefficient for the spontaneous emission in all fluorescence channels, which for atomic oxygen is $A \cong A_{23}$ because the other channels are transition dipole forbidden.

Because the measurements of atomic oxygen were carried out at atmospheric pressure, the most important process causing the depletion of level 2 is the quenching by collisions with N_2 and O_2.

In the non-saturation regime, i.e. when the depletion of the ground state is negligible, the total number density of the ground state atoms (level 1) is given by:

$$N_1 = \frac{\iiint_{t,\lambda L,\lambda F} S_{TALIF}\, dt\; d\lambda_L\, d\lambda_F}{D\,\frac{A_{23}}{A+Q+\Gamma}\, h\nu_F\, G^{(2)}\hat{\sigma}^{(2)}\,\frac{\int_t I_0(t)^2\, dt}{(h\nu_L)^2}} \qquad \text{eq. 30}$$

where S_{TALIF} is the fluorescence signal integrated over time, t, λ_F is the fluorescence wavelength (lines centered at 844.6 nm for O), and λ_L is the laser wavelength (225.6 nm for O). D characterizes the LIF detection system, accounting for the collection volume, the solid angle, the transmitivities of the fiber, filter and spectrometer, and for the quantum efficiency of the detector. $A_{23}/A+Q+\Gamma$ is the fluorescence quantum yield (branching ratio) and represents the ratio of radiative depletion of level 2 (i.e. by emission into the channel used for our measurements), to all other depletion losses of the level 2.

If the parameter D is kept constant during the parametric plasma studies, the fluorescence signal normalized to the square of the laser intensity is directly proportional to the ground state concentration (level 1). Absolute densities can be

obtained if all parameters in equation (30) are measured.

The ground state of atomic oxygen is a triplet $^3P_{2,1,0}$ with corresponding energies of 0, 158.3 and 227 cm^{-1}, respectively. Consequently, the fluorescence signal is proportional to the population of the sublevel from where the two-photon absorption takes place. Since the separation energies are smaller than the kinetic energy of plasma heavy particles, the population distribution of the triplet is governed by collisions. Hence, the distribution of population over the triplet should follow a Boltzmann equilibrium distribution at the gas temperature. The total oxygen number density, N_{total}, is given therefore by:

$$N_{total} = N_1 \sum_j g_j e^{-E_j/kT} \Big/ g_1 e^{-E_1/kT} \qquad \text{eq. 31}$$

where N_1 is the measured density of one of the sublevels with statistical weight g_1 and energy E_1, and g_j and E_j are the statistical weights and energies of all O electronic levels. Here, the two-photon transition for densities measurements was chosen from the $^3P_2$ sublevel. For the typical plasma conditions, i.e. gas temperature of 1000 K, about 61 % of the O population is expected to be in the $^3P_2$ state (Stancu et al., 2009).

2.3.2 Space resolved TALIF

Because of cylindrical symmetry of our discharge the local density of the species measured in emission ($N_2(B)$, $N_2(C)$) and absorption ($N_2(A)$) can be obtained using the Abel inversion procedure. While the emission and absorption are line-of-sight integration techniques, the laser induced fluorescence techniques (including TALIF) give access to local densities, the spatial resolution of the technique being determined by the intersection of the laser beam and the volume limited by the collection optics.

In Fig. 2.13, a schematic of the probed volume in a TALIF experiment is shown. For our experiments the plasma diameter is larger than the diameters of the collection cylinder and of the laser. The spatial resolution of the TALIF experiment is limited to the intersection of the laser cylinder and the cylinder formed by the collection optics. If the laser beam waist is equal to the waist of the cylinder defined by the collection optics, then the sample volume is the Steinmetz volume. The measured density is an average of the particle density present in this volume.

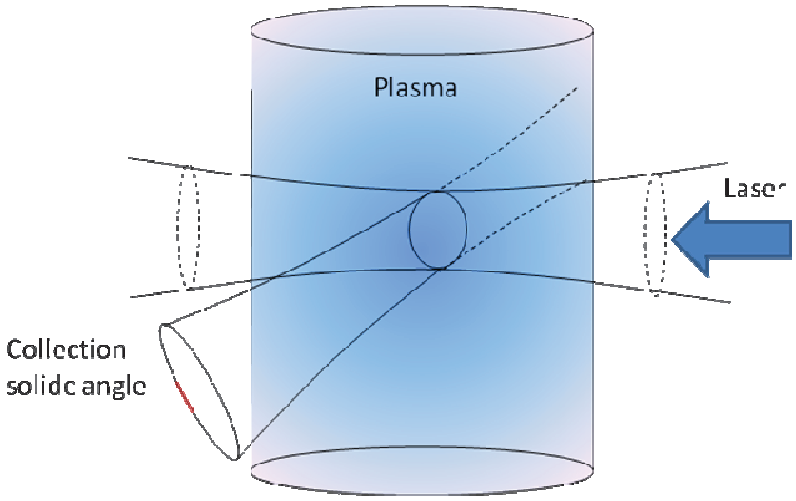

Figure 2.133 Schematic of the collection volume in a TALIF experiment.

Chapter 3. Experimental set-up

This chapter describes the different set-ups implemented and/or developed during this work to perform the experimental studies.

The understanding and validation of the ultrafast mechanism require the measurements of the densities of various important species together with the quantification of the energy deposited into the gas by the discharge.

The absolute densities of excited nitrogen, $N_2(B)$ and $N_2(C)$, were measured by fast Optical Emission Spectroscopy (OES). $N_2(A)$ metastable was another key species to investigate in our NRPD. For this we developed a Cavity Ring-Down Spectroscopy (CRDS) set-up to measure its density. In order to access the density of atomic oxygen, we used a Two-photon Absorption Laser Induced Fluorescence (TALIF) set-up. Electrical measurements were implemented to measure the current and the voltage of the discharge in order to determine the energy deposited per pulse in plasma.

This chapter comprises four sections. In the first section, we present the discharge set up and explain the electrical measurement procedure together with the synchronization strategy. The second section describes the OES set-up used for measurements of excited species. The ICCD camera response optimization and the calibration procedure are explained. The next section provides details about the CRDS technique and the cavity design parameters which were used to measure the nitrogen metastable $N_2(A)$. The last section presents the: TALIF experimental set-up used to measure the density of ground state atomic oxygen.

3.1 Nanosecond repetitively pulsed discharge set-up

Description of the NRPD set- up

The NRP discharges studied in this thesis are generated by applying high voltage pulses between two pin electrodes separated by 4 mm, in preheated atmospheric pressure air or nitrogen at 1000 K. Figure 3.1 shows the nanosecond repetitively pulsed discharge set-up and the electrical diagnostic instrumentation.

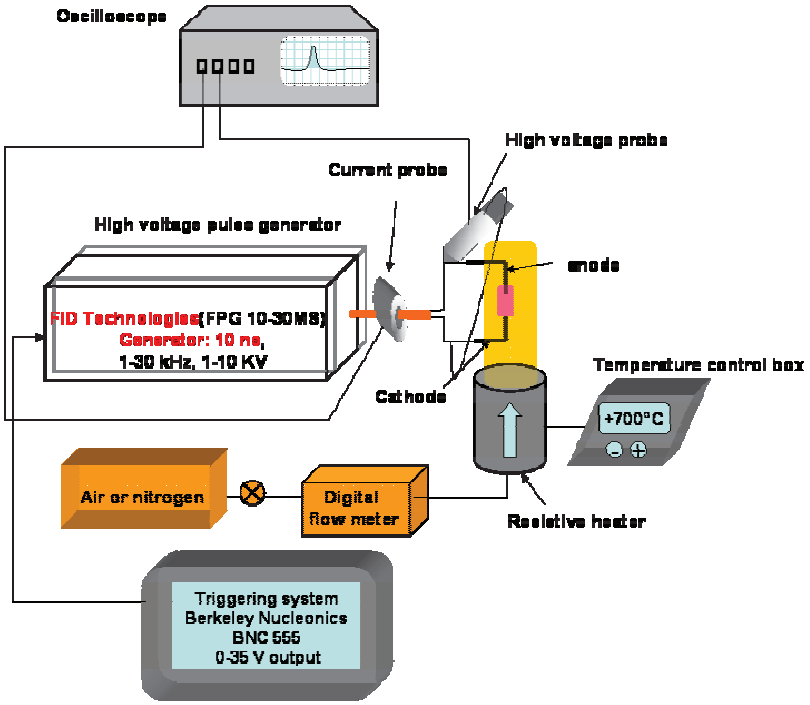

Figure 3.1 Schematic of the nanosecond repetitively pulsed discharge set-up with instrumentation for electrical diagnostics.

The pulses are produced by a FID Technologies generator (FPG 10-30MS) that produces high voltage pulses with rise times of 2-3 ns, fall times of 5 ns, a flat top of 10 ns at greater than 90% of the maximum voltage, and amplitudes up to +5 kV into a matching 75Ω impedance or up to 10 kV into an open circuit or a short circuit. The pulse repetition frequency (PRF) ranges from 1-30 kHz. The system was triggered with a Berkeley Nucleonics (BNC) 555 four-channel pulse

delay generator. The standard connecting cables are 2-m BNC coaxial cables which are always used to relay the BNC's trigger signals to other devices.

The preheated air flow is obtained with an Osram Sylvania Hot Air System heater. The latter is basically a steel tube (2.5-cm inner diameter) fitted with a ceramic wrapped resistive heating coil that allows to adjust the flow temperature between 300 K and 1000 K. The temperature in the system is controlled through an internal thermocouple, located 2.5 cm upstream of the heater outlet, and a regulation control loop. We verified that this system can maintain a stable temperature for several hours of continuous run. The preheated gas was injected below the lower electrode with flow rates between 0.5 to 2 ms^{-1}.

A Sierra Instruments Smart Trak digital mass flow meter calibrated for air and nitrogen is used to regulate compressed laboratory-grade air or nitrogen from 5 atm down to 1 atm. Its flow rate can be adjusted up to 166 slpm. The gas used was either dry air or nitrogen (standard "Azote U" with nitrogen fraction > 99,99% , water ≤ 5 ppm and oxygen ≤ 5 ppm).

The electrodes are refractory steel domestic heater electrodes bent into a 90° angle to create a vertical pin to pin electrode configuration aligned with the axis of the flow. The bottom electrode is the grounded cathode. The anode is placed above, with an interelectrode gap of about 4 mm. As the experiments are carried out at high temperature for long durations, we to periodically resharpened the electrode to maintain the electrode's radius of curvature constant at around 200 μm, so as to maintain a constant electric field between the electrodes.

Electrical measurements of current and voltage are performed using various high frequency probes. The voltage is measured with a 100-MHz bandwidth high-voltage probe (Lecroy PPE20kV), and the current with a Pearson coil current monitor (Model 6585) with a 3 dB low frequency cutoff at 400 Hz, a ±3 dB high frequency cutoff at 250 MHz, a 1.5 ns rise time, and a 1A/1V current-to-voltage conversion when terminated into 1-MΩ. The voltage and current measurements are recorded by a 350-MHz bandwidth (maximum 1 or 2 GS/s) LeCroy oscilloscope triggered by the BNC. One of the important issues of the experimental work was to synchronize the time evolution of the electrical measurements with emission, absorption and fluorescence measurements.

Synchronization

In order to understand the fundamental processes of the NRP discharges, we measured the time evolution of the densities of $N_2(B)$ and $N_2(C)$ in the plasma together with the current and the voltage of the discharge.

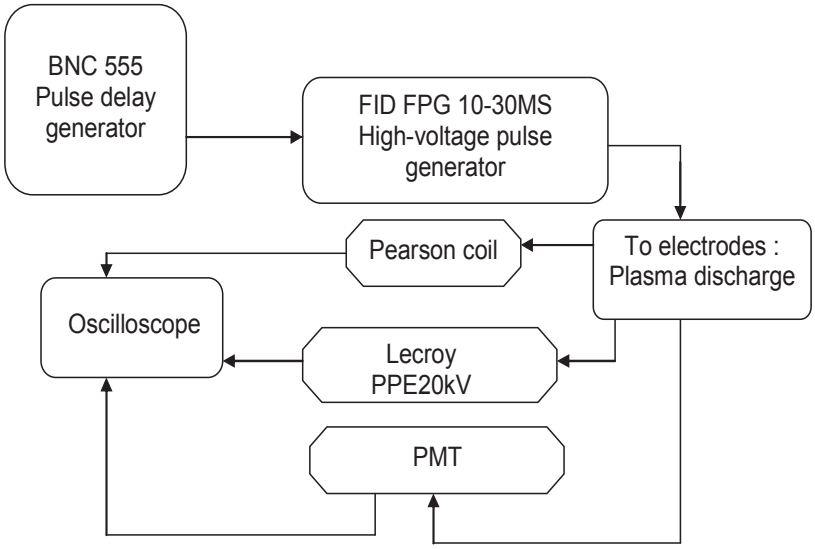

Figure 3.2 Schematic of signal synchronization between the discharge emission recorded by the PMT and the electrical measurements obtained by the current and voltage probes.

Figure 3.2 shows the experimental setup used for electrical measurements. To synchronize these measurements with the discharge emission, we used a Photomultiplier Tube (PMT, Hamamatsu H9305-03) equipped with a high-speed amplifier (Hamamatsu C5594-44). The characteristics of the PMT and the amplifier are given in Table 3.1:

Table 3.1. PMT and amplifier characteristics

Hamamatsu H9305-03 Photomultiplier Tube Module (PMT)	Characteristics
Cathode radiant sensitivity at 337 nm	80 mA/W
Rise time	1.4 ns
Typical electron transit time	15 ns
Maximum output signal current	10 μA
Control voltage adjustment range ($V_{control}$)	+0.25 to +1.0 V
Maximum dark current	10 nA
Maximum gain	10^7
Hamamatsu C5594-44 High-speed amplifier	
Minimum upper cutoff (-3 dB) frequency	1.2 GHz
Maximum lower cutoff (-3 dB) frequency	100 kHz
Input current-to-voltage conversion factor	3.15 mV/μA
Minimum voltage gain at 100 MHz	34 dB (factor 63)
Gain flatness from 200 kHz to 1 GHz	±1 dB

As shown in figure 3.3, synchronization between the BNC trigger signal and the probes was performed in several steps.

The transit time inside the PMT is the only time that needs further investigation to be determined.

Experimental set up

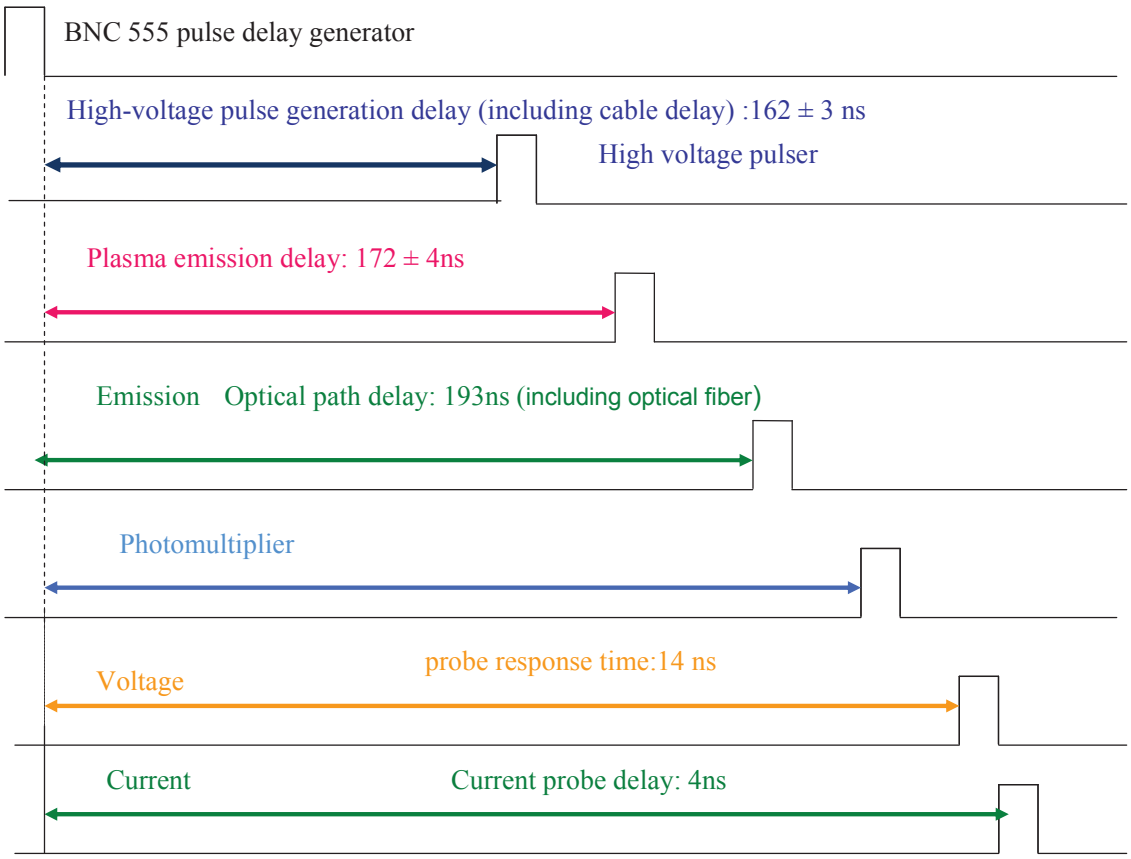

Figure 3.3 Diagram of the synchronization timing of the electrical measurements with the PMT

The delay of the high-voltage pulse (due to electronics and connecting cables) following the moment of the trigger signal (delivery by the BNC generator) was measured ranged from 159 to 165 ns. The plasma emission initiates 8-16 ns after the beginning of the high-voltage pulse. The optical path consists of the optical free path between the mirrors (0.4 m), the fiber optic bundle (3 m), and the monochromator (2 m). This counts for a total optical path delay of 18 ns. To obtain the delays of the voltage and the current probes, it is sufficient to compare in time each instrument signal on the oscilloscope with the one obtained connecting directly the oscilloscope to the pulse generator. To determine the delay time of the PMT, we use a 7 ns wide pulse produced by our Nd:Yag laser. The signal measured with the PMT is compared with the signal recorded an ultrafast photodiode UPD (Alphalas, UPD-200-UD) with a response time of 200 ps. Typical signals are shown in figure 3.4. Different signals, from low to high PMT gain, were measured by increasing the control voltage of the PMT.

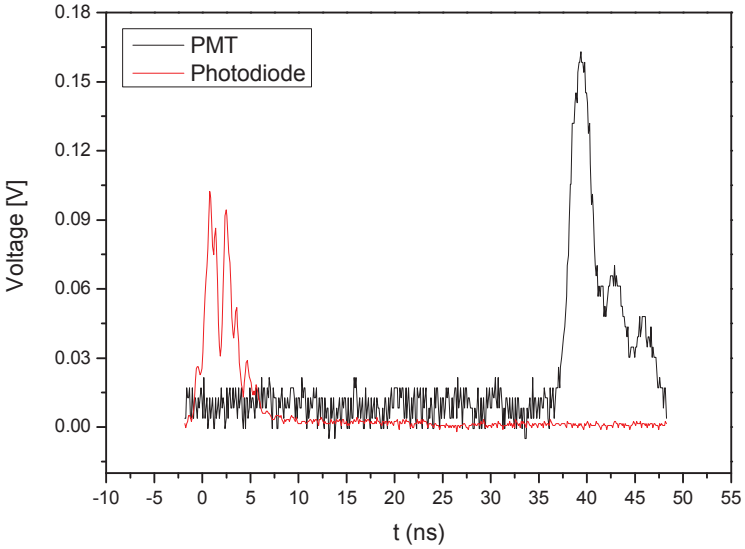

Figure 3.4. Sample ND- YAG laser signal of 7 ns width recorded by the ultrafast photodiode and by the PMT

For low PMT gains (0.25-0.4 V), the laser width recorded by the PMT is found to be 10,4 ns (wide signal) and does not vary from shot to shot. This could be explained by a decrease of the sensitivity of the PMT for weak gains. On the other hand, for higher gains (0.7–1 V), the recorded pulse width varies from shot to shot, but is sometimes narrower, thus closer to the laser manufacturer specifications. In addition, for certain shots, the rise and fall times are also in agreement with the specifications (rise time of ~2 ns and fall time of ~6 ns). It should be noted that during these experiments, we also acquired several signals of the voltage and the current. Very little variation between acquisitions was observed for the electrical measurements. This confirms that the variations in PMT signal are not caused by electrical signal fluctuations..

To understand this apparently erratic behavior of the PMT, we carried out measurements at relatively high PMT gain V= 0,67V. Hundreds of acquisitions were taken in a single shot oscilloscope mode. These single shot measurements confirm that there are two types of signal: the first type exhibits ringing, which is attributed to a hysteresis phenomenon at high signal intensities, resulting in distorted PMT signals. The second type of data is hysteresis-free and consistent with the manufacturer specifications. Figure 3.5 shows samples of each case.

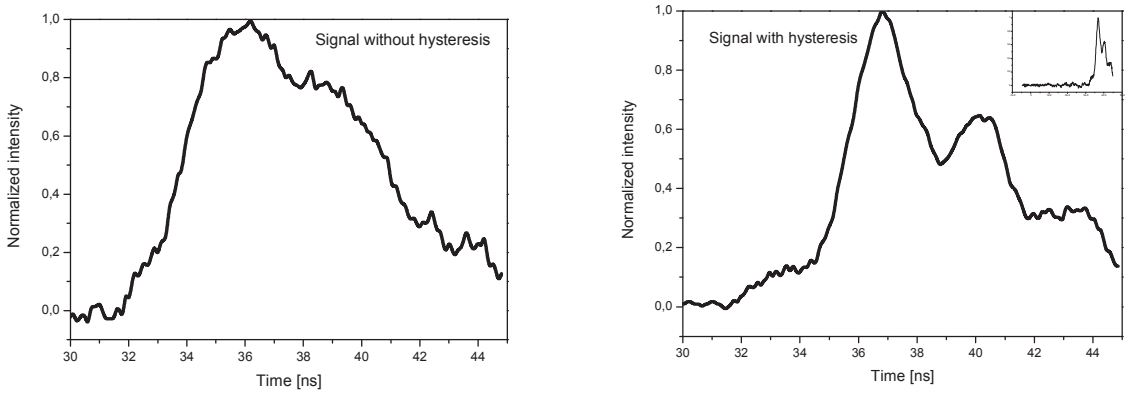

Figure 3.5 Sample recorded PMT signals with and without hysteresis

We now compare the emission measurements obtained with the PMT and with the spectrometer. We only consider the PMT signals without hysteresis. Figure 3.6 shows a comparison of the emission signal measured with the spectrometer with the spectrally integrated emission measured by the PMT. The two signals are synchronized at the beginning of the rise time of the two curves. As can be seen in Figure 3.6, the rise time of the PMT signal agrees well with the spectrometer measurements. The PMT decay time is also consistent with the spectrometer measurements, and in both cases the laser profile has a temporal width of about 7 ns, consistent with the laser manufacturer's specifications.

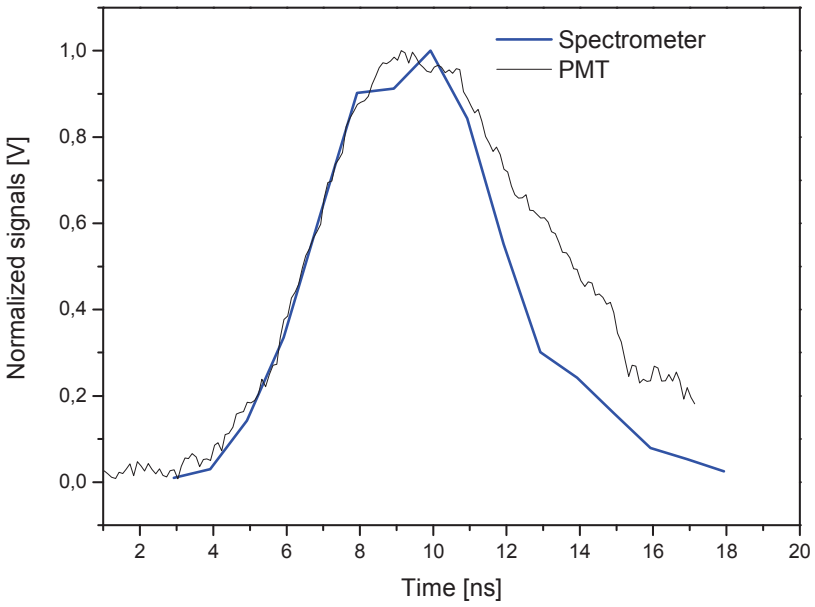

Figure 3.6. Plasma emission signal recorded with the PMT at 0,67 V gain synchronized on the rise time of the emission of $N_2(C)$ obtained using the spectrometer

We can then complete the determination of the PMT delay. To this end, the PMT signals without hysteresis are measured and compared with the signals recorded with the ultrafast photodiode (which, again, can be considered to have zero delay). The PMT delays so determined are shown in figure 3.7. As can be seen in this figure, the PMT delay is a strong function of the applied gain. This will be taken into account in synchronizing the emission signals with the electrical measurements.

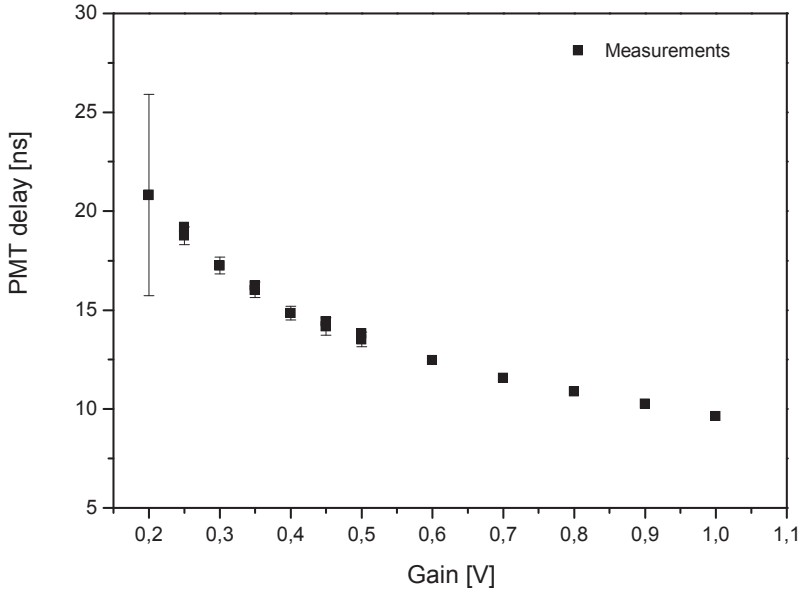

Figure 3. 7 PMT delay as a function of the PMT gain (Hamamatsu H 9305-03). The measured delay include a 10.6 ns delay time due to the 3m long optical fiber.

The resulting synchronized traces of voltage, conduction current, and emission of $N_2(C)$ are shown in figure 3.8. Voltage pulse generation delays following the moment of trigger signal delivery by the BNC generator were measured as a function of the input DC voltage with a error of <300 ps and ranged from 162 to 165 ns. This includes the interconnecting cable delay, which was not measured separately.

The plasma emission begins 8-16 ns after the initiation of the high-voltage pulse. This light reaches the camera after following the path through the mirror optics (0.4 m), the fiber optic bundle (3 m), and the monochromator (2 m), for a total optical path delay of 18 ns.

We see that the discharge current peaks a few nanoseconds after the applied voltage, and that the emission of $N_2(B)$ and $N_2(C)$ follows the discharge current

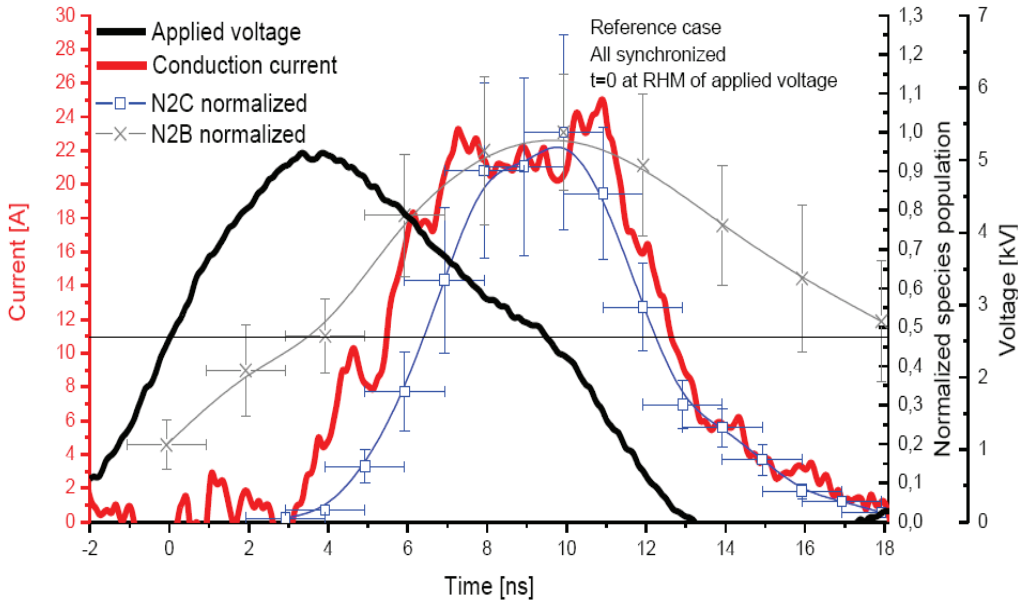

Figure 3.8 Synchronized electrical measurements (voltage and current) and spectroscopic emission measurements of $N_2(C)$ and $N_2(B)$. Time 0 ns corresponds to the instant where the voltage pulse has reached half of its maximum value. The present measurements are performed in the standard conditions defined in section 4.1.1

3.2 Optical Emission Spectroscopy (OES)

Optical emission spectroscopy allows us to access the densities of the nitrogen excited states, $N_2(B)$ and $N_2(C)$, which emit in the UV, visible and Near-IR. This will permit the evaluation of the temporal evolution of the densities and temperatures of these species, and thus their impact on the ultrafast mechanism suggested.

A photograph of the collection optics system used for emission measurements is shown in figure 3.9. A schematic of this setup is given in figure 3.10.

Experimental set up

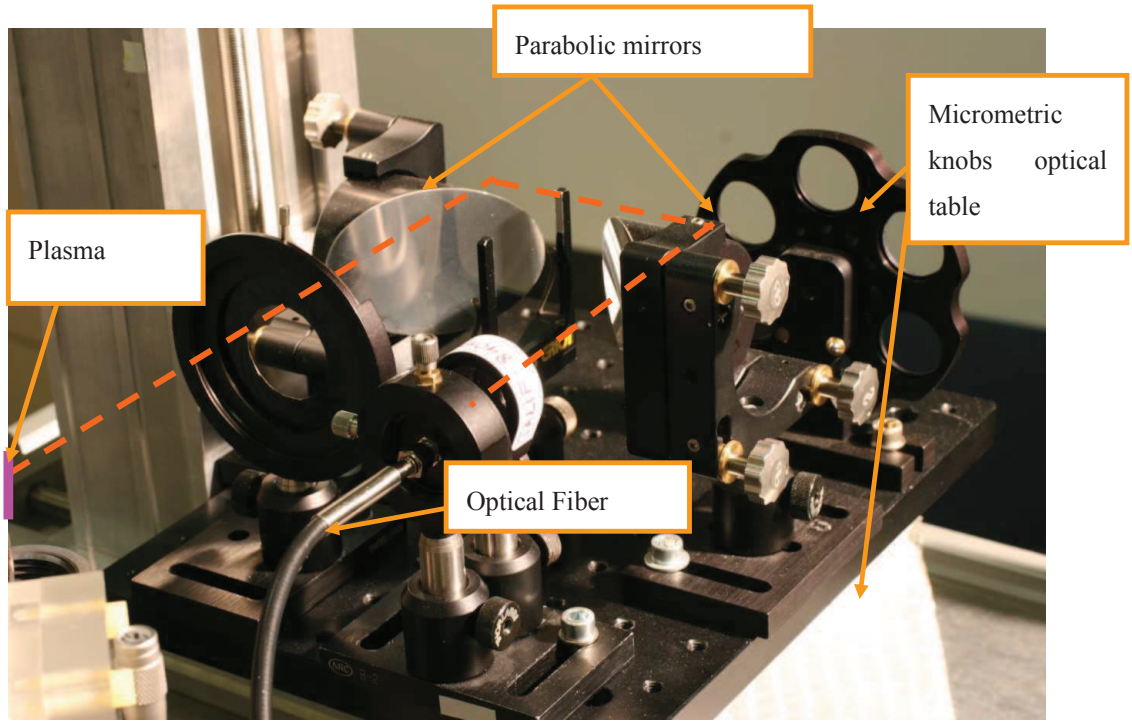

Figure 3.9 Photograph of the optical train for optical emission spectroscopy

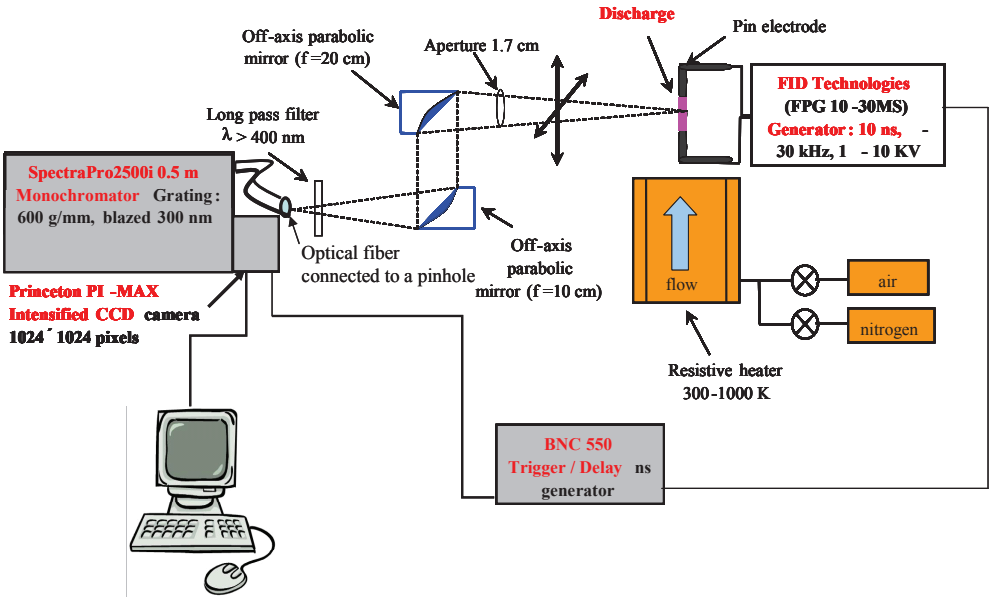

Figure 3.10 Schematic of the optical emission spectroscopy setup

Experimental set up

The optical train consists of two off-axis parabolic (OAP) mirrors (Janos Technologies UV-grade MgF2-coated aluminum mirrors of 50-mm diameter and focal lengths equal to 10 and 20 cm). The mirrors are placed in mirror mounts (Ultima U200-A38) with adjustment knobs for 3-D movement. An adjustable aperture is placed before the collecting OAP in order to control the collection solid angle. Light is collected and focused into a 2-m UV fiber optic bundle (Ocean Optics QP600-2-SR-BX). The bundle contains (LG-455-020) 19 fibers, with a core diameter of 200 μm each, arranged in a circular bunch at the collecting end, and in a 1D array at the entrance of the spectrometer. The entire light collection system is placed on a 20×25 cm optical table resting on an X-Z translation stage set (Velmex A4009K1-S4 UniSlide and B4909K1Unslide). As shown in figure 3.11, the spatial resolution of the optical system is controlled by inserting Melles Griot pinholes of various diameters (50 to 300 □m) at the focal point of the imaging off-axis parabolic mirror, right in front of the collecting optical fiber. In general the diameter D of the collection volume was chosen smaller than the plasma width to allow for spatial resolution.

The detection system described above provided a spectral resolution of about 0.4nm (full width at half maximum with the 600 gr/mm grating) and a spatial resolution down to 100 μm with the 50 μm pinhole.

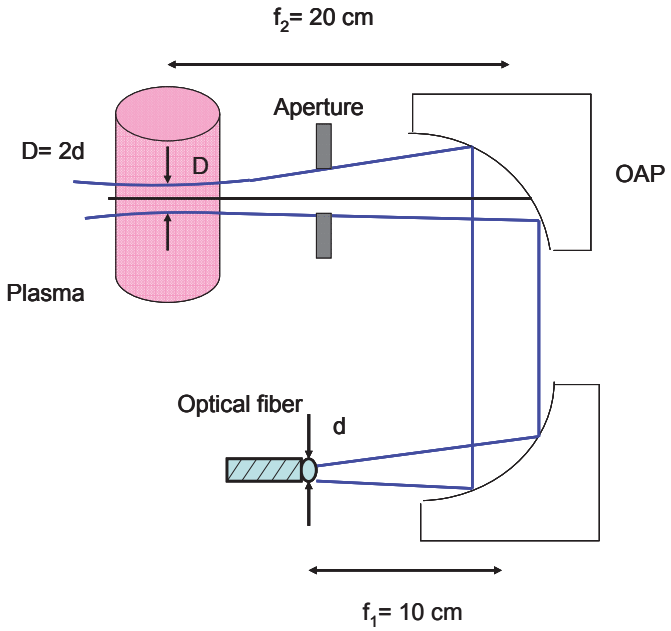

Figure 3.11. Spatial resolution of the experimental optical system

The light from the fiber optic bundle is sent into the side entrance slit placed at the focal point of a collimating toroidal mirror in a half-meter spectrometer (Spectra Pro 2500i), equipped with a fast ICCD camera (Princeton instruments, PI-MAX). The collimated light is diffracted by the grating and then re-focused by a second toroidal mirror onto the ICCD array of the PI-MAX camera. Rotating the mirror or grating changes the wavelength range observed by the camera. Spectra from 200-900 nm can be measured with this system.

The characteristics of the spectrometer, the intensified camera and the programmable timing generator are described in table 3.2.

Table 3.2 Spectrometer Characteristics

SpectraPro2500i monochromator	Characteristics
Mirrors	Original polished aspheric
Focal length	50 cm
Diffraction gratings	600, 1200 and 2400 grooves blazed at 300 nm
Entrance slit	100 μm at side entrance
Resolution	0.4 nm for the 600 gr/mm diffraction grating 0.2 nm for the 1200 gr/mm 0.1 nm for the 2400 gr/mm
Princeton PI-MAX Intensified CCD camera	
Image intensifier	Micro-channel plate (MCP)
Mode	Gate mode
CCD array dimensions	1024x1024 pixels
Pixel dimensions	13 x13 μm
Shutter type	Electronic
Gain	Adjustable from1 to 255
Temperature control	Peltier-effect cooler at -20°C
Maximum background signal rejection ratio	5×10^{6}:1
Maximum image intensifier electronic gain	10,000
Minimum gate width	2 ns

Readout time	~1.2 s
Princeton Instruments ST-133 Controller with Programmable Timing Generator (PTG) Module	
ST-133 Timing mode	Internal sync
PTG Trigger	External
Operating mode	Gate mode

Camera principle and characteristics

The principles of operation of the PIMAX ICCD camera used in the present work are taken from report PI-MAX camera system manual. The spectra are obtained by running the camera in spectroscopic mode. The ICCD set-up and a schematic of its different components are shown in figure 3.12. In the PI-MAX camera, the input image is focused onto the photocathode of an image intensifier tube. The image intensifier tube is an evacuated tube which comprises the Photocathode, Microchannel plate (MCP) and a Phosphor screen. That light is then coupled to the CCD array using a fused fiber-optic bundle from the output of the image intensifier to the front side of the CCD window. The image at the output of the image intensifier is translated to the input of the CCD at the same size. After being detected by the CCD, the image is read out to the Controller, where it is digitized and transferred to the computer for processing via a high speed data link.

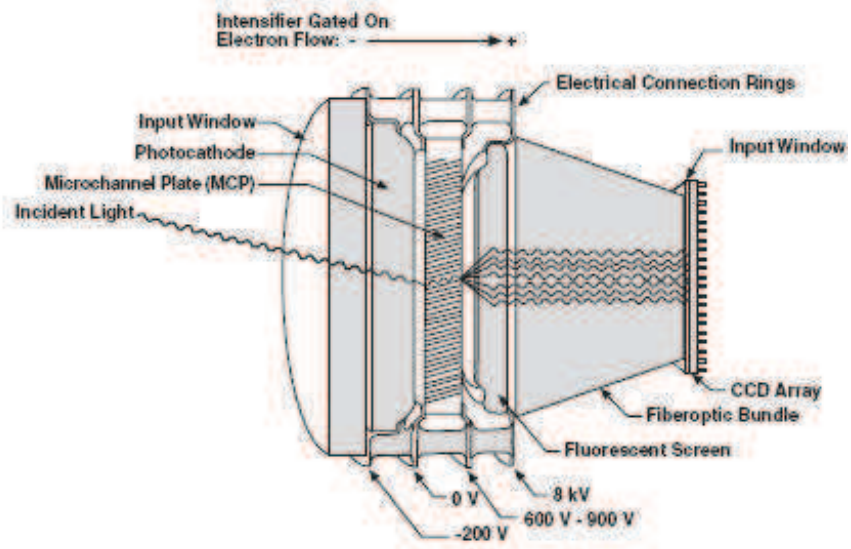

Figure 3.12. ICCD set-up and schematic of the different components taken from PI-MAX camera System Manual

Electrons are attracted to more positively charged surfaces and are repelled by more negatively charged surfaces. This principle is used to control electron flow through the intensifier tube, changing the photocathode voltage with respect to the voltage at the MCP input is used to switch (gate) the intensifier on and off.

Calibration of the ICCD as a function of gate width and number of accumulations:

The system allowed time-resolved measurements down to 2 ns for OES. In order to improve the signal-to-noise-ratio, the output spectra were obtained by accumulating the signal over a high number of single frames. Between two measurements, during the readout phase, the CCD arrays were emptied from the accumulated charges. This CCD allows numerical accumulation which is based on summing the signal from repeated acquisitions and improves the signal-to-noise ratio. Hence the optimization of each measurement involved the optimization of the number of on-CCD accumulations, the exposure time and the gate delay. These parameters were chosen to obtain the highest signal-to-noise ratio and the highest signal intensity without reaching saturation of the CCD.

It was found (Pai, 2008) that with this detection system the output signal does not evolve linearly with the number of accumulations and the gate width. A calibration was therefore performed. Figure 3.13 and figure 3.14 represent the evolution of the photon count as a function of the gate width and the number of accumulations, respectively.

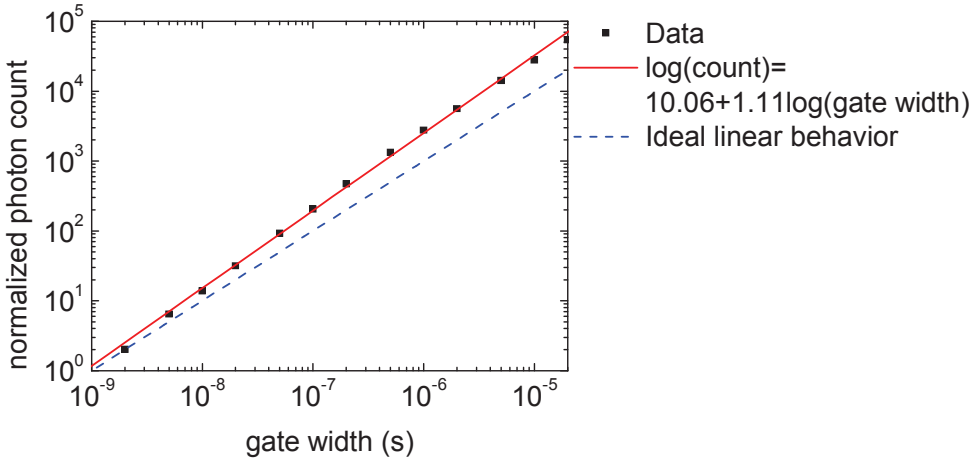

Figure 3.13. Measured photon count as a function of gate width (symbols) fitted with a line compared to ideal linear behavior (dotted line) taken from Pai, 2008.

The measurements shown in figure 3.13 were obtained by Pai (2008) with a radiance standard source (OL550 tungsten filament lamp). In this case, he fixed the number of accumulations and varied the gate widths. For the second correction, shown in figure 3.14, he maintained the same value of gate width for all measurements and varied the number of accumulations. When a measurement was taken near the CCD saturation limit, a second measurement was taken at reduced lamp intensity.

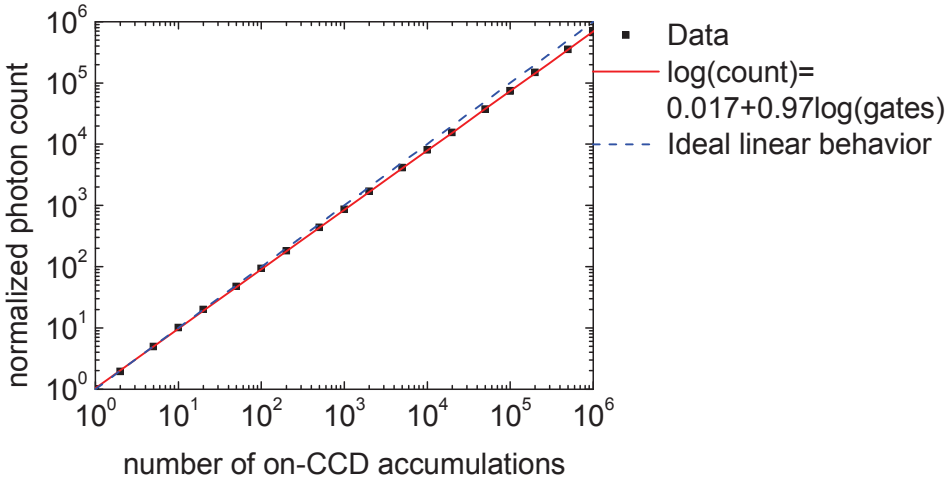

Figure 3.14. Measured photon count as a function of the number of on CCD accumulations (symbols) compared to ideal linear behavior (dotted line)taken from Pai, 2008

We notice that for low numbers of accumulations of on-CCD and low gate widths, as shown in the figures above, the measured signal has an ideal linear behavior. It also appears that for high numbers of on-CCD accumulations the difference with the ideal linear response is minor and much more significant for large gate widths. These dependencies allow us to correct the response of the camera for gate width and on-CCD accumulation.

Spectral response of the optical detection system

The spectrometer was calibrated in intensity for the first and second positive systems of N_2 with a tungsten radiance standard (OL550) in order to obtain absolute densities from the measured emission spectra. The intensity calibration was performed for wavelengths from 350 nm to 800 nm, using an Optronics Laboratory model 550 lamp, which is a modified GE-18A/t10/2p tungsten ribbon filament placed behind a sapphire window for optimum ultraviolet transmission. Its spectral radiance is calibrated from 250 to 800 nm and has a quoted accuracy better than 3%. Figure 3.15 provides the radiance of the lamp for a current of 15A.

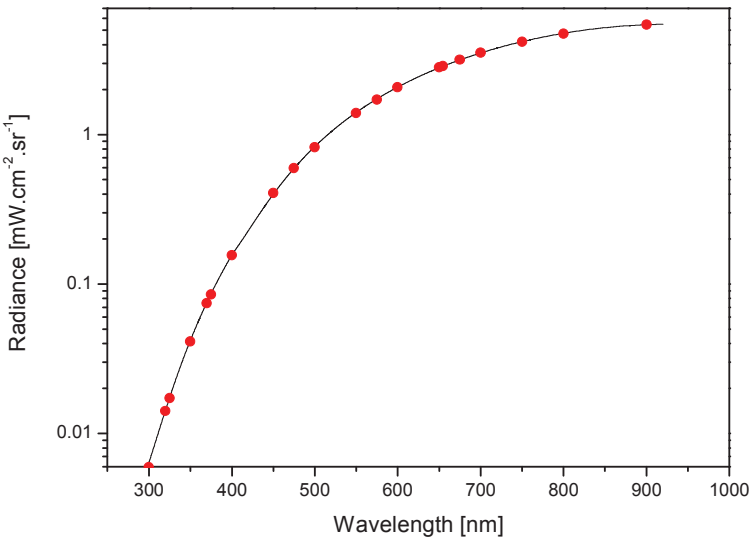

Figure 3.15. Radiance of the tungsten lamp OL550 for a current of 15A (taken from Optronic Laboratories, Report of Calibration)

We then compare the known spectral radiance emitted by the radiance standard with the response of our system to this source signal.

The spectral radiance L_λ is a function of the wavelength, the spectral width of the detection, $\Delta\lambda$, the area of the emitting surface A, the solid angle Ω, the angle of incidence θ (equal to 0 here since we work under normal incidence) and the radiative power Φ_λ

$$L_\lambda = \frac{\mathrm{d}^5\Phi_\lambda}{\Delta\lambda \cdot \mathrm{d}A \cdot \mathrm{d}\Omega \cdot \cos\theta}\ ;\quad \frac{\Phi_\lambda[\mathrm{W}]}{\Delta\lambda[\mathrm{nm}] \cdot A\left[\mathrm{cm}^2\right] \cdot \Omega[\mathrm{sr}]} \qquad \text{Eq 1}$$

To obtain the system response, we replace the light source to be calibrated (i.e. the plasma discharge) with the standard of radiance. For absolute calibration, we use the same detection system, camera settings, collection optics etc, for the radiance standard as in the plasma discharge experiments. We also position the tungsten filament at the same focal point of the collecting system. Figure 3.16 shows the system intensity response to the tungsten lamp in arbitrary units (counts).

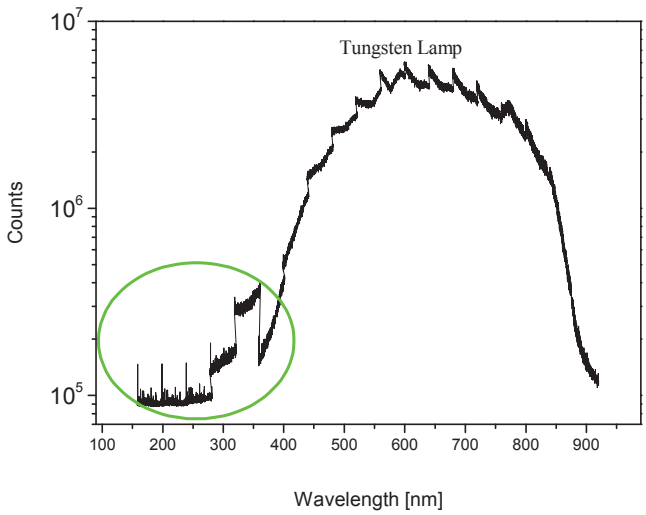

Figure 3.16. Tungsten lamp signal recorded with the spectrometer from 200 to 920nm.

Typical ICCD acquisitions spanned spectral windows of 40 nm when using the 600 gr/mm grating. It can be seen that in the 250-350 nm region, there are two windows with higher intensity. This is most probably due to straylight or internal reflections inside the spectrometer. Thus these windows were avoided in the experiments. Because air is optically thick below 200 nm, the signal detected below that wavelength (about 90 000 counts) is a background signal (due to dark noise and stray light) that must be subtracted from the spectrum measured at higher wavelengths.

We then divide the recorded lamp signal of Figure 3.16 (with the background subtracted) by the radiance curve of Figure 3.15. We then obtain, as shown in Figure 3.17, the absolute spectrometer response. This curve allows us to convert relative spectra into absolute spectra, and hence to obtain the densities of the species measured by emission spectroscopy.

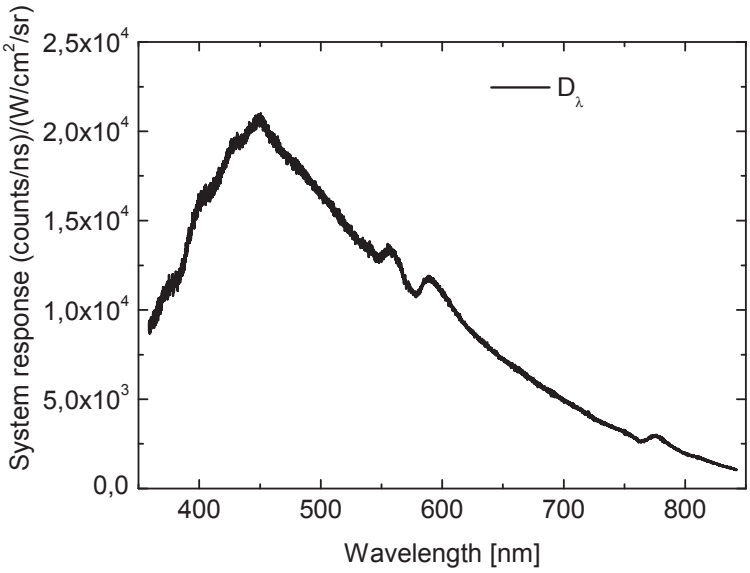

Figure 3.17. Spectral response curve of the OES detection system (counts/ns)/ (W/cm^2 sr) with the 600 gr/mm grating.

3.3 Cavity Ring- Down Spectroscopy (CRDS)

To measure the $N_2(A)$ electronic excited state of nitrogen, the technique of Cavity Ring Down Spectroscopy was used. A photograph of the experimental setup is presented in Figure 3.18.

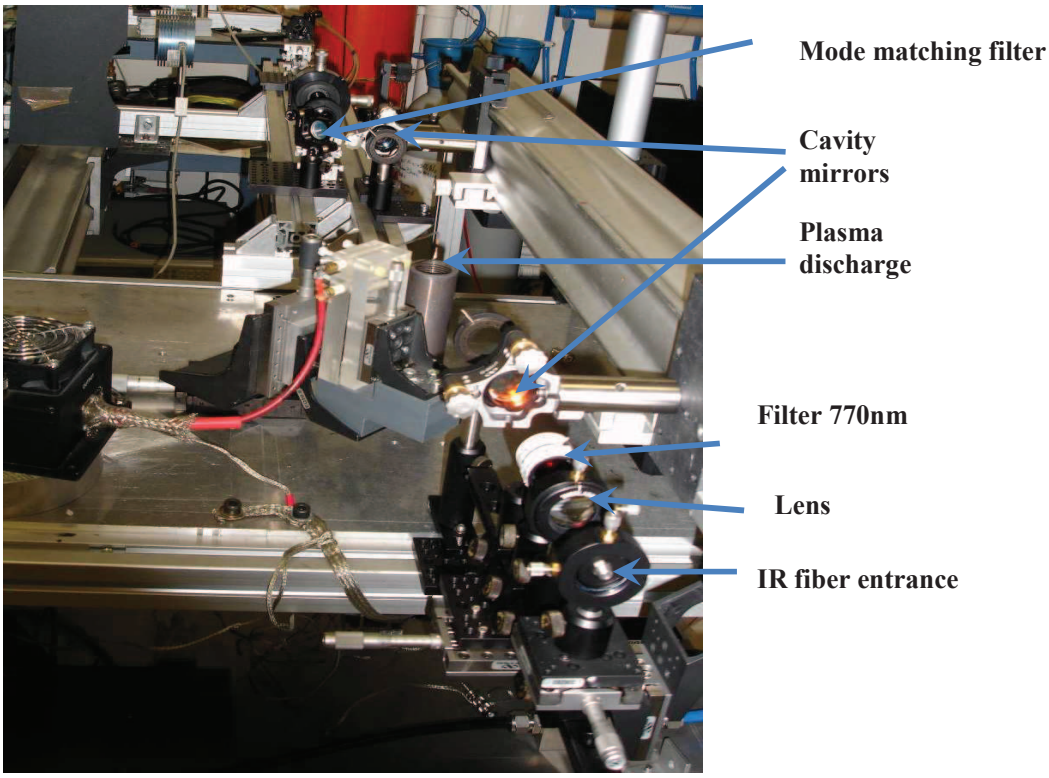

Figure 3.18. Photograph of the cavity ring-down spectroscopy setup

A schematic of the CRDS setup with the atmospheric pressure nitrogen/air discharge is shown in Figure 3.19. The CRDS cavity consists of two plano-concave mirrors (Los Gatos Research) of high reflectivity, R > 99.97%, and radius of curvature r = 0.5 m. The beam of a tunable pulsed dye laser, Continuum ND 6000, pumped with a Precision PL 8010 Nd:YAG laser was coupled into the cavity. The output laser energy per pulse was up to 40 mJ at 770 nm, the laser spectral width was 0.1 cm^{-1}, and the repetition frequency was 10 Hz.

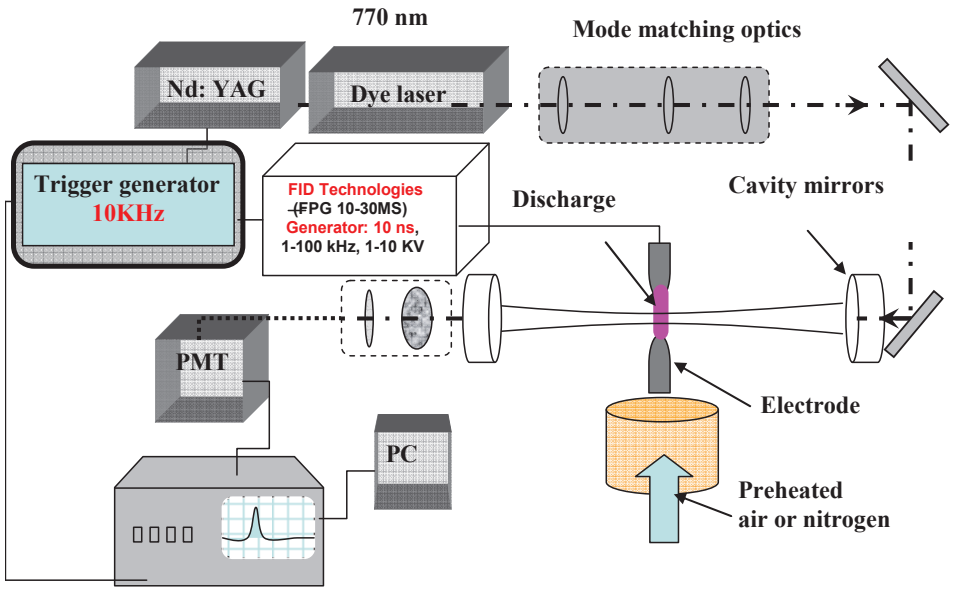

Figure 3.19. Cavity ring down spectroscopy and discharge setup.

The density of $N_2(A)$ was determined by probing the (2←0) vibrational band of the N_2 first positive system (B ← A) in the vicinity of 770 nm. This spectral region was chosen because it contains some of the strongest absorption lines and it allows access to the $N_2(A, v = 0)$ density. The dye laser output sent into the cavity was attenuated down to a few hundreds of μJ per pulse by reducing the power of the Nd:YAG laser. Then it was focused inside the cavity to match the TEM00 mode of the cavity. The mode-matching optics were calculated using matrix-optics and implemented using plano-convex lenses of focal lengths 5, 10, and 50 cm (Stancu et al., 2010).

In general the CRDS consists of an absorption volume bounded by mirrors with high reflectivity over the wavelength range of interest. For the present case the absorbing plasma is confined in a 1-2 mm^3 volume at the center of the cavity. The range of wavelengths covered by any particular set of high reflectivity mirrors depends on the wavelength itself, the nature of coating etc. The typical range is a few tens of nanometers.

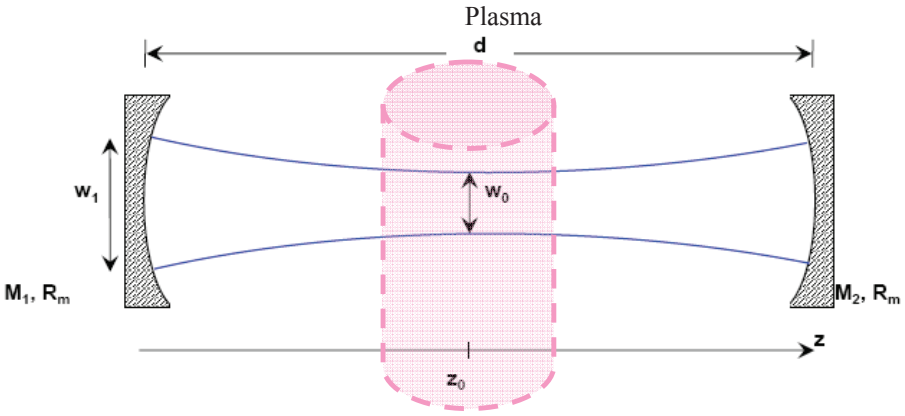

Figure 3.20. Typical ring down spectroscopy cavity parameters

The ring-down cavity is formed by two identical plano-concave mirrors whose radius of curvature R_m is typically between 25 cm and 1 m (Berden et al., 2000). Following (Yalin et al, 2002), special attention was paid to the choice of cavity geometry. We used mirrors with radii of curvature appropriate to the establishment of a stable cavity configuration (Yariv, 1989). Because the nanosecond atmospheric pressure discharges are generated in preheated gas at 1000 K, the presence of large temperature gradients affects the refractive index of air and causes beam steering effects (the plasma acts like a lens). Spuler and Linne (2002) calculated the beam-steering displacement of a Gaussian beam for different values of the so-called cavity parameter, g, defined as (see previous chapter):

$$g = 1 - \frac{d}{R_m} \qquad \text{Eq 2}$$

where d is the cavity length and R_m the radius of curvature of the two identical mirrors. The two cavity mirrors are designated by M_1 and M_2. w_0 and w_1 are respectively the waist of the beam in the middle of the cavity, where the plasma is, and the waist of the beam on the cavity mirrors. Figure 3.20 shows a schematic of the cavity and the cavity parameters designation.

If the two mirrors of the cavity are different, they will have two distinct cavity parameters respectively g_1 and g_2. The plot of g_1 against g_2 is shown in figures 3.21 and 3.22. Areas bounded by the curve $g_1\ g_2 = 1$ and the axes correspond to stable cavities. Cavities at points exactly on the line are at the edge of the stable region; small variations in cavity length can

cause cavity instabilities. The cavity length was chosen to be 0.67 m and the radius of curvature of the mirrors was R_m = 0.5 m, which corresponds to g equal to -0.34. This was a good compromise for our experimental conditions as will be demonstrated in the following. This configuration provides a small beam waist (FWHM = 0.4 mm), while maintaining a low sensitivity to beam steering effects.

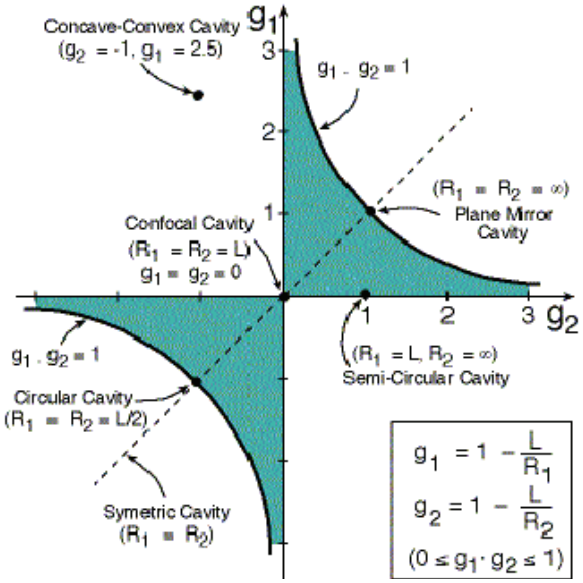

Figure 3.21. Stability diagram for a two-mirror cavity. Shaded areas correspond to stable configurations (taken from www.weizmann.ac.il/Lasers)

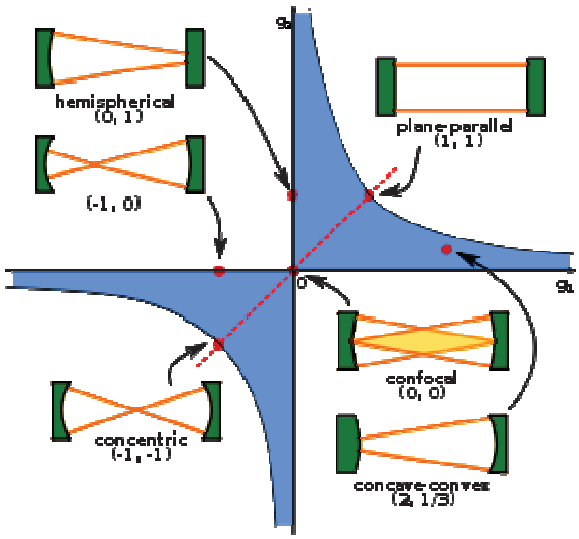

Figure 3.22. Various cavity configurations as a function of $g_1.g_2$

The stability region of the cavity is shown in figure 3.21 and 3.22 colored in green and blue, respectively. The line that lies along the $g_1 = g_2 = g$ corresponds to cavities with identical mirrors. The cavities for g = 1 (planar), g = 0 (confocal) and g =-1 (concentric) lie all on this line. It is important to note that these three cavity geometries, planar, confocal, and concentric, all lie on the stability boundary and are therefore prone to instability.

For a stable symmetric resonator, the beam sizes or the Gaussian spots w_0, $w_{1,2}$ of the cavity (see Figure 3.20) are calculated function of the g parameter as shown in figure 3.23 (taken from Spuler and Linne 2002).

Figures 3.24 shows the effect of misalignment with mode-matched Gaussian beam for different cavity parameter g. This graph has been taken from Spuler and Linne calculations. The two curves show the beam displacement for 1-mm input-beam offset and a 0.5-deg tilt per unit cavity length, respectively.

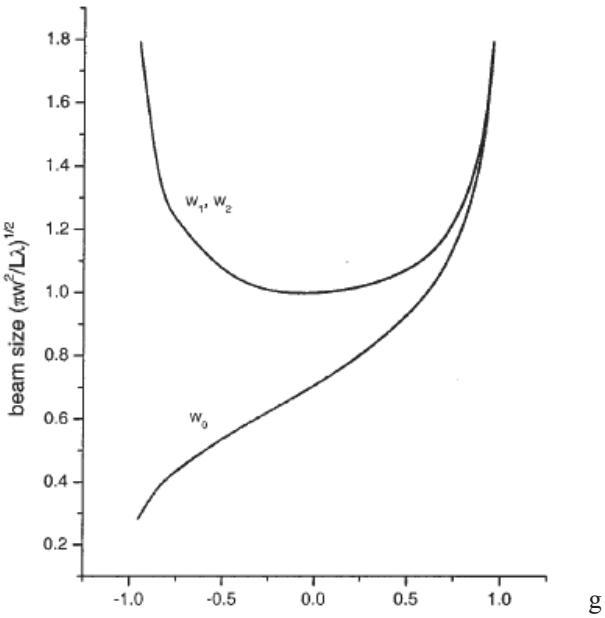

Figure 3.23. Gaussian input: beam size with perfect mode matching, w_0 is the beam size at the center of the cavity, and $w_1 = w_2$ is the beam size at the cavity mirrors (taken from Spuler and Linne, 2002).

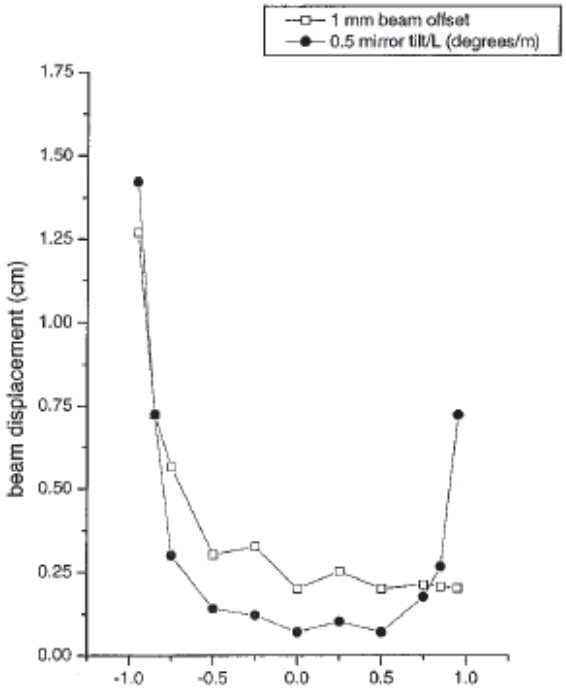

Figure 3.24. Effects of misalignment with mode-matched Gaussian (taken from Spuler and Linne, 2002).

It appears that the cavity remain stable with a minor displacement of the beam for the region where g parameter is in the range between -0.5 and 0.5. Thus, in order to minimize the beam steering effects due to strong temperature gradients induced by plasma or gas heating system (the gas was preheated a 1000 K), a cavity with g between -0.5 and 0.5 is required.

An important feature in designing our cavity is the beam size at the cavity centre. The cavity parameter g taken between -0.5 and 0 allows a relatively small spot within the range where the beam displacement is minimum. An essential criterion for our experimental work was the beam to be smaller than the typical plasma diameter (less than 500 μm). Taking in account all these conditions an optimal value for the cavity parameter g=-0.34 was chosen. For these conditions , in our case , we wanted a width w_1= 0,418 mm and w_0=0.24 mm. Using a computer program under MAPLE (Stancu, private com) we obtained the optimized parameters listed below:

Experimental set up

d_0=150 mm f_1=50 mm

d_1=141.93 mm f_2=100 mm

d_2=63 mm f_3= 500 mm

d_3=575.07mm

Another important aspect was the effect of the laser linewidth on the measured densities. The profile of measured lateral absorbances is determined as a ratio of the laser intensities entering and exiting the plasma, according to:

$$A(x) = \ln(I_0/I) \qquad \text{Eq 3}$$

where A is the absorbance of plasma per path (defined as A = k(ν)l, where k(ν) is the absorption coefficient, and l is the length of the absorbing layer), I_0 is the laser signal intensity when entering the absorbing media and I is the intensity of the signal transmitted through the absorber. Yalin and Zare, (2002) showed that the measured integrated line absorption coefficient is not conserved when the laser linewidth is larger or comparable with the absorption linewidth, and when the peak absorbance, $\ln(I_0/I)_{\max}$, is larger or comparable with the cavity loss, $(1-R)$. For our conditions the integrated absorption coefficients were essentially independent of the laser linewidth. Only the largest peak absorbances led to an underestimated value of the density (a few percent).

The cavity mirrors were mounted on U100-G2K Micro Control supports, which allows for tilting without changing the cavity length. Their position was chosen to allow accurate adjustment using micrometer screws. The alignment permits to keep the laser pulse bouncing back and forth inside the cavity. In this way it is possible to achieve hundreds to thousands round trips before decaying due to the cavity losses. A PMT and light collection optics are positioned behind the output mirror to record the intensity of the light pulse transmitted through the mirror on each round-trip of the cavity. Because the decay time is independent on the laser pulse intensity, the influence of pulse-to-pulse intensity variations is negligible (if constant species densities are assumed).

The light leaking out of the cavity was filtered by two interferential bandpass filters (CVI-F10-770) with peak transmittance at 770 nm and a band transmissivity of 10 nm (FWHM). It was

then focused into a 5-m long optical fiber and transmitted to a photomultiplier tube (PMT) with 1.4-ns risetime (Hamamatsu H9305-3). The PMT signal was digitized by a LeCroy Waverunner 434 oscilloscope (350 MHz analog bandwidth, eight-bit vertical resolution) and recorded by a computer under Labview. software. Faraday cages were used to shield the PMT system, which was very sensitive to the electromagnetic noise produced by the discharge. The plasma discharge, laser system and detection system were synchronized by a Berkeley Nucleonics (BNC) 555 four-channel gate and delay generator. The BNC triggered the flash lamp and Q-switch of the Nd:YAG laser, and the detection system at 10 Hz, and the discharge at 10 kHz with appropriate delays. For density measurements, one hundred decay curves were averaged at on- and-off-resonance wavelengths. Spectral scans were acquired at wavelength steps of 5 pm and spatial scans were taken with steps of 0.1 mm across the diameter of the discharge (Kaddouri et al. 2009).

The empty cavity provides a theoretical ring-down time up to 6 μs, but laser instability, coupling of several laser modes, scattering, and degradation of the mirrors reduce the observed empty-cavity decay time to about 2 μs

The lateral profiles of ring-down times was fitted with a Gaussian function which was then Abel-inverted to obtain the local absorption coefficients. The effective absorption length in the discharge was found to be about 0.6 mm in nitrogen plasma.

3.4 Two-Photon Absorption Laser Induced Fluorescence (TALIF)

Two-photon absorption laser-induced fluorescence spectroscopy (TALIF) was used to measure the density of ground state oxygen atoms, using two-photon absorption at 225 nm and fluorescence at 844 nm (Niemi and al, 2005). A schematic of the experimental set up is presented in figure 3.25 (Stancu et al. AIAA 2008).

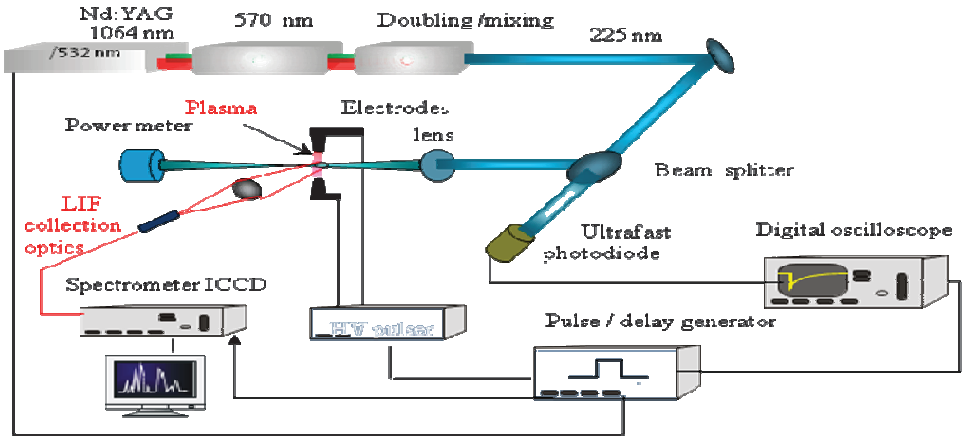

Figure 3.25. Two-Photon Absorption Laser-Induced Fluorescence setup.

The TALIF experiments were carried out using a commercial laser system which consists of a Nd:YAG laser (Continuum Precision PL 8010), providing second harmonic light at 532 nm with a repetition rate of 10Hz, pumping a tunable dye laser (Continuum ND 6000). The output of the dye laser at about 570 nm was then doubled and mixed with the residual 1064 nm output beam of the Nd:YAG laser to obtain wavelengths between 224 and 226 nm. The pulse energy and duration are 1mJ and 6ns respectively.

This UV radiation is separated by a beam splitter (BS) into two unequal parts. The largest portion of the beam (>90%) is focused by a lens of f = 35cm, 3 cm after the air plasma studied. This defocusing is used to avoid saturation of the TALIF signal. The output power is measured by an Astral power meter (AD 30). The remaining portion of the beam is used as a reference

signal detected by an ultrafast photodiode PD UV (Alphalas, UPD-2000-UD, 200 ps rise time). This reference signal is recorded by a digital oscilloscope (Lecroy, 2GHz bandwidth).

As in LIF, the fluorescence is detected perpendicular to the exciting laser beam and to the plasma channel. The fluorescence optics consist of two off-axis parabolic mirrors with focal lengths of 10 cm and 20 cm respectively, which guided the fluorescence signal through a 2-m optical fiber to the slit of a spectrometer (Spectra Pro 2500 i), equipped with a fast ICCD camera (Princeton Instruments, I-max), connected to a PC where the measured spectra were recorded.

The synchronization of the plasma discharge with the laser, LIF and PD detection systems was achieved with a Berkeley Nucleonics (BNC 555) four-channel pulse delay generator (1 ns RMS jitter). The BNC triggered the flash lamp, the Q-switch of the Nd :YAG laser and the detection systems at 10 Hz, and the discharge at 10 kHz with appropriate delays. (Stancu et al., 2010)

The atomic oxygen fluorescence signal is collected from a volume formed by the intersection of the three cylinders of the plasma, the laser beam and the collecting channel defined by the solid angle of the optics used. This is illustrated in figure 3.26. The dimensions of the cylinders are: 400 μm for the laser beam, 600μm for the fluorescence collection volume. The discharge diameter is estimated to be 450μm The volume for the atomic oxygen fluorescence signal is then 0.05 mm^3 .

Depending on the data quality, up to 200 numerical averages of the fluorescence spectra and laser intensity temporal profiles were performed. Xenon is used here as the calibration gas to convert experimental data into absolute concentrations.

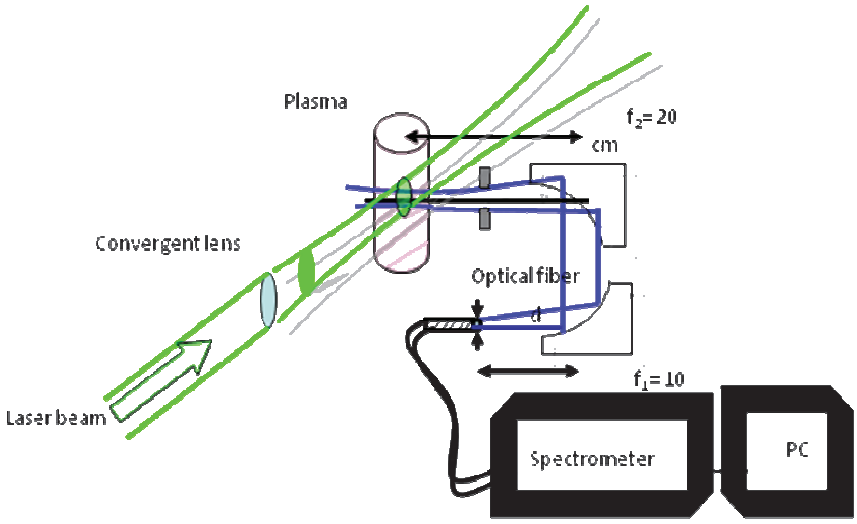

Figure 3.26. Collection volume for the atomic oxygen fluorescence signal..

3.5 TALIF calibration with noble gases

The method of TALIF calibration with noble gases for the determination of absolute atomic ground state densities has been introduced by Goehlich et al, 1998. It represents a technically simple alternative to the use of atomic reference sources like the flow-tube reactor with titration. The method is based on comparative TALIF measurements using a noble gas as a reference with a two-photon resonance spectrally close to that of the atomic species to be quantified. Xenon is well suited for the purpose of the present measurements calibration of atomic oxygen as shown in figure 3.27.

Several rules have to be observed. The conditions of excitation and detection should be similar for both the oxygen and xenon transitions. This includes the properties of the laser output and the optical detection system. Only the unsaturated quadratic signal response allows a quantitative comparison. The various saturation effects (ground state depletion, photo-ionization out of the excited state, amplified spontaneous emission via fluorescence channels or artificial particle generation, e.g. by photodissociation) exhibit rather complex intensity dependences with individual thresholds, therefore the laser intensity has to be kept as low as possible. The atomic oxygen density is given by:

$$n_O = X \frac{S_O}{S_{Xe}} n_{Xe} \qquad \text{Eq 4}$$

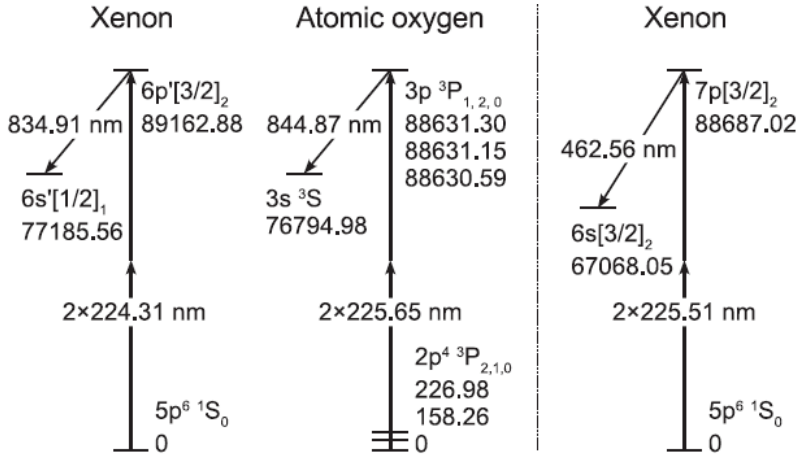

Figure 3.27. Matching two-photon excitation schemes of atomic oxygen (taken from Niemi et al., 2005)

The first scheme of Xe of figure 3.27 was used in our experiment (Stancu et al., AIAA 2009). Where n_{Xe} and n_O are respectively the Xe and O density, S_O and S_{Xe} are the 'normalized' fluorescence signal S (integrated over fluorescence wavelength, excitation wavelength and time, and normalized to the squared laser pulse energy). X is constant, that takes into account the absorption cross-sections and the branching ratios of O and Xe.

For low pressure media (collisionless case) the calibration factor X depends only on atomic cross sections in absorption, Einstein coefficients for emission and experimental constants (solid angle, sensitivities, etc). With increasing pressure, the situation becomes more complex. Collisional quenching reduces the effective branching ratio of a spontaneous transition i → k:

$$a_{ik} = \frac{A_{ik}}{A_i + Q_i} \qquad \text{Eq 5}$$

A_i denotes the total spontaneous emission rate of the upper level, which is equal to its reciprocal radiative lifetime τi , and (see prevous chapter)

$$Q_i - \sum_q k_q^i n_q$$ Eq 6

the effective quenching rate, which can be expressed by the collision partner densities n_q and the corresponding quenching coefficients $k^i{}_q$.

The collision partner densities depend on the gas temperature T_g according to the ideal gas law as well as the quenching coefficients according to the kinetic theory. For a thermal velocity distribution, the following relation holds:

$$k_q^i - \sigma_q^i \langle v \rangle - \sigma_q^i \sqrt{\frac{8 k_B T_g}{\pi \mu}}$$ Eq 7

with mean collision velocity <v>, Boltzmann's constant k_B, reduced mass of the colliders μ, and collision cross section σ_q^i , which generally exhibits a modest temperature dependence .

The fine structure of atomic oxygen has to be considered in the present case. The ground state and the two-photon excited state are triplet states. The splitting of the excited state (0.7 cm−1) can only be resolved partially with respect to the room temperature Doppler width (0.274 cm^{-1}) in contrast to the substantial ground state splitting (227 cm^{-1}), which is comparable to the mean kinetic energy at room temperature ($k_B T_g$ = 209 cm^{-1} for T_g = 300 K). If the ground state exhibits a thermal population distribution, only one ground state sub-level (with total angular momentum quantum number J and energy EJ) has to be probed in order to determine the total ground state population by considering the corresponding Boltzmann population fraction:

$$\frac{n_J}{\sum_J n_J} = \frac{(2J+1) exp\left(-E_J / k_B T_g\right)}{\sum_J (2J+1)\, exp\left(-E_J / k_B T_g\right)}$$ Eq 8

The applicability of the calibration method requires a knowledge of atomic data, namely the radiative lifetimes and the corresponding quenching coefficients of the laser-excited states as well as the two-photon excitation cross-section ratio. These data were taken from Niemi et al. and NIST atomic data.

Chapter 4: Results on the validation of the two-step mechanism

The two-step mechanism suggests both a chemical effect, which is the atomic oxygen production, and a thermal effect, that is heating of the gas by the discharge (see chapter 1, ultrafast mechanism) as a result of the following reactions:

$N_2 + e \rightarrow N_2(A, B, C) + e$

$N_2(A, B, C) + O_2 \rightarrow N_2 + 2O + heat$

Both aspects were explored here.

In this chapter, we present the main results obtained during the experimental investigation of nanosecond repetitively pulsed (NRP) discharges at atmospheric pressure in air or nitrogen preheated at 1000 K, for a range of repetition frequencies from 1 to 30 kHz. This study was conducted under a well-defined discharge reference case, allowing consistent experimental conditions for the comparison of different types of experiments.

We started this work by evaluating quantitatively the energy available in the system. For this purpose electrical measurements were performed to estimate the energy delivered per each pulse. Then, experiments were conducted to determine the electron density of the plasma by measuring the line broadening of the H_α emission. We then move to optical emission spectroscopic (OES) investigations of the NRP discharge. The principal chemical species emitted by the plasma in the reference case conditions were identified. We applied then OES to determine the temporal evolutions of the rotational and vibrational temperature of N_2(C-B). The rotational temperature was assumed to be equal to the translational temperature of the plasma. These measurements allowed proving the ultra-fast heating of the gas by the NRP discharges. To better understand the

chemical effect of the NRP discharge and in order to prove that the two-step mechanism is the dominant O production path for our experimental parameters, the time evolution of the absolute densities of $N_2(C)$ and $N_2(B)$ nitrogen excited states were measured.

Section 4 of this chapter is devoted to the measurement of $N_2(A)$ metastable by Cavity Ring Down Spectroscopy (CRDS), which is another key nitrogen species for the two-step mechanism. The densities and the lifetime of $N_2(A)$ in air and in nitrogen NRPD were compared.

Section 5 presents measurements of the temporal evolution of O density produced by the NRPD, measured by TALIF. This measurement was essential for the direct validation of the two-step mechanism.

In the last section, a summary of the experimental results together with the validation of the two-step mechanism for O production by NRP discharges in air at atmospheric pressure are presented. Finally the energy deposited in the two-step mechanism, which includes the energy dissociation of oxygen and the energy for heating the gas, is compared to the electrical energy deposited per pulse.

4.1. Reference discharge parameters and electrical measurements

The experimental setup allows changing the discharge pulse characteristics such as the applied voltage, the repetition frequency, the gap distance and it permits also to vary the discharge gas parameters such as the gas composition or the gas input temperature.

In order to compare the results of different experiments, we have defined the conditions of a discharge reference case. We have then electrically characterized this reference case (in terms of current, voltage, power and energy) for literature comparison and for concluding on the efficiency of the NRP discharges in oxygen production (as shown in section 4.6).

4.1.1 Discharge reference case

The discharge reference case is defined as follows:

- NRP discharge was used in the filamentary regime. The applied voltage between electrodes was fixed at about 6.6 ± 0.2 kV,
- Gap distance: 4 mm ± 0.5 mm,
- Pulse repetition frequency: 10 kHz,
- Air flow:: velocity of about 1 m/s, preheated at 1000 K and at atmospheric pressure, the flow was directed from the ground electrode (bottom) to the positive high-voltage electrode (on top).

4.1.2 Electrical measurements: discharge energy

The voltage across the electrodes was measured with a 100-MHz bandwidth high-voltage probe (Lecroy PPE20kV), connected in parallel with the electrodes. The discharge current is measured with a Pearson coil current monitor (Model6585) with a nominal 1.5-ns rise time, placed around the wire of the output of the pulse generator connected to the ground. The probe signals were recorded with a 1-GHz LeCroy Wavepro 7000 oscilloscope.

Figure 4.1 shows a sample of the voltage and current measurements taken while the discharge is running.

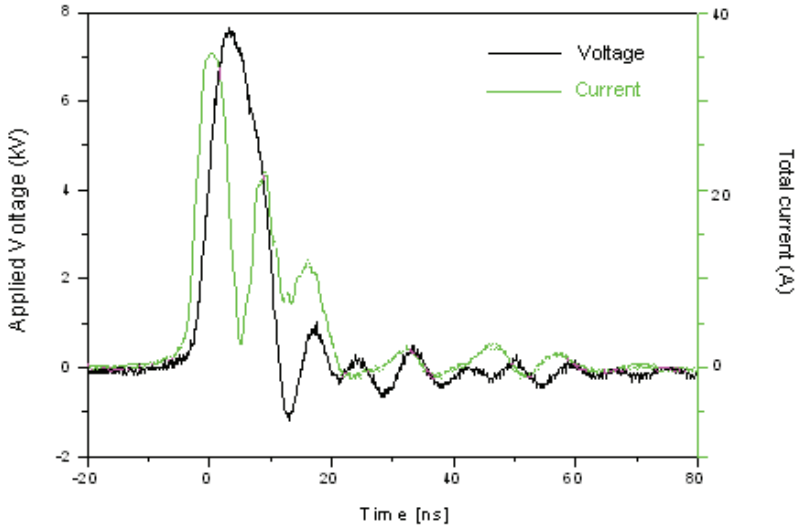

Figure 4.1 Sample of voltage and current measurements.

The plasma can be modeled by an RC circuit in parallel as shown in figure 4.2. The measured current is considered as the sum of the conduction current and the capacitive current.

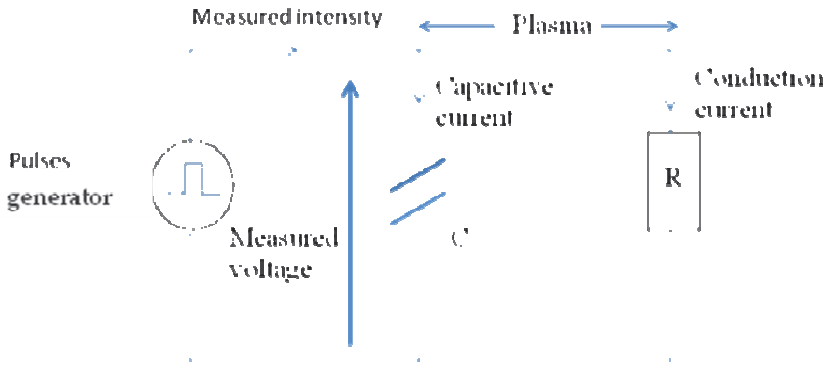

Figure 4.2 Electric circuit representing the filamentary discharge

To determine an equivalent resistance of the plasma in this circuit, the conduction current in the plasma needs to be expressed. Its value is equal to the difference between the total current and the capacitive current as shown by the formula:

$$I_{conduction} = I_{measured} - \frac{CdV}{dt} \qquad \textbf{eq. 1}$$

Samples of the total and the conduction current with the applied voltage in the discharge are illustrated in figure 4.3.

The power coupled into discharge is obtained as the product of the resistive current and voltage signals. The curves of the intensity and the voltage need to be well synchronized. The integration over the pulse duration τ provides the energy deposited per pulse as given by:

$$E = \int_{\tau} P(t)\,dt \qquad \textbf{eq. 2}$$

We have grouped the results of the electrical experiments in figure 4.4. (a)-(e), which shows the measured applied voltage, total current, conduction current, power, and energy deposited in the plasma for the reference case. Detailed descriptions of the experimental methods used for electrical measurements can be found in Pai's thesis (2008).

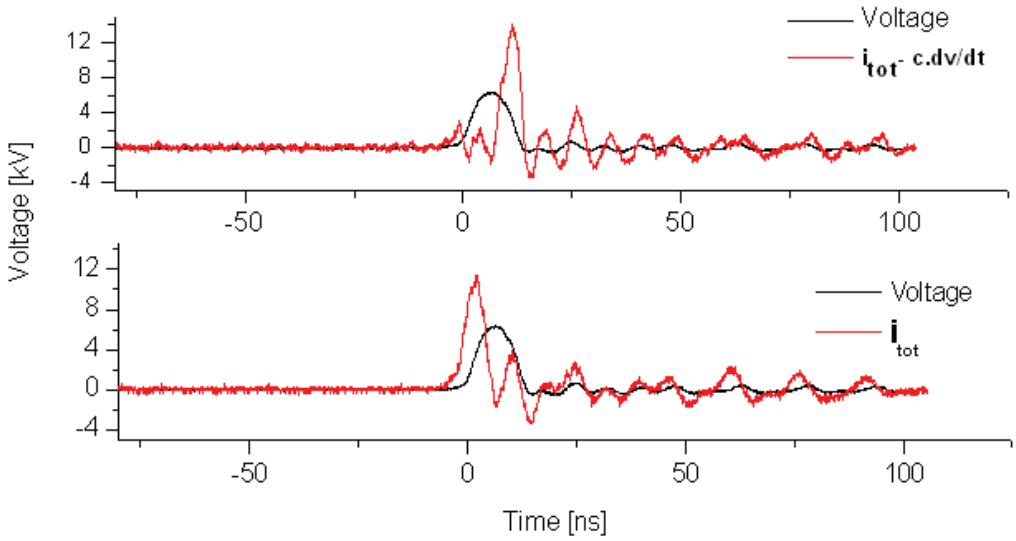

Figure 4.3 Sample waveforms of the applied voltage and of the total (top) and conduction (bottom) current

From figure 4.4 (e), we see that the energy deposited by the end of the pulse is 500±100 μJ. The 20% uncertainty in energy can be explained by several factors. First, the spark discharge erodes the electrodes, which can cause the gap distance to change during measurements, and requires an adjustment of applied voltage to obtain the reference case. As the energy varies strongly with the applied voltage (Pai, 2008), it follows that small variations in gap distance may cause larger proportional differences in energy. There is a variation on the order of 10% in the emission intensity of the NRP spark , which could be indication of a similar variation in power and energy.

The synchronization of the electrical measurements in figure 4.4 (a)-(e) has been achieved by measuring delays in detection of all relevant instruments. The detection delay of the high-voltage probe has been determined by measuring the arrival time of a voltage pulse after that of a coaxial cable section of negligible electrical length.

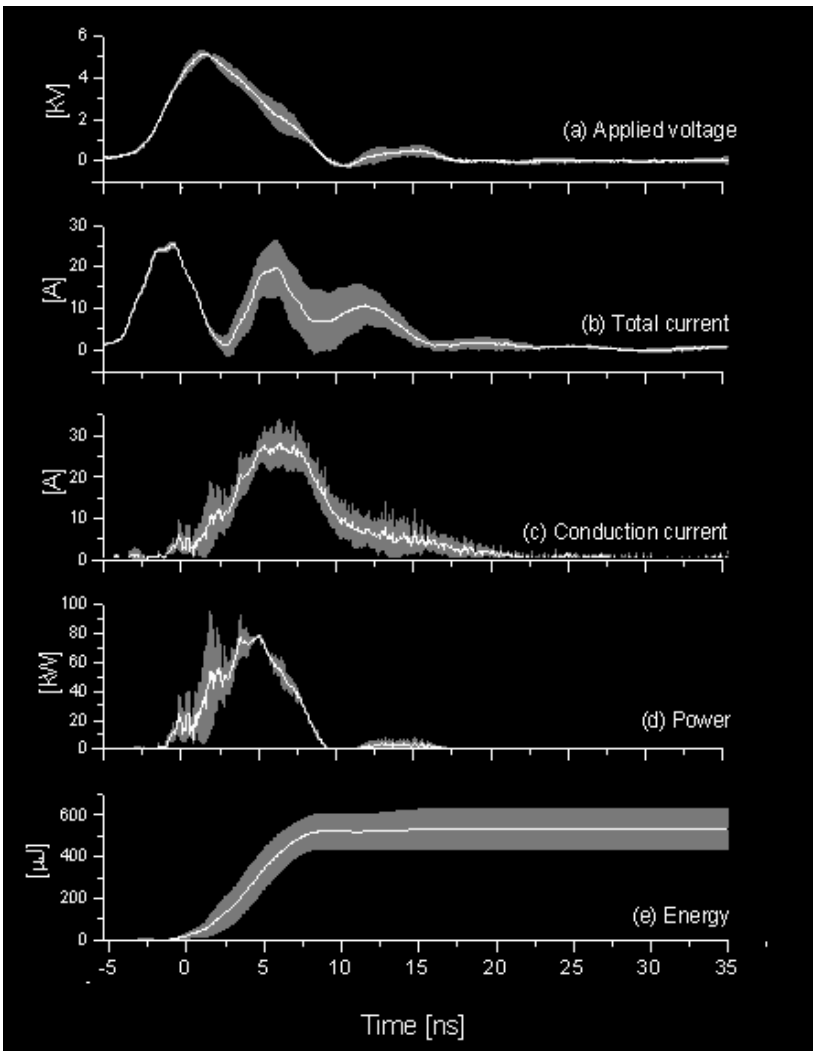

Figure 4.4 (a) measured applied voltage, (b) total current, (c) conduction current, (d) power and (e) energy, as a function of time.

4.2 Electron density determined by Stark effect of the H_α line

A key parameter of the NRPD is the electron density generated by the discharge. A high density of electrons will lead to the production of a large amount of active species, thus the interest of measuring this density. A method to evaluate the electronic density, n_e, in the discharge is to measure the emission of the Hα line (Marode 1977). In the presence of a high density of free electrons, Stark broadening is a very important broadening mechanism. If this density exceeds 10^{13} cm^{-3}, the profile of the Hα line

allows the determination of the electron density.

In our reference case, H_α emission does not appear. There are not enough water impurities in the laboratory air used to generate hydrogen in the plasma. So, in order to measure n_e we had to introduce about 4% of hydrogen flow premixed with air in the discharge.

We measured the emission spectra of the H_α line using a 0.5-m emission spectrometer system equipped with a grating of 1200 grooves per mm, which allows a spectral resolution of 0.15 nm (the same OES system as described for emission measurements). The H_α line is seen in a temporal window of 2 ns after the pulse. For each measurement point, a spectrum of the discharge in pure air without hydrogen was taken in the same experimental conditions to be subtracted from the one with H_α line, in order to separate it from the spectrum containing the underlying N_2(B-A) emission system, as shown in figures 4.5 and 4.6.

To determine the electron density in the discharge, we have used the profiles of Stark effect published by Stern (Stern et al, 1975). In figure 4.7 the time evolution of electron density is presented together with the current, voltage and the FWHM of H_α curves. The maximum electron density is in the range of $4(1.8)x10^{16}$ cm^{-3} (an error of 40 % was considered due to statistical errors).

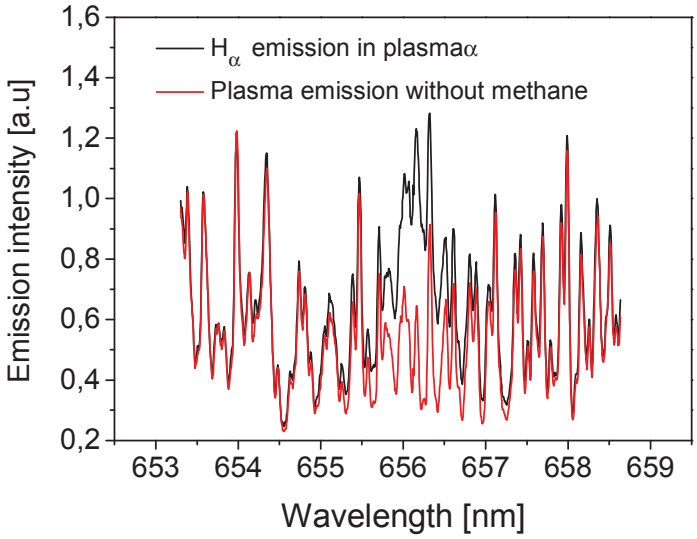

Figure 4.5 Typical Hα emission in plasma with and without hydrogen flow of 4%

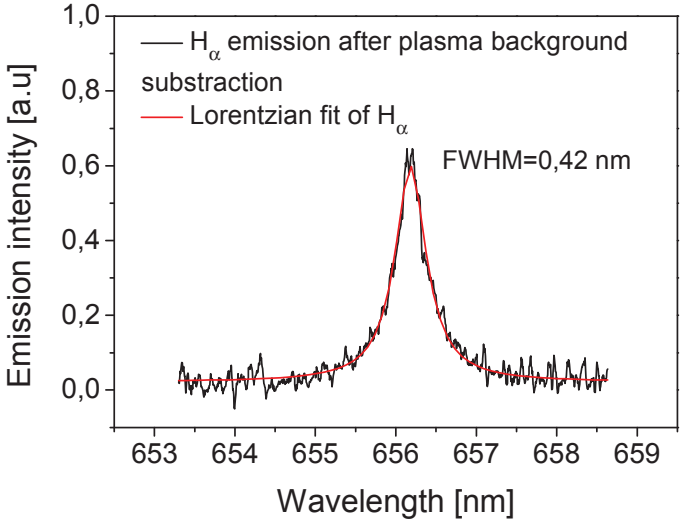

Figure 4.6 Typical Hα emission with hydrogen flow of 4% in preheated air discharge. The shape of the line is obtained by subtracting the measured spectrum without hydrogen from the spectrum with hydrogen. FWHM of the line is determined with a Lorentzian fit.

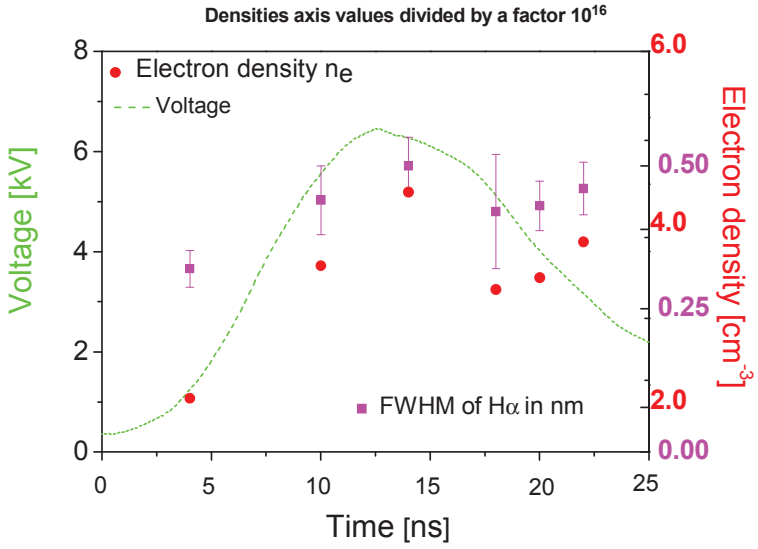

Figure 4.7 Temporal evolution (5-ns resolution) of the electron density (in red) of filamentary discharges in air, obtained from the FWHM of H_α (the points in pink). The dashed curve (in green) shows the evolution of the voltage of the discharge.

4.3 Optical Emission Spectroscopy (OES) study

4.3.1 Identification of the emitting species of NRP discharges

To identify the species present in the plasma discharge, we used the OES system described in Chapter 3 with a grating of 1200 grooves per mm.

The discharge studied was in the reference case. Figures (4.8, 4.9, 4.10, and 4.11) present the spectra obtained from 220 to 820 nm. The spectra are not calibrated (except those in figure 4.10) and are integrated over 10 ns during the maximum of discharge emission. For the wavelength between 400 and 800 nm, the use of high-bandpass filter at 400 nm is necessary to eliminate the second diffraction order of the spectrometer.

In the first domain between 200 and 290 nm, the emission of the electronic

system NO gamma ($A^2\Sigma^+_u$-$X^2\Pi_r$) is the major one as shown in figure 4.8. Between 290 and 490 nm, the second positive emission system of N_2 appears (see figure 4.9). We have identified also the first negative system of N_2^+, with a bandhead at 391 nm. Bands of the first positive system of nitrogen, N_2 (B-A), are visible from 480 to 760 nm (see figure 4.10) together with atomic nitrogen lines. At longer wavelengths, the characteristic triplet of atomic oxygen appears centered at 777 nm (see figure 4.11).

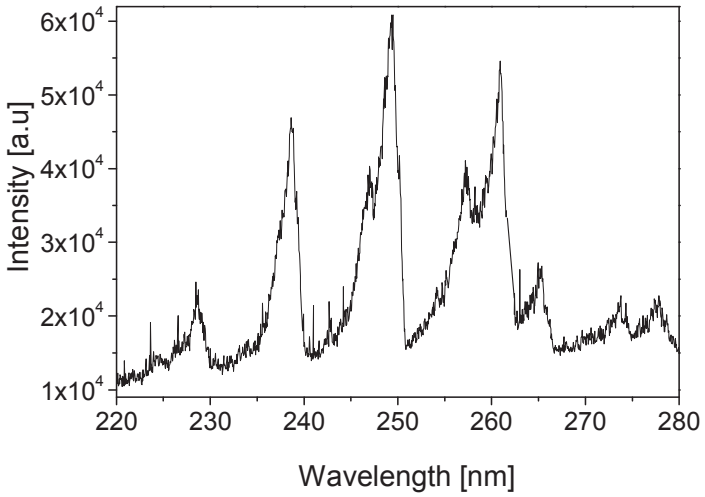

Figure 4.8 Emission spectrum of the discharge between 220 and 280 nm showing NOγ bands.

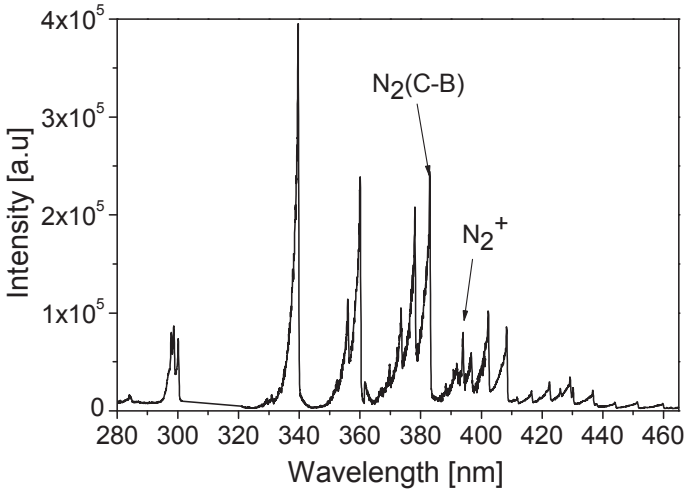

Figure 4.9 Emission spectrum of the discharge between 320 and 460 nm showing the emission bands of N_2(C-B) and N_2^+ (B-X)

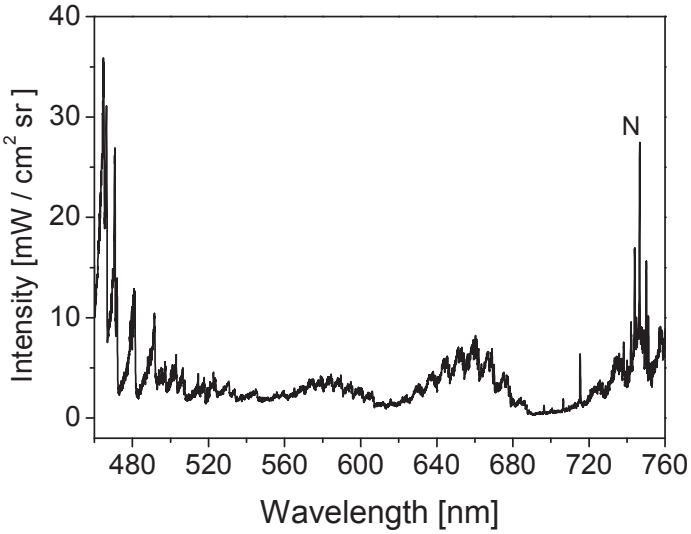

Figure 4.10 Emission spectrum of the discharge between 560 and 760 nm showing the emission bands of N_2 (B-A).

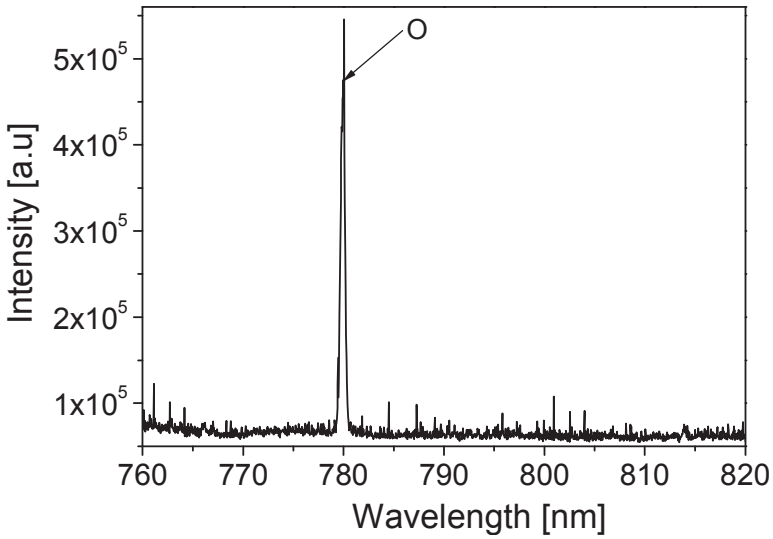

Figure 4.11 Emission spectrum of the discharge between 760 and 820 nm showing the emission of atomic oxygen.

4.3.2 Vibrational, rotational and translational temperatures

As discussed in chapter 2, the emission spectra of molecular band contain information on the electronic, vibrational and rotational population distributions.

To obtain the total density of a certain molecular species we need to know the population distribution over all the energy states of the species. If the population distributions over the vibrational and rotational levels follow Boltzmann distributions, we can define a vibrational temperature $T_{vib,}$ and a rotational T_{rot}, of the molecule of interest in the considered electronic excited state.

To determine the evolution of T_{vib} and T_{rot} in the reference case, the second positive system of nitrogen was used. This system represents the electronic transition of the molecule of N_2 from the $C^3\Pi_u$ electronic state to the $B^3\Pi_g$ electronic state, noted N_2(C-B).

i) Determination of the vibrational temperature

To obtain the population density in a given electronic level, the population distribution over the rotational and vibrational levels has to be known. Boltzmann distributions over these levels have to be proven and vibrational, rotational and translational temperatures have to be determined.

Fig 4.12 shows the vibrational bands simulated with SPECAIR (Laux *et al*, 2003). In this graph the best fit is obtained for the rotational temperature equal to 1500 K and for the vibrational temperature equal to 3400 K. We notice that different vibrational bands have different intensities. T_{vib} influences the relative intensities of the vibrational bands.

The measurements presented in figure 4.12 are made by optical emission spectroscopy in the discharge reference case, i.e. filamentary regime with applied voltage 6.6 kV and the distance inter-electrodes of 4 mm.

The spectra of N_2(C-B) vibrational bands are recorded using the OES system described in chapter 3. Figure 4.12 shows the fit of the experimental spectrum of the (0,3), (4,8) and (3,7) vibrational bands of N_2(C-B) with spectra obtained with SPECAIR simulations.

Careful attention was paid to the conditions of acquisition measurement parameters in order to maximize the signal-to-noise ratio. We can see in figure 4.13 that considerable error could be introduced depending on the accuracy of the acquisition. In this figure, we can see for instance that for T_{vib} = 3400 K determined from the (0-3) band an error of about 17% is introduced in the ratio of intensity when fitting other bands like the (0-2) and (1-3) bands. This occurs when the acquisition of the spectra is taken with fewer accumulations.

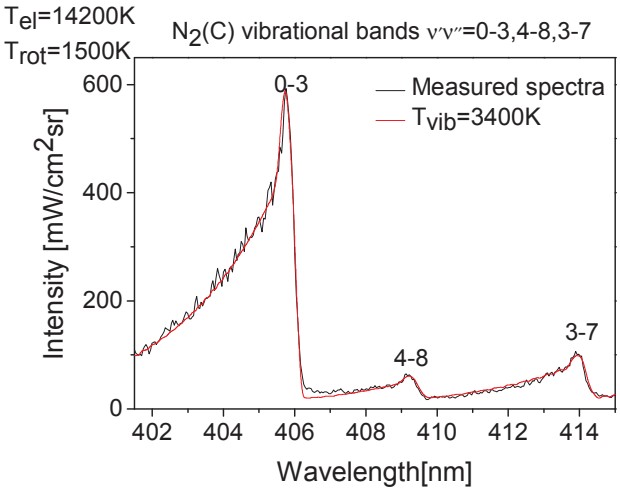

Figure 4.12 Typical N_2 (C-B) bands. The vibrational temperature is determined from the relative intensities of the following vibrational bands: (0-3), (4-8), (3-7)

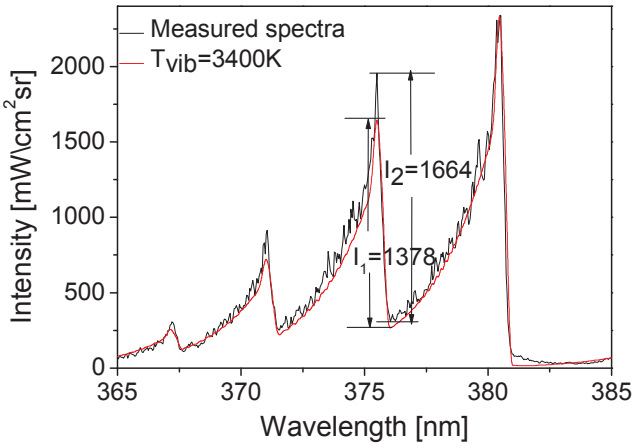

Figure 4.13 Typical N_2 (C-B) bands in filamentary regime of preheated air at 1000 K with PRF=10 kHz and inter-electrode distance of 4 mm, fitted with SPECAIR.

Nevertheless, we notice good spectral fitting with the same vibrational temperature, T_{vib}= 3400 K for different Δν (Δν=2, 3, 4). This confirms the assumption of a Boltzmann distribution of the populations over the vibrational levels for a given excited electronic state (here N_2(C)).

ii) Determination of the rotational and translational temperatures

The excitation of N_2 to electronic excited states occurs via collisions by electron impact. The free electrons in the discharge acquire a high kinetic energy in the electrical field which allows a fast (nanoseconds time scale) and significant excitation of fundamental molecular nitrogen. We considered here that the population distribution of of the rotational levels of $N_2(C)$ reflects the rotational distribution of $N_2(X)$. Because the mole fraction of N_2 in the gas is 0.8 and because rotational-translational relaxation is a very fast process at atmospheric pressure (less than ns), we can assume that T_{rot} = T_{rot} $N_2(X)$ = T_{gas} (Capitelli *et al*, 2000). The comparison with the numerical simulations of $N_2(C\text{-}B)$ spectra provided by SPECAIR will allow the determination of the translational (gas) temperature, if we measure the rotational temperature of the excited states.

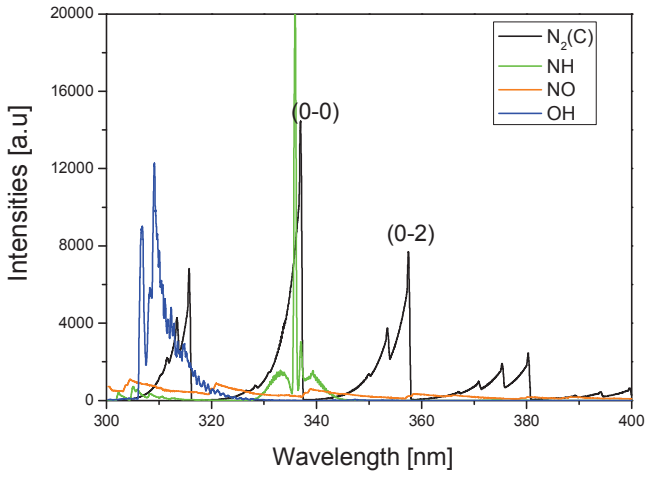

Figure 4.14 SPECAIR simulations of the species emitting in the range 300 -400 nm

For the T_{rot} measurements based on the $N_2(C\text{-}B)$ transitions, special attention was given to the spectral choice. The $N_2(C\text{-}B)$ emission band (0-2) shows the smallest overlap with the other emission species present in the discharge. In figure 4.14 spectra of the species present in the plasma such OH, NO, NH are simulated together with the second positive system.

In figure 4.15, the (0-2) $N_2(C\text{-}B)$ band shows a good fit with SPECAIR simulations for the rotational temperature of 1500 K with an estimated fitting error of ±

200 K. This temperature was assumed to be the gas temperature in the plasma channel before the heat release due to the discharge pulse, and is the result of heating by all previous pulses. The temperature was obtained from fitting the emission just at the beginning of the discharge pulse.

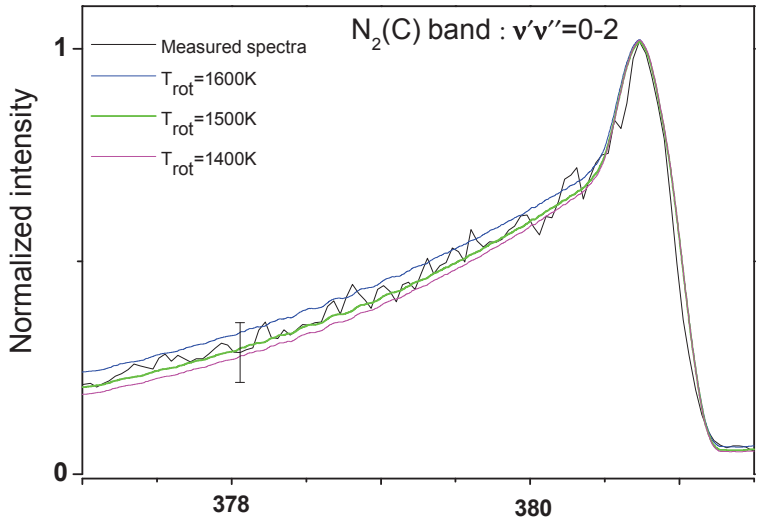

Figure 4.15 Normalized measured (0-2) band of N_2(C-B) in the reference case. The error on the fit of the rotational temperature is found to be ± 200 K

4.3.3 Determination of T_{rot} and T_{vib} time evolutions

To obtain a better understanding of the filamentary regime the evolution of vibrational and rotational temperatures, we performed optical emission spectroscopic measurements with a time gate width of 2-ns.

An important aspect of the discharge setup is the shape and the size of the electrodes, which have a strong influence on the applied electric field. Consequently the electron density and the heat released change in the discharge. A careful re-shape of the electrodes has been performed in order to keep constant these experimental parameters.

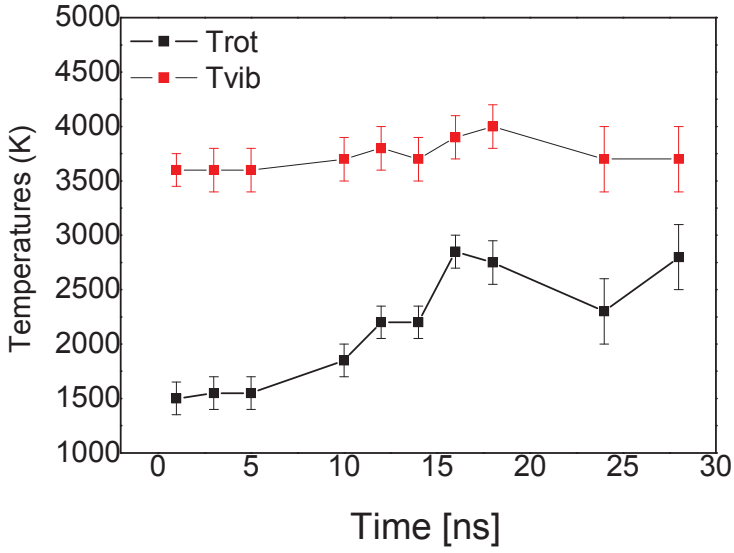

Figure 4.16 Temporal evolutions of T_{rot} and T_{vib} during 30 ns after the half of the maximum rise time of the tension

Figure 4.16 shows the temporal evolution of T_{rot} and T_{vib} during 30 ns . We notice a fast increase of the rotational temperature from 1500 (100) K to 2500 (400) K in about 30 ns. The fast heat released by the two-step mechanism could explain this fast increase of the temperature. In contrast, the vibrational temperature over 30 ns shows a nearly constant behavior. This aspect is explained by the slow (order of microseconds) vibrational-translational energy relaxation process (Capitelli *et al*. 2000).

4.3.4 Gas temperature increase as a function of the discharge repetition frequency

The influence of the pulse repetition frequency on the gas heating by the discharge was also studied. Optical emission spectroscopic measurements were realized at frequencies varied from 1 to 30 kHz, for the applied voltage 6.6 kV in the filamentary regime. Comparisons with spectra simulated using SPECAIR were realized on the vibrational bands (0,2) to obtain the rotational temperature. Best spectral fits of the evolution of the rotational temperatures as a function of the discharge pulse frequency are represented in figure 4.17. One set of measurements is taken at the first measurable discharge emission, while the second set represents the measurements taken at the time

corresponding to the emission of the maximum rotational temperature, which appears around 2-ns after the maximum plasma emission. We notice an increase of the rotational temperature with the increase of the pulse repetition frequency for both gate windows (i.e. before discharge and at 2-ns after the maximum emission).

To determine the relation between the frequency and the elevation of the temperature we need to look at the energy deposited by pulse. The average energy deposited per pulse increases linearly with the frequency. Thus, the increase of gas heating shown in figure 4.17 can be explained by the increase of the energy deposited by pulse.

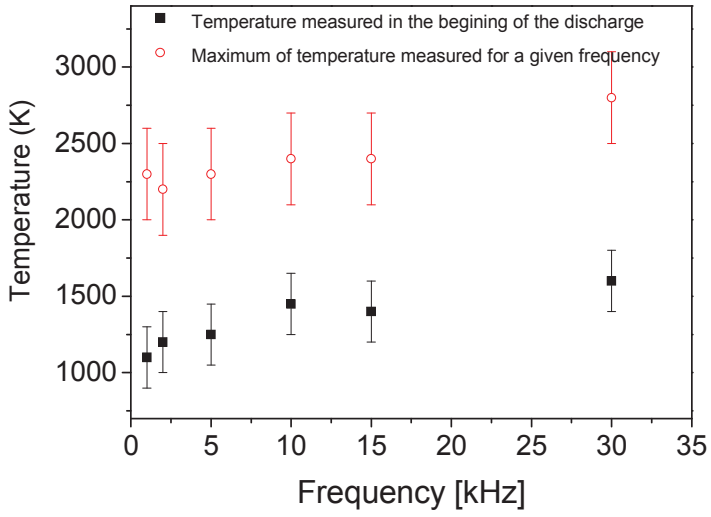

Figure 4.17. Gas temperature increase as a function of the discharge pulse frequency.

4.3.5 Time evolution $N_2(B)$ and $N_2(C)$ densities in air and nitrogen plasmas

The second positive emission system of nitrogen N_2(C-B) and the first positive emission system of nitrogen N_2 (B-A) allow us to determine from the spectra the density of the corresponding emitting electronic states. They also permit, based on the knowledge of quenching rate constants, to find the density of atomic oxygen produced by the quenching of these particular nitrogen excited states together with the

contribution of this quenching to the heat release and subsequent gas temperature increase.

Typical intensity-calibrated N_2 (B-A) spectra and N_2 (C-B) are represented in figures 4.18 and 4.19.

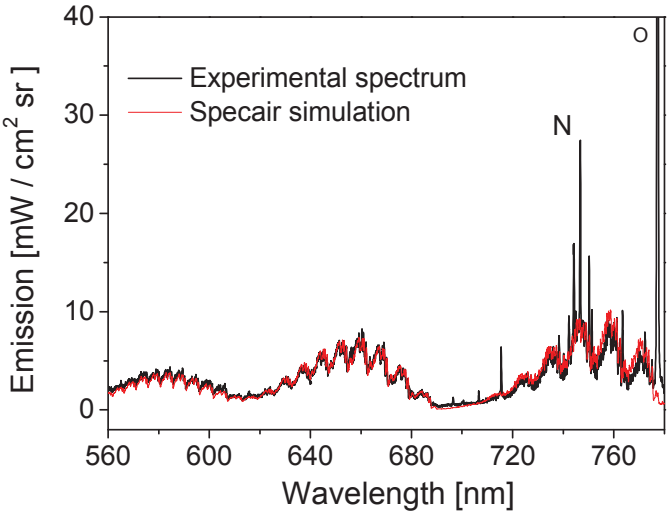

Figure 4.18 Typical calibrated N_2 (B-A) spectra. The best fit gives a density of N_2(B) equal to 3.7 x 10^{16} cm^{-3} for a 10-ns temporal window and with 30 % uncertainty

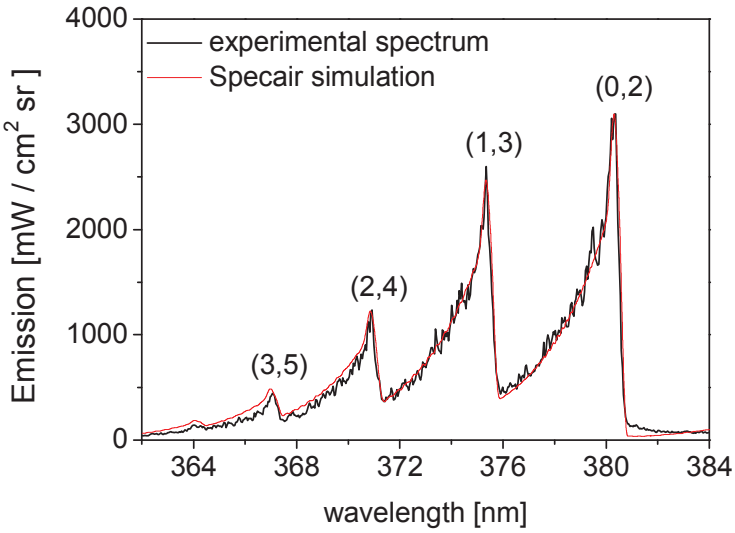

Figure 4.19 Typical calibrated N_2 (C-B) spectra. The best fit gives a density of $N_2(C)$ equal to 5 x 10^{15} cm^{-3} for a 10-ns temporal window and with 30 % uncertainty

The temporal evolution of the emission of N_2(C-B) was determined by measuring the emission of the vibrational band (0-2) at 380 nm. The spectral resolution of the spectrometer for these experiments was 0.4 nm. The typical acquisition time was changed between 2 ns (during the discharge) to 30 ns (in the post discharge). The time origin is taken from the first measurable spectra. Most acquisitions are averaged over 30000 pulses and calibrated in intensity using a tungsten lamp.

The spectra obtained show a maximum of intensity at t=8 ns. Knowing that N_2(C-B) emission is proportional to the density o N_2(C), we can say that the density of N_2(C) increases fast during the pulse. The excitation of the nitrogen electronic states is mainly due to fast electron impact excitation from the ground state. We notice, during the pulse duration when the electrical field is maximal, a fast and high increase of N_2(C) density followed by a quick density decrease. This decrease of the density could be explained by two processes: radiative de-excitation and quenching de-excitation with different molecules, mainly nitrogen and oxygen.

The measured temporal evolution of the densities of N_2(B) and N_2(C) in air and nitrogen, under filamentary discharge conditions, are represented in figures 4.20 and 4.21. In figure 4.21 the densities are normalized to the maximum values of 5×10^{16} cm^{-3}

and 6.1×10^{15} cm^{-3} for $N_2(B)$ and $N_2(C)$, respectively. For the nitrogen discharge, only relative densities are measured. The applied voltage pulse has a pulse width of 10 ns, a rise-time of 3 ns, and a decay time of 4 ns.

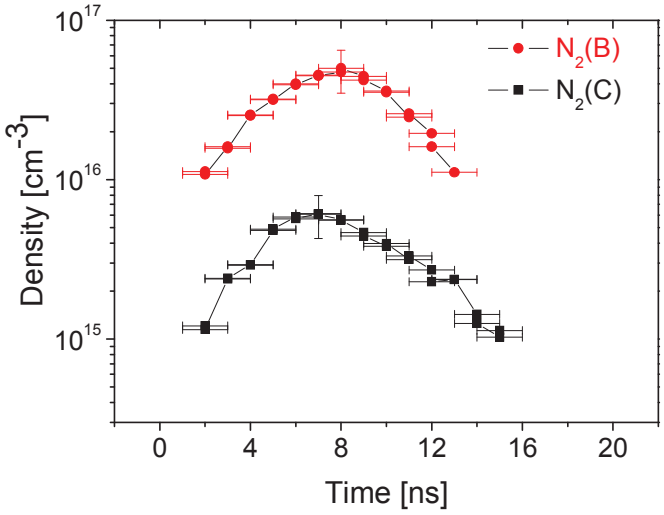

Figure 4.20 Temporal evolution (2-ns resolution) of the density of $N_2(B)$ and $N_2(C)$ in filamentary discharges in air

A decay time on the order of 2-5 ns was measured for $N_2(B)$ and $N_2(C)$. This very fast decay can be explained only by the fast quenching of $N_2(B)$ and $N_2(C)$ by the plasma species. The radiative processes are much slower than the quenching processes, the radiative lifetime being 40 ns for $N_2(C)$ and 6 μs for $N_2(B)$.

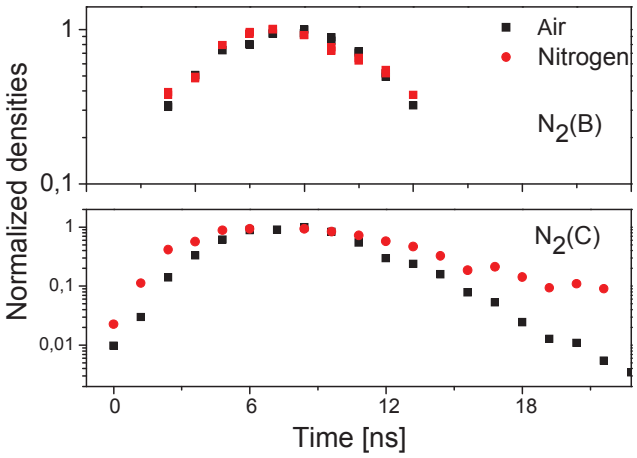

Figure 4.21 Normalized temporal evolution (2-ns resolution) of the density of N_2(B) and N_2(C) in filamentary discharges in air and in nitrogen

In figure 4.22 the spatially resolved emission intensity of N_2(C) produced by the NRP discharge is given. The spatial profiles in the diffuse and the filamentary regime at the maximum of discharge emission are shown. The plasma diameter is found to be about 0.5 mm for the diffuse regime and 0.35 mm for the filamentary regime. The size of the plasma is a very important parameter for the energy density calculations for instance.

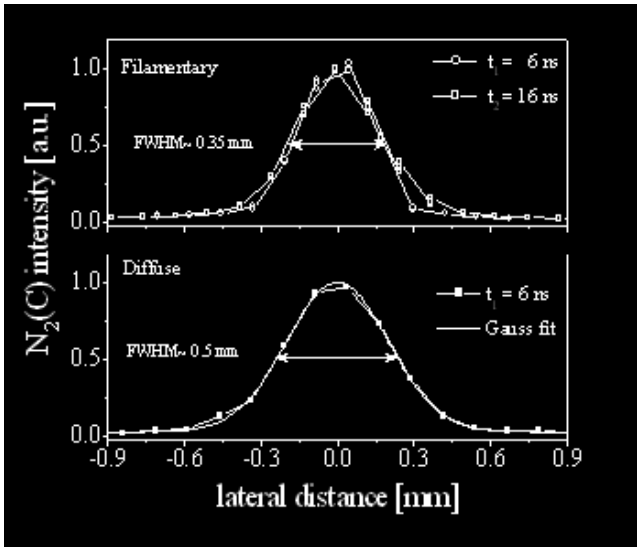

Figure 4.22 Spatial distribution of $N_2(C)$ density in filamentary and diffuse air discharges

4.4 Time evolution of $N_2(A)$ density measured by CRDS

In order to measure the density of the $N_2(A)$ metastable state by CRDS, precise synchronization of the discharge and laser events has been performed. The discharge occurs every 100 μs for a duration of 10 ns. The $N_2(A)$ density needs to be measured during the discharge and in the post discharge. The lifetime of $N_2(A)$ is too short to have an accumulation of metastable from pulse to pulse. The expected life time of $N_2(A)$ is of the order of 1 μs in nitrogen and less than 100 ns in air.

A typical CRDS signal is shown in figure 4.23. In the first part of the decay, which corresponds to times before the discharge pulse, there is no detectable absorption of $N_2(A)$. The decay intensity shows no information of the $N_2(A)$ density, the slope of the signal during this period defines the empty cavity decay time. In the second region, the presence of the discharge event is marked by a large spike due to the discharge electromagnetic noise (EM). The decay time in this part cannot be measured. In the third region after the pulse, we notice that the decay intensity is faster with the discharge (figure 4.23 b) due to the presence of $N_2(A)$ species, which are formed by electron-impact excitation during the discharge pulse. We notice another short period with EM

noise (a second spike) corresponding to a secondary voltage pulse (a feature inherent to our specific pulser). However, this second spike does not disturb significantly our measurements. These three regions can be seen distinctly in the typical cavity ring down decays of nitrogen and air filamentary plasmas, as presented in figures 4.23 and 4.24 respectively.

The (a) curves show the variation of the intensity recorded by the PMT when the 770.055-nm radiation passes through the cavity, which corresponds to an off-resonance wavelength of the N_2 (B-A) transition. The (b) curves are obtained on an absorption resonance at 769.945 nm (Kaddouri *et al*, 2009).

In figure 4.24, we can see that the difference from (a) and (b) curves is much smaller than in figure 4.23. We notice also that the difference between (a) and (b) seems to be constant about 100 ns after the discharge pulse.

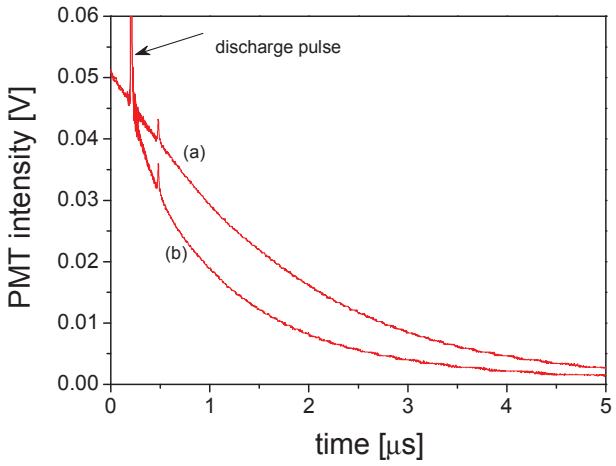

Figure 4.23 Typical measured intensity decays for nitrogen plasma. Curves (a) and (b) are recorded at 770.012 (off-resonance) and 769.945 nm (on resonance), respectively.

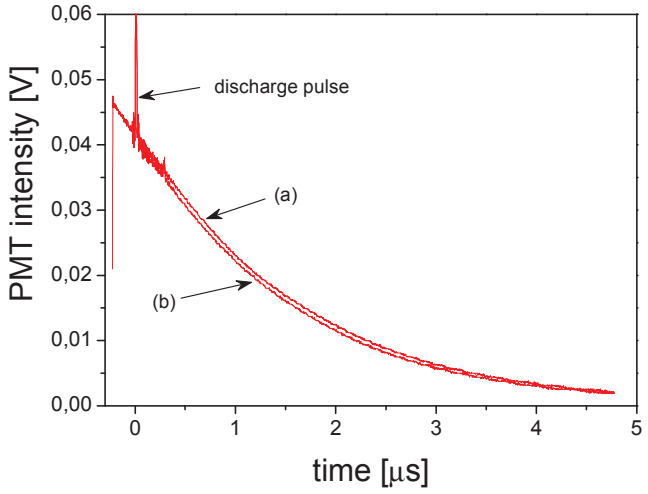

Figure 4.24 Typical measured intensity decays for air plasma. Curves (a) and (b) are recorded at 770.012 and 769.945 nm, respectively.

Figure 4.25 shows the results of figure 4.23 plotted in a semi-log scale. We notice a difference between the measured off-resonance signal and the extrapolated signal measured before the discharge event. This difference is explained by the beam-steering and scattering losses inside the cavity. Beam-steering is caused by the large temperature difference between ambient air and the plasma whose temperature is higher than 1000 K. This causes changes in the refractive index of air. As a result the laser beam tends "to walk away" from the cavity and therefore a faster decay is measured. We verified that these effects have negligible wavelength dependence for the spectral region scanned (Janda and al, 2009).

We notice also that the on resonance curve is not linear in the semi-log plot. This is an evidence that the density of $N_2(A)$ changes during the decay time (see chapter 2). When the laser wavelength is set to 769.944 nm (strongest absorption), the resulting signal is no longer linear. The slope of this signal decreases in time. In the semi-log scale several slopes can be observed, which means that the absorption is not constant in time. The $N_2(A)$ and the absorption decreases due to the decreasing density of $N_2(A)$..

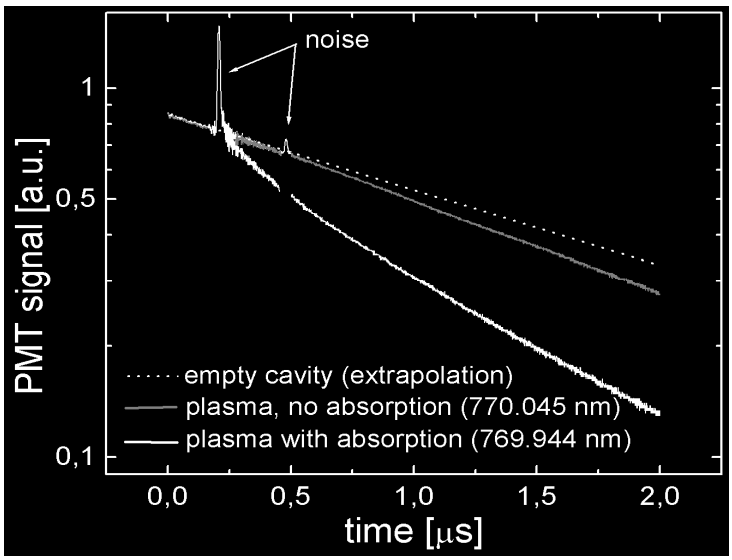

Figure 4.25 Curves from figure 4.23 plotted in semi-log scale.

Figure 4.26 presents the decay time in semi-logarithmic scale for the air discharge. When the laser is tuned to 770.055 nm (an off-resonance wavelength with no absorption) the signal in the logarithmic scale remains linear. We see that there is a fast change in the decay rate during less than 100 ns, and afterwards the decay rates are equal. This means that, in the air plasma, $N_2(A)$ is quenched faster than in the nitrogen plasma. Thus the presence of O_2 leads to faster quenching.

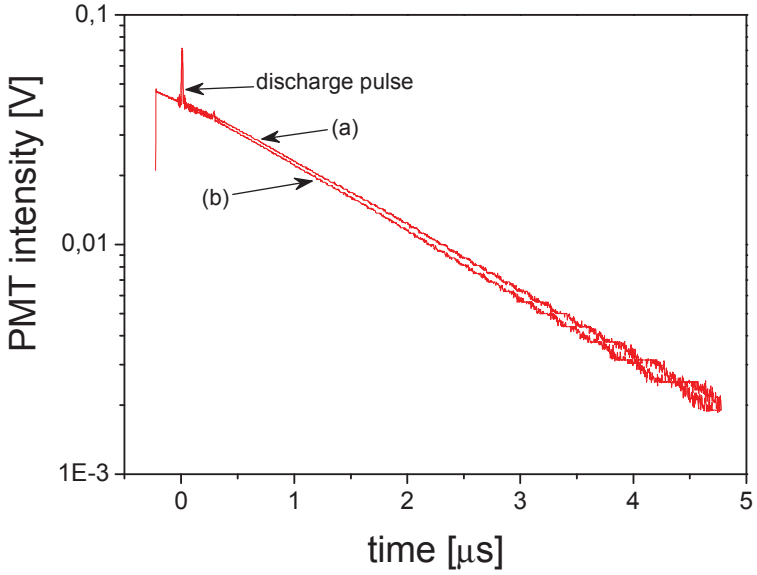

Figure 4.26 The curves from figure 4.24 plotted in semi-log scale.

The average $N_2(A)$ density for the air plasma in the reference case can be calculated using the following formula (Stancu *et al*, 2010 a):

$$N_{average} = \frac{1}{S(T)\phi(\nu)} \frac{L}{cl_{abs}} \frac{\ln(I_1/I_3)_{t=100ns}}{dt} \qquad \textbf{eq.3}$$

The $N_2(A)$ average density over 100 ns was found to be $5x10^{14}$ cm^{-3}.

Because the decay signal in the air plasma was too weak, we could not make parametric studies for the air plasma. Instead, we tried to characterize the nitrogen plasma. We have measured first the variation of $N_2(A)$ concentration with the applied voltage. Figure 4.27 shows the results averaged over one microsecond immediately after the discharge pulse. A linear behavior as a function of the applied voltage was obtained. Increasing the applied voltage leads to an increase of the electron density and thus of the $N_2(A)$ production. The $N_2(A)$ density increases linearly when the voltage increases from 6.2 to 7.7 kV. Over this voltage range, the plasma produced by the discharge varies from a diffuse regime to a filamentary regime.

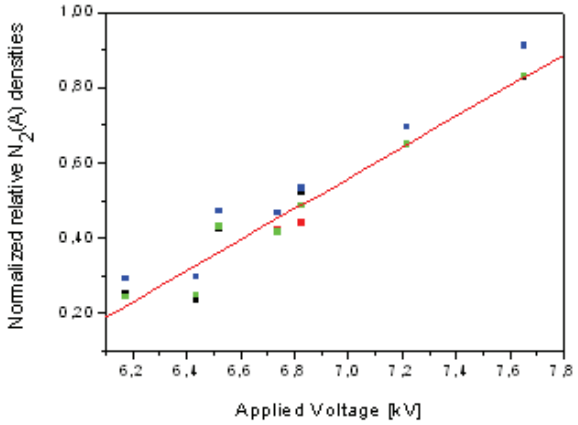

Figure 4.27 $N_2(A)$ density as a function of the applied voltage.

The evolution of the $N_2(A)$ concentration in nitrogen is shown in figure 4.28 (see chapter 2 for data processing procedure). We can see that the $N_2(A)$ peak density was measured to be of $2.5x10^{15}$ cm^{-3} . The $N_2(A)$ lifetime was found to be 600 ns (Stancu *et al*. 2010 a).

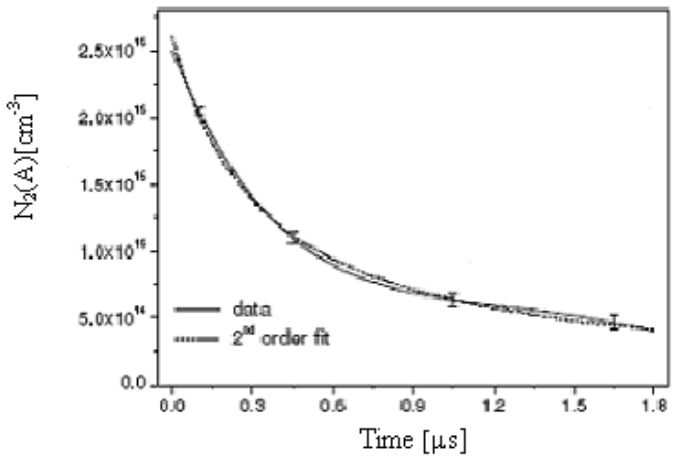

Figure 4.28 Time evolution of the $N_2(A)$ density in nitrogen plasma.

As shown in figure 4.29, the $N_2(A)$ spatial distribution has a nearly Gaussian profile, of Full Width at Half Maximum equal to 0.6 mm. A radial profile of the absorption coefficient was obtained after Abel inversion (see chapter 2). The inset

shows the lateral absorbance fitted with a Gaussian function. The $N_2(A)$ species in the nitrogen plasma presents a slightly larger distribution than $N_2(C)$, which could be due to larger instrumental broadening (laser spatial width) and diffusion processes.

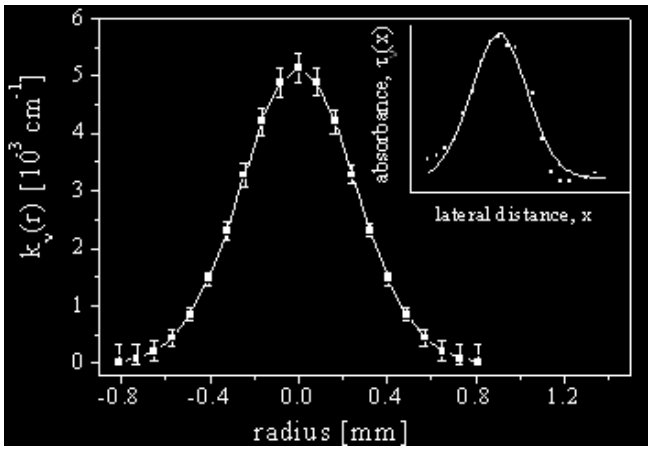

Figure 4.29 The radial profile of absorption coefficient obtained after Abel inversion

4.5. Time evolution of O ground state measured by TALIF

TALIF measurements have been performed to characterize the formation of atomic oxygen by the discharge pulse. As mentioned earlier, atomic oxygen is one of the key species in combustion processes. Understanding its formation is important for the mechanism of flame ignition and stabilization by NRP discharges.

As described in chapter 2, the density of the ground state atomic oxygen depends on the fluorescence signal and the square of the laser intensity, as given by the formula:

$$N_1 = \frac{\iiint_{t,\lambda L,\lambda F} S_{TALIF}\, dt\ d\lambda_L\, d\lambda_F}{D\,\frac{A_{23}}{A+Q+\Gamma}\, h\nu_F\, G^{(2)}\hat{\sigma}^{(2)}\,\frac{\int_t I_0(t)^2\, dt}{(h\nu_L)^2}} \qquad \textbf{eq. 4}$$

where S_{TALIF} is the fluorescence signal integrated over time t, λ_F is the fluorescence wavelength (lines centered at 844.6 nm for O), and λ_L is the laser wavelength (225.6 nm for O). D characterizes the LIF detection system, $G^{(2)}$ is the photon statistics factor,. $\hat{\sigma}^{(2)}$ is the integrated two-photon absorption cross-section, $I_0(t)$ is the laser intensity and $h\nu$ is the photon energy. $A_{23}/A+Q+\Gamma$ is the fluorescence quantum yield;

As a first step, we measured the atomic oxygen fluorescence signal at 844 nm by scanning over the laser line at 225 nm. The exciting laser intensity and the fluorescence signal were recorded by the ultrafast PD and the spectrometer, respectively. Figure 4.30 shows a typical oxygen TALIF signal. The output laser intensity, which slightly varied in time, was monitored by the fast photodiode for normalization purposes. The measured O fluorescence signal as a function of the squared intensity, $I^2(t)$, time integrated, is represented in figure 4.31. All TALIF measurements were performed for the range of intensities in which a non-saturated regime is observed. In order to obtain fluorescence signals independent of the laser intensity, all measurements were normalized to $\int I^2(t)dt$. The fluorescence signals were therefore directly proportional with the density of O in the ground state, noted N_1.

As explained in chapter 3, Xenon was used here as the calibration gas, to convert experimental data into absolute densities. Because Xe has very similar wavelengths for two-photon absorption and fluorescence, the sensitivity of the detection system is closely similar for O and Xe. Using the literature values of the spectroscopic properties, the branching ratios and cross-sections of Xe and O (Bamford *et al*, 1986 and Niemi, 2005), the absolute O density can be determined using the equations from chapter 3.

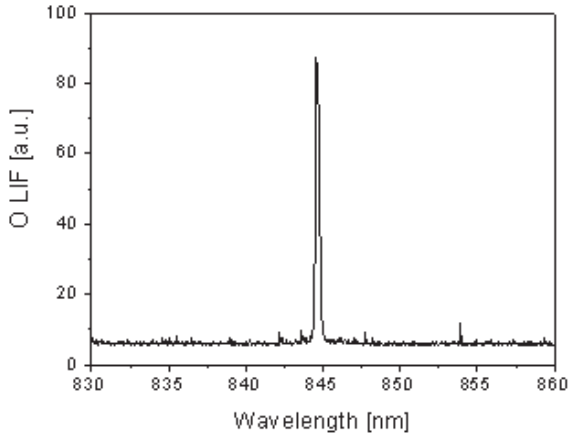

Figure 4.30 Typical O fluorescence at 845 nm

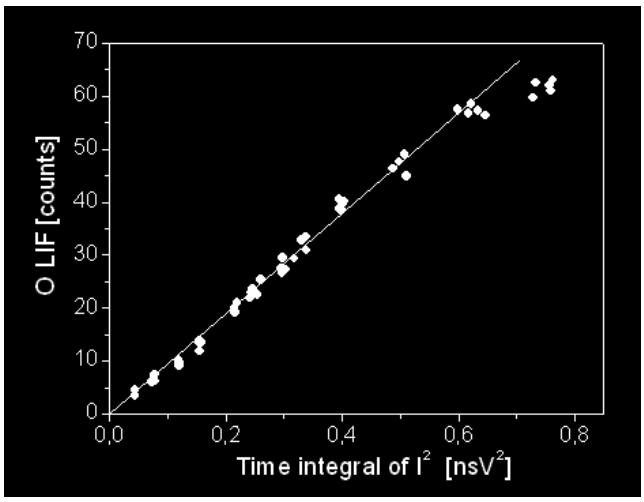

Figure 4.31 O fluorescence signal as a function of the squared laser power

Figure 4.32 shows a typical Xe fluorescence signal (Stancu *et al*. 2008). The variation of the fluorescence signal **as a** function of the squared laser power is shown in figure 4.33. The linear dependency shows that the experiment is carried out in non-saturation conditions.

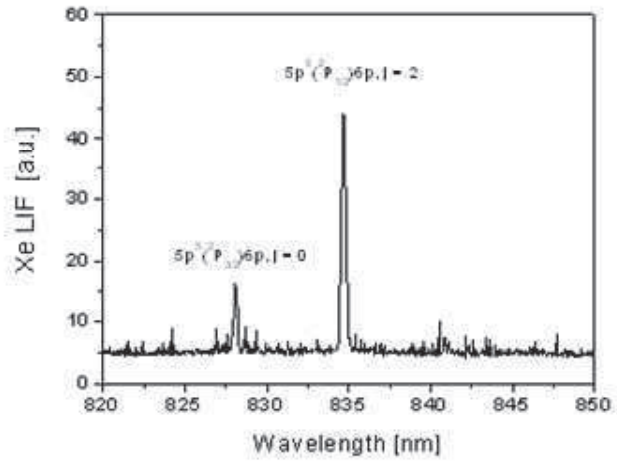

Figure 4.32 Sample of Xe fluorescence at 835 nm

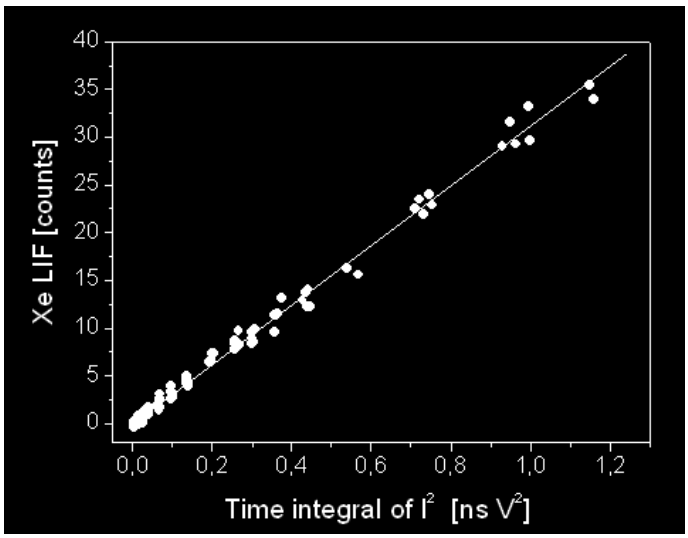

Figure 4.33 Xe fluorescence as a function of the squared laser power

Figure 4.34 shows the normalized atomic oxygen fluorescence signal as a function of the laser excitation wavelength. This result shows a Gaussian profile centered at wavelength $\lambda = 225.597$ nm, which is the resonant two-photon transition.

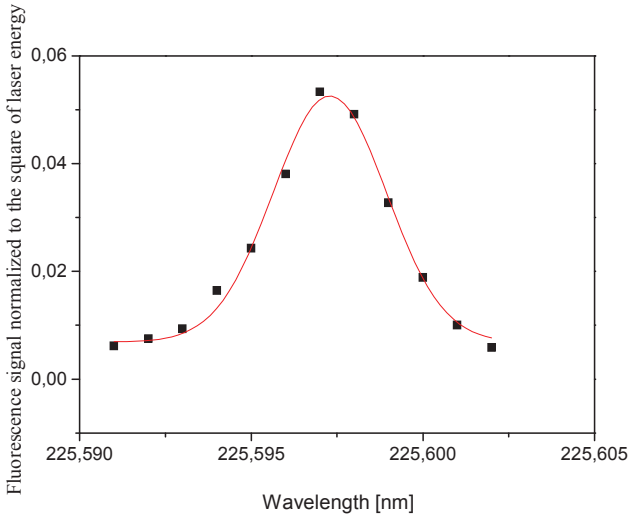

Figure 4.34 Oxygen fluorescence signal normalized to the squared laser pulse energy as a function of the excitation wavelength

As a second step, we studied the spatial distribution of atomic oxygen in the

plasma. We recorded measurements of normalized fluorescence signal measured laterally in the air plasma. Results are presented in Figure 4.35.

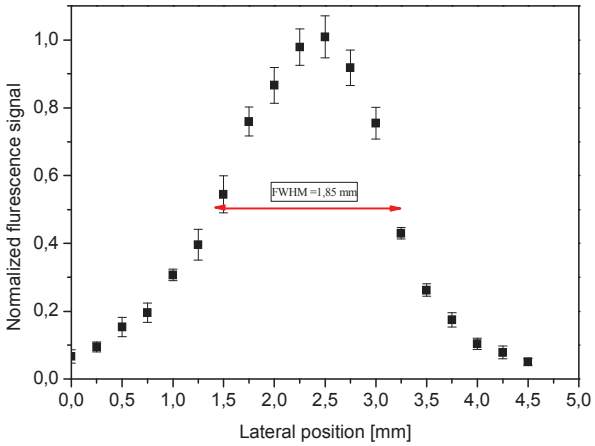

Figure 4.35 Lateral scan measurements of the oxygen fluorescence in the plasma

The lateral evolution of the fluorescence signal has a nearly Gaussian profile of FWHM = 1.85 mm (Kaddouri *et al*. 2009). This is wider than the plasma width measured by OES (N_2(C) distribution) and CRDS (N_2(A) distribution). As we will see later, because O has a long lifetime (25 µs), it decays slowly and thus accumulates and diffuses during one period (100 µs).

Figure 4.36 shows the temporal evolution of the normalized fluorescence during one plasma cycle.

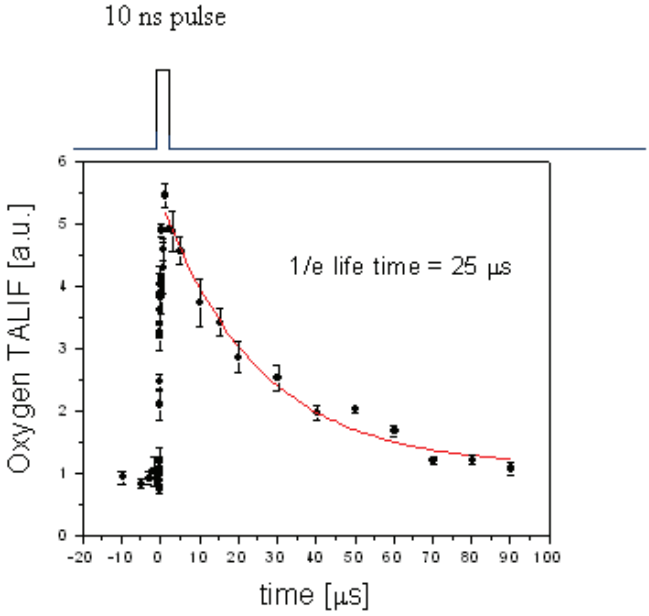

Figure 4.36 Relative temporal evolution of the O fluorescence during one plasma cycle

A zoom in the first 300 ns after discharge event is shown in figure 4.37. The duration over which the discharge pulse occurs is shown by the emission of the excited atomic oxygen generated by direct electron-impact excitation during the discharge pulse. This was recorded at 844.6 nm with the same detection system as for fluorescence, except that the laser was turned off. The emission from the plasma was present for about 15 ns. The TALIF data show the following important results: 1) atomic oxygen is largely produced only about 20 ns after the discharge event, 2) the production of atomic oxygen continues during the first 100 ns and 3) the atomic oxygen density decreases until the next pulse. We measured an increase by a factor of 5.5 of oxygen fluorescence due to the discharge pulse, followed, after the end of the pulse, by a decay of oxygen due to recombination processes. According to figure 4.36, the oxygen lifetime is about 25 µs.

Using the procedure of calibration with Xe described in chapter 3, the O relative densities were then converted into absolute densities.

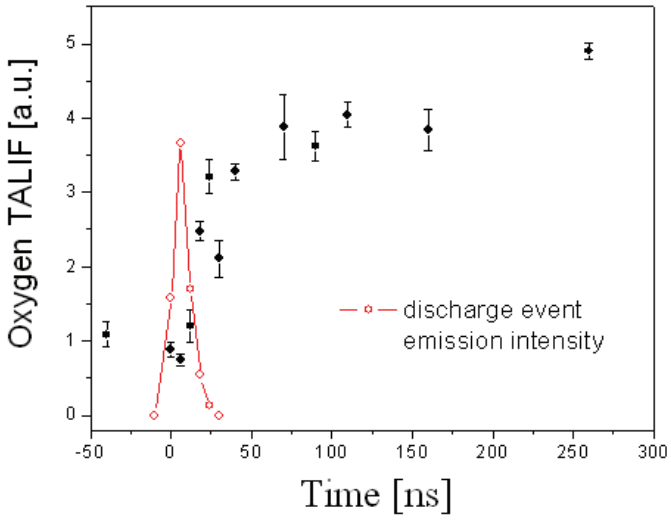

Figure 4.37 Temporal evolution of the O fluorescence normalized to the squared laser intensity, together with the emission of the atomic oxygen produced during the pulse.

4.6 Validation of the two-step mechanism for O production by NRP discharges in atmospheric pressure air

4.6.1 Comparison of the measured and calculated O density

Figure 4.38 (top graph) shows the measured temporal evolution of the densities of $N_2(B)$, $N_2(C)$, and $N_2(A)$ after the discharge pulse (Stancu *et al*. 2009). Figure 4.38 (bottom) shows the measured temporal evolution of the density of O during the first 100 ns following the discharge pulse, with a temporal resolution of 6 ns. Up to 50% of molecular oxygen is found to be dissociated by the filamentary NRP discharge in the reference case. In addition the increase of the O density is found to be synchronized with the decrease of the $N_2(B)$ and $N_2(C)$ densities. Finally, we note that the density of O before the pulse corresponds to about 10% of dissociation o O_2. This initial O density is the result of previous pulses.

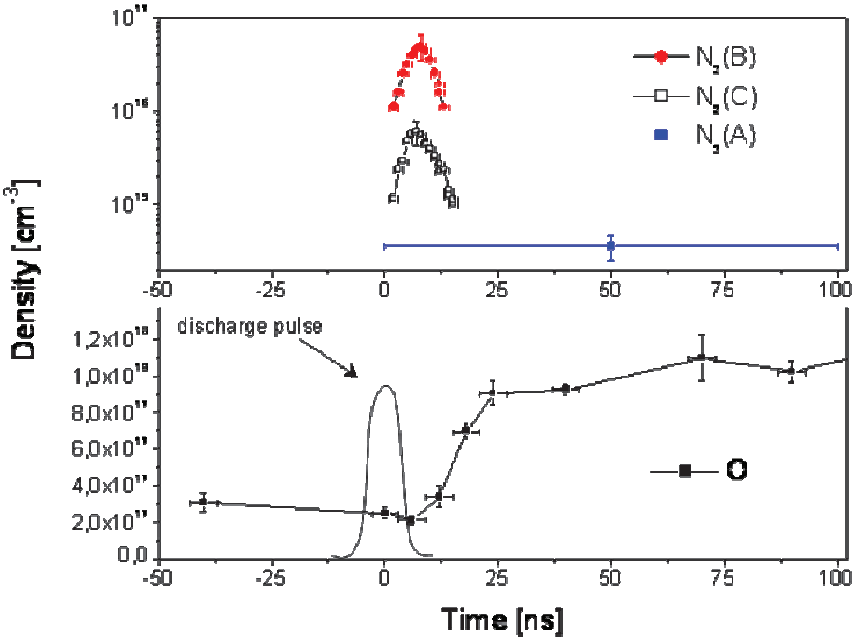

Figure 4.38 Temporal evolution of N_2(B), N_2(C), N_2(A) and O densities during first 100 ns after discharge pulse

Calculations have been made to compare the density of atomic oxygen measured by TALIF with the density of oxygen obtained considering the two-step mechanism as described by the set of reactions given in eq. 5. The results are shown in figure 4.39. These calculations were carried out using the densities of the measured nitrogen excited states N_2(A), N_2(B) and N_2(C), and the quenching rates published in the literature (Kossyi *et al*., 1992). The influence of N_2(A) is found to be minor due to the weak value of the density of this state and its slow quenching rate compared to those of N_2(B) and N_2(C).

$$N_2(A) + O_2 \rightarrow N_2(X) + 2O$$
$$N_2(B) + O_2 \rightarrow N_2(X) + 2O \qquad \textbf{eqs. 5}$$
$$N_2(C) + O_2 \rightarrow N_2(X) + 2O$$

The oxygen produced by the two-step mechanism was calculated using the following equations:

$$\frac{dn_O}{dt} = 2k_B n_{O_2} n_B + 2k_C n_{O_2} n_C$$
$$= 2\left(n^0{}_{O_2} - \frac{n_O}{2} \right)\left(k_B n_B + k_C n_C \right)$$
$$n_O{}^{i+1} - n_O{}^{i} = 2\left(k_B{}^{i} n_B{}^{i} + k_C{}^{i} n_C{}^{i} \right)\left(n^0{}_{O_2} - \frac{n_O{}^{i}}{2} \right).\Delta t \qquad \textbf{eq. 6}$$
$$n_O{}^{i+1} = n_O{}^{i}\left[1 - \left(k_B{}^{i} n_B{}^{i} + k_C{}^{i} n_C{}^{i} \right)\Delta t \right] + 2\left(k_B{}^{i} n_B{}^{i} + k_C{}^{i} n_C{}^{i} \right) n^0{}_{O_2}\,\Delta t$$

To summarize, we calculate the amount of atomic oxygen produced by integrating the following relation over time:

$$n_{O(t)} = 2\times\int_0^t \sum_{A,B,C} k_{A,B,C} \quad n_{N_2[A,B,C](t)} \quad n_{O_2} \quad dt$$

with $k_{A,B,C}$ taken from Kossyi *et al*, 1992. at 1500 K.

In figure 4.39 the O density calculated based on the measured temporal profiles of N_2(A,B,C) densities shows a very good agreement with the measured O density. Thus, the two-step mechanism for the formation of O atoms is validated by the measured temporal evolution of O and of the excited nitrogen species. The formation of O coincides with the loss of N_2(A,B,C), and mostly with the loss of N_2(B).

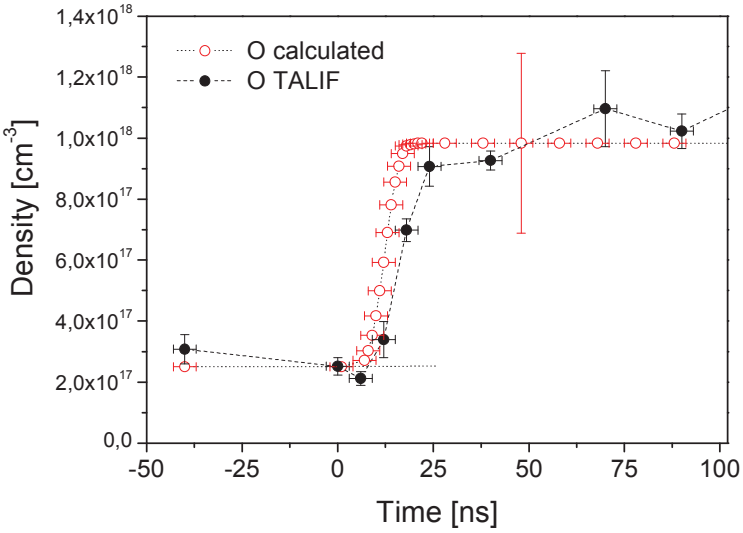

Figure 4.39 Comparison between the density of the atomic oxygen measured by TALIF and the one calculated following the two step mechanism

Measurements of O, $N_2(B)$ and $N_2(C)$ densities as a function of time have confirmed that the formation of atomic oxygen occurs through the fast two-step mechanism. The large amount of O produced by the filamentary NRP discharge may explain its key role in the mechanism of flame stabilization by plasmas.

4.6.2 Comparison of the measured and calculated gas temperature

In this section, we will show the comparison between the measured increase of gas temperature and the calculations, which are based on the two-step mechanism process. This assumes that the heat release is mainly due to the exothermic effect of the quenching reactions that also produce atomic oxygen:

$$N_2(X) + e \rightarrow N_2(A,B,C) + e \qquad \textbf{eq.7}$$

$$N_2(A,B,C) + O_2 \rightarrow N_2(X) + 2O + Heat \qquad \textbf{eq 8}$$

For the three electronic excited states of nitrogen N_2 (A,B,C), the energy released when one excited molecule interacts with molecular oxygen to produce atomic oxygen can be calculated. In the literature the quenching rates of these reactions are presented in Table 1:

Table 1 Dissociative quenching rate coefficients of nitrogen excited states.

k_{diss} N_2(A) [$cm^3.s^{-1}$]	k_{diss} N_2(B) [$cm^3.s^{-1}$]	k_{diss} N_2(C) [$cm^3.s^{-1}$]
$1.63x10^{-12}$ (Guerra)	$2x10^{-10}$ (Piper)	$3x10^{-10}$ (Pancheshnyi)
$2.54x10^{-12}$ (Kossyi)	$3x10^{-10}$(Kossyi)	$3x10^{-10}$(Kossyi)

We will see later in this section the importance of the choice of the reaction rates in the determination of the temperature increase and the error related to this choice.

We consider that the heat released by each of the three quenching channels of the A, B, and C nitrogen states is given by ΔE_A = 1 eV, ΔE_B = 2.2 eV, ΔE_C = 5.9 eV, respectively and that k_A, k_B and k_C are the corresponding dissociative rate coefficients.

Using the measured density evolutions and the quenching rates from the literature, we can determine the energy E released by the system as:

$$\frac{dE}{dt} = \frac{1}{2}\left[\left.\frac{dn_O}{dt}\right|_A \Delta E_A + \left.\frac{dn_O}{dt}\right|_B \Delta E_B + \left.\frac{dn_O}{dt}\right|_C \Delta E_C \right]$$

$$= \left[k_A n_A \Delta E_A + k_B n_B \Delta E_B + k_C n_C \Delta E_C\right] \cdot n_{O_2} \qquad \textbf{eq 9}$$

The temperature of the gas is directly related to the energy released by the system as shown in the following formula:

$$T(t_{i+1}) = T(t_i) + \frac{1}{\rho C_v}\left[k_A(t_i) n_A(t_i) \Delta E_A + k_B(t_i) n_B(t_i) \Delta E_B + k_C(t_i) n_B(t_i) \Delta E_C\right] \cdot \left(n_{O_2}^0 - \frac{n_O(t_i)}{2} \right) \Delta t$$

eq 10

where C_v is thermal heat capacity and ρ is the gas density.

Thus, knowing the nitrogen excited states n_A, n_B and n_C time evolutions we can calculate the time evolution of the gas temperature in the discharge.

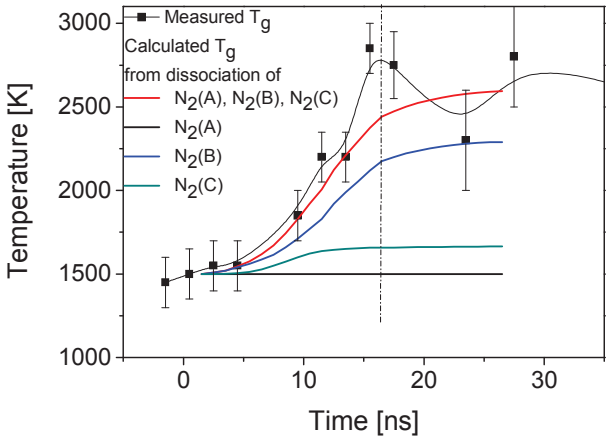

Figure 4.40 Calculated and measured gas temperature evolution in the air plasma discharge (standard case)

Figure 4.40 shows a comparison between the calculated gas temperature and the measured rotational temperature evolution in the plasma. From the calculations of the evolution of the gas temperature we observe a fast increase during the first 20ns, which is comparable to the one obtained experimentally by optical emission spectroscopy. The results are in good agreement within error bars. We can see also the major role of the $N_2(B)$ in the temperature increase, about 80 %. The black curve shows the $N_2(A)$ contribution, the green curve is $N_2(C)$ contribution, the blue curve is $N_2(B)$ and the red curve is the sum of all contributions.

If we use in the calculations the different sets of dissociative rate coefficients reported in the literature, we obtain a range of gas temperature increases. Figure 4.41 shows different gas temperature evolutions obtained using the quenching rates reported by Kossyi *et al*. 1992, Guerra *et al*, 1997; and Bak *et al*. 2011 (see Table 2) , for purposes of comparison with the measured rotational temperature evolution.

Table 2. Quenching rate coefficients from the literature

Reference	k_{diss} $N_2(A)$ [$cm^3.s^{-1}$]	k_{diss} $N_2(B)$ [$cm^3.s^{-1}$]	k_{diss} $N_2(C)$ [$cm^3.s^{-1}$]
Kossyi (1992)	$2.54x10^{-12}$	$3x10^{-10}$	$3x10^{-10}$
Guerra *et al*. (1997)	$1.63x10^{-12}$	$2x10^{-10}$	$3x10^{-10}$
Bak *et al*; (2011)	–	$4x10^{-11}$	$10x10^{-11}$

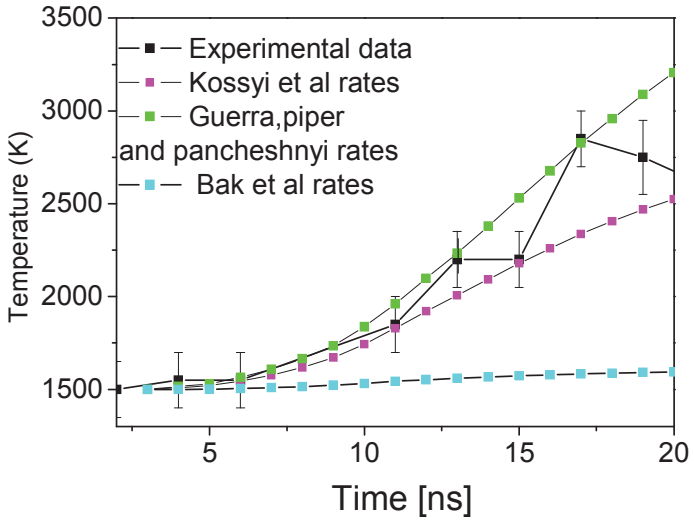

Figure 4.41 Gas temperatures evolutions obtained using various quenching rate coefficients referenced in the literature (Kossyi, 1992, Guerra, 1997, and Bak, 2011) compared to the measured temperatures

4.6.3 Comparison of the discharge and the two-step mechanism energies

The two-step mechanism has exothermic reactions where nitrogen excited states react with molecular oxygen producing atomic oxygen with heat release. An important aspect is to know the total energy available per pulse and the fraction used for the respective productions of oxygen and heat. The total energy coupled into plasma was

obtained from voltage and current measurements as described in section 4.11. Using the results of the density evolution of $N_2(A)$, $N_2(B)$ and $N_2(C)$ will allow to compare the measured energy with the energy released into O production and heating.

The energy released per reaction channel is calculated by the formula:

$$\frac{dE}{dt} = \frac{1}{2}\left[\left.\frac{dn_O}{dt}\right|_A \Delta E_A + \left.\frac{dn_O}{dt}\right|_B \Delta E_B + \left.\frac{dn_O}{dt}\right|_C \Delta E_C \right] = \left[k_A n_A \Delta E_A + k_B n_B \Delta E_B + k_C n_C \Delta E_C \right] n_O \qquad \textbf{eq 12}$$

The total energy, the energy consumption on heating and the energy used for the dissociation of O_2 are shown in figure 4.42. We can see that about 30 % of the energy is spent on the two-step mechanism: about 20 % for the dissociation of O_2 and about 10 % for gas heating.

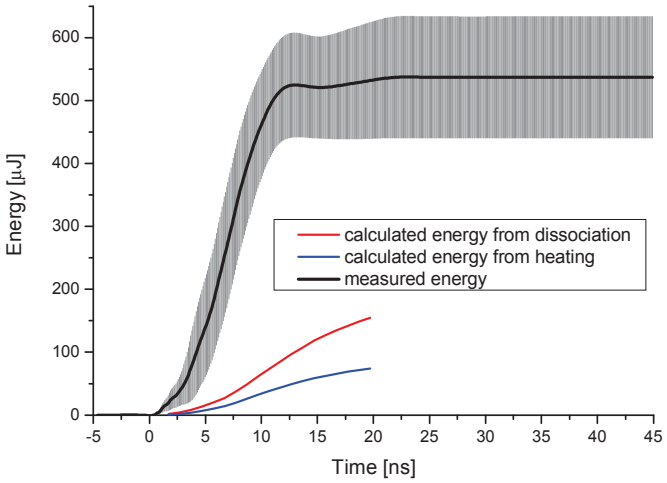

Figure 4.42 Comparison of the measured total energy with the calculated energy into dissociation of O_2 and into gas heating

Conclusions and Future Work

Many applications of atmospheric pressure plasmas are in development. For each application, it is important to use plasmas produced with high energy efficiency and to optimize the processes of production of the desired chemical species. For this, a fundamental understanding of the energy coupling and of the kinetic mechanisms involved in plasmas are necessary.

The study of plasma-assisted combustion is our principal application of interest. It has been shown that the use of plasmas tends to help stabilize lean flames, which are known to be less polluting. To satisfy the efficient energy coupling criterion, we chose to use in our work the Nanosecond Repetitively Pulsed discharge.

The discharge and the associated diagnostics, i.e. Optical Emission Spectroscopy (OES), Cavity Ring-Down Spectroscopy (CRDS), and Two-photon Absorption Laser-Induced Fluorescence (TALIF) experimental set-ups, their principles and their challenges were presented together with electrical measurements used for investigations of the NRP discharges in air at atmospheric pressure. Using these techniques we have measured the temporal evolution of the absolute densities of the key species N_2(A,B,C) and O, the temperatures and the energy coupled into air and nitrogen plasmas (in the NRP spark discharge regime) with nanosecond temporal resolution and sub-mm spatial resolution.

Based on previous studies, it was assumed that the discharge produced radicals that enhance the combustion process due to the formation of atomic oxygen in NRP discharges via a fast two-step mechanism:

$$N_2(X) + e \rightarrow N_2(A,B,C) + e$$

$$N_2(A,B,C) + O_2 \rightarrow N_2(X) + 2O + \text{heat}$$

The main result of our work was the experimental validation of the two-step mechanisms for O production. This has been proven by nanosecond time-resolved measurements of N_2 (A, B, C), and atomic oxygen densities together with temperature and energy measurements.

Optical emission spectroscopy allowed us to determine the densities of N_2(B) and N_2(C) nitrogen excited states. In air plasmas, the average density over 10 ns was found to be about $3.7(1.2)\text{x}10^{16}$ cm^{-3} and $5(1.6)\text{x}10^{15}$ cm^{-3}, respectively.

CRDS has proven to be an appropriate technique for $N_2(A)$ detection. Time-resolved and space-resolved CRDS have been performed. The density of $N_2(A)$, averaged over 100 ns, produced by the NRP discharge was found to be on the order of $4(1.2)x10^{14}$ cm^{-3}.

The temporal evolution of the atomic oxygen density was determined by TALIF and showed an increase of a factor 5 of the density after the discharge pulse. The peak measured O density, $1.5(0.8)x10^{18}$ cm^{-3}, represents about 50 % of dissociation of molecular oxygen. This large amount of O production can explain the beneficial role of the NRP discharge in the stabilization of flames.

In air, the characteristic time of $N_2(A,B,C)$ density decays were found to coincide with the characteristic time for atomic oxygen formation, which is about 30 ns after the discharge event. The temporal evolutions of the measured absolute densities thus validate that atomic oxygen production is the result of the assumed two-step mechanism.

In addition, the gas temperature was obtained using emission spectra of the nitrogen second positive system and CRDS absorption spectra of the nitrogen first positive system. We noticed a fast increase of the rotational temperature from 1600(200)K to 2600(400)K in about 30 ns. This fast increase of temperature can be clearly explained by the fast heat release due to the two-step mechanism.

Using electrical measurements, the energy deposited by discharge pulse was found to be 500(100) μJ. This energy mainly goes into the dissociation of O_2 via the two-step mechanism and into the gas heating. Based on an energy balance, we determined that 10 to 20% of the energy deposited per pulse goes into gas heating. Thus, in addition to oxygen radical production, the heat release by the discharge may also play a role in the flame stabilization mechanism.

The results obtained here open up new questions to be solved for further understanding of the NRP discharge kinetics and dynamics. Investigations of other key species produced by the discharge, such as atomic nitrogen, metastable oxygen $O(^1D)$, $O_2(^1\Delta)$, NO, etc, need to be conducted to clarify the role and reaction channels of these species. Regarding plasma-assisted combustion, other issues need to be solved such as: how the key species produced by the NRPD propagate and react in the combustion chamber, which are the pollutant species and how they are reduced by the presence of the NRP plasma.

References

N. L. Aleksandrov, S. V. Kindysheva, M. M. Nudnova and A. Yu. Starikovskiy Mechanism of ultra-fast heating in a non-equilibrium weakly ionized air discharge plasma in high electric fields Journal of Physics D: Applied Physics Volume 43, Number 25 30 June 2010.

N.L. Aleksandrov , F.I. Vysikailo, R. Islamov , I.V Kochetov , A.P. Napartovich and V.G. Pevgov ,1981 Sou. High Temp. Thermophys. 19 22-27; 485-9

R Arieli, stwww.weizmann.ac.il/Lasers/laserweb/Ch-4/C4s4t2p3.htm,"The Laser Adventure" Chapter 4 Section 4, page 14,

M. Asmann, D. Kolman, J. Heberlein and E. Pfender, Experimental confirmation of thermal plasma CVD of diamond with liquid feedstock injection model, Diamond Relat. Mater. 9. 2000.

S.E. Babayan, J. Jeong, A. Schu¨ tze, V.J. Tu, M. Moravej, G.S. Selwyn and R.F. Hicks, Deposition of silicon dioxide films with a non-equilibriumatmospheric-pressure plasma jet, Plasma Sources Sci. Technol. 10, 2001.

M Baeva, H Gier, A Pott, J Uhlenbusch, J Höschele and J Steinwandel, Pulsed microwave discharge at atmospheric pressure for NO_x decomposition, Plasma Sources Sci. Technol. 11, 2002.

D.J.Bamford ,L.E.Jusinski, and W.K;Bischel1986 *Phys. Rev.* A 34 185, 1986

K.H. Becker, M. Schmidt, A.A. Viggiano, R. Dressler, and S. Williams. Air plasma chemistry. In K.H. Becker,U. Kogelschatz, K.H. Schoenbach, and R.J. Barker, editors, Non-Equilibrium Air Plasmas at Atmospheric Pressure, pages 124–182. IoP, Bristol, 2005.

G. Berden, R. Peeters, and G. Meijer, Int. Rev. Phys. Chem. 19, 565, numéros de pages, 2000.

J. P. Borra, Nucleation and aerosol processing in atmospheric pressure electrical discharges: powders production, coatings and filtration, J. Phys. D: Appl. Phys. 39 (2006) R19–R54, 2006.

J. P. Boeuf, Topical review. Plasma display panels: physics, recent developments and key issues, J. Phys. D: Appl. Phys. 36 R53-R79, 2003.

M. Capitelli, C. M. Ferreira, B. F. Gordiets, A. I. Osipov. Plasma Kinetics in atmospheric Gases, Springer-Verlag, New York 2000

A. Chirokov, A. Gutsol, and A. Fridman, Atmospheric pressure plasma of dielectric barrier discharges, Pure Appl. Chem. 77; 487-495, 2005.

W. Demtroeder , Laser spectroscopy (3ed., Springer, 2003)(T)

P. Fauchais, Journée Technique sur les Traitements de Surfaces et leurs applications a` la mécanique, 15 Février 1996, Limoges, France, 1996.

N. Gherardi and F. Massines, Mechanisms controlling the transition from glow silent discharge to streamer discharge in nitrogen, IEEE Transactions on Plasma Science 29, 536-544,2001.

F.R. Gilmore, J. Quant. Spectr. And Rad. Transfer, 5, 369, 1965.

A. Goehlich, T. Kawetzki and H.F. Dobele 1998 J. Chem. Phys.108 9362–70. 1998.

V. Guerra V and J. Loureiro ,, Plasma Sources Sci. Technol. 373, 1997

A.Gutsol , G. Fridman, G. Friedma, M. Balasubramanian, M. Peddinghaus and A. Fridman Non-Thermal Plasma Blood Coagulation and Sterilization of SurfaceWounds. in 17th International Symposium on Plasma Chemistry. Toronto, Canada, 2005.

Z.B. Guzel-Seydim, A.K. Greene and A.C. Seydim, Use of ozone in the food industry, Lebensm.-Wiss. Technol. 37, 2004.

O. Ishihara, G.V. Candler, C.O. Laux, A.P. Napartovich, L.C. Pitchford, J.P. Boeuf, and J. Verboncoeur, "Chapter 5. Nonequilibrium Plasma Modeling", pp. 183-275, Non-Equilibrium Air Plasmas at Atmospheric Pressure, ed. K.H. Becker, U. Kogelschatz, K.H. Schoenbach, and R..J. Barker, Institute of Physics, Jan. 2005.

M. Janda, G. D. Stancu, T. G. Spence, C. Harb, F.Kaddouri, D. Pai, D.A. Lacoste and C. O. Laux, Measurements of $N_2(A)$ by pulsed cavity ring down spectroscopy in repetitively pulsed nanosecond discharges, XVII International Conference on Gas Discharges and their Applications, Cardiff, UK, September 7-12, p. 385-388 ,2008.

References

F. Kaddouri, G.D. Stancu, D.A. Lacoste, C.O. Laux, Investigation of atmospheric pressure nitrogen plasma by cavity ring-down spectroscopy, J. Phys.: Conf. Ser. 157, 012005, 2009

F. Kaddouri, G.D. Stancu, D.A. Lacoste, C.O. Laux, Investigation of atmospheric air pressure plasma by two-photon absorption laser induced fluorescence, 29-th ICPIG, Cancun, PA6-13 2009 Mexico

U. Kogelschatz, B. Eliasson, and W. Egli, From ozone generators to flat television screes: history and future potential of dielectric barrier discharges, Pure Appl. Chem. 71, 1819, 1999.

P. Kong, Atmospheric-pressure plasma generation, processes, and applications , SOHN International Symposium On Advanced Processing of Metals and Materials; Principles, Technologies and Industrial Practice, September 2006.

A. Kossyi, A. Yu Kostinsky, A.A. Matveyev and V.P. Silakov, Plasma Sources Sci. Techol., 1, 207, 1992.

C.H. Kruger, C.O. Laux, L. Yu, D.M. Packan, and L. Pierrot, Nonequilibrium discharges in air and nitrogen plasmas at atmospheric pressure Pure Appl. Chem., Vol. 74, No. 3, pp. 337–347, 2002

E. E. Kunhardt, Generation of large volume atmospheric pressure, non equilibrium plasma, IEEE Transactions on Plasma Science 28, 189-200, 2000.

C. O. Laux Thesis, Optical diagnostics and radiative emission of air plasmas, Stanford University, 1993

C. O. Laux, L. Yu, D. M. Packan, R. J. Gessman, L. Pierrot, C. H. Kruger and R. N. Zare, AIAA 99-3476, 30th PDL Conf., Norfolk, VA 1999.

C. O. Laux, T. G. Spence, C. H. Kruger; R. N. Zare, Plasma Sources Sci. Technol. , 12, 125, 2003

C O. Laux, G. Pilla, S Pancheshnyi, D Pai, L Caillault, D. A. Lacoste, A. Bourdon, and D Veynante , Plasma-Assisted Flame Ignition and Stabilization using Nanosecond Repetitively Pulsed Discharges, 60th Gaseous Electronics Conference Arlington, VA – October 2-5, 2007.

F. Leipold, A. Fateev, Y. Kusano, B. Stenum, and H. Bindslev, Reduction of NO in the exhaust gas by reaction with N radicals, Fuel Volume 85, Issues 10-11, 2006.

S. B. Leonov, D. A. Yarantsev, A. P Napartovich and I. V. Kochetov,"Plasma-Assisted Combustion of Gaseous Fuel in Supersonic Duct", IEEE Transactions on Plasma Science, Vol. 34, no. 6, pp. 2514-2525, 2006.

G. Lou, A. Bao, M. Nishihara, S. Keshav, Y.G. Utkin, J.W. Rich, W.R. Lempert, and I.V. Adamovich, Proceedings of the Combustion Institute, vol. 31, no. 2, January 2007.

Z. Machala, I. Jedlovský and V. Martišovitš, DC discharges in atmospheric air and their transitions, IEEE Trans. Plasma Sci. 36, 918-919, 2008.

Z. Machala, E. Marode, C.O. Laux, and C.H. Kruger, "DC Glow Discharges in Atmospheric Pressure Air," Journal of Advanced Oxidation Technologies, vol. 7, no. 2, pp. 133-137, 2004.

F. Massines et al, Experimental and theoretical study of a glow discharge at atmospheric pressure controlled by dielectric barrier, J. Appl. Phys. 83, 2950-2957, 1998.

E. Marode, D. Djermoune, P. Dessante, C. Deniset, P. Segur, F. Bastien, A. Bourdon and C. Laux, Physics and applications of atmospheric non-thermal air plasma with reference to environment, Plasma Phys. Control. Fusion 51 124002 , 2009.

I. Matveev, S. Matveeva and E. Kirchuk, Plasma Assisted Combustion Technologies, Proceedings of the European Combustion Meeting , 2009.

A. Mizuno, Industrial applications of atmospheric non-thermal plasma in environmental remediation, Plasma Phys. Control. Fusion Vol. 49, A1–A15, 2007.

M. Moravej, X. Yang, R. F. Hicks, J. Penelon and S.I. Babayan, A radio-frequency non- equilibrium atmospheric pressure plasma operating with argon and oxygen, Journal of Applied Physics 99, 093305, 2006.

M. Nagulapally, G. V. Candler, C. O. Laux, L. Yu, D.Packan, C. H. Kruger, R. Stark, and K.H. Schoenbach, Experiments and simulations of DC and pulsed discharge in air plasmas, 31st AIAA Plasma Dynamics and Lasers Conference, Denver, CO, USA, AIAA 2000-2417,2000.

V. Nehra, A. Kumar and H. K. Dwivedi, Atmospheric Non-Thermal Plasma Sources International Journal of Engineering, vol. 2,: no. 1, 2008.

K. Niemi , V. Schulz-von der Gathen and H.F. Dobele, J. Phys. D: Appl. Phys. 34 2330–5, 2001.

K Niemi, V Schulz-von der Gathen and H F Doebele, Absolute atomic oxygen density measurements by two-photon absorption laser-induced fluorescence spectroscopy in an RF-excited atmospheric pressure plasma jet, Plasma Sources Sci. Technol., Vol. 14, 375–386, 2005

D. Packan, Ph.D. Thesis, Stanford University, 2003.

D.Z. Pai, Nanosecond repetitively pulsed plasmas in preheated air at atmospheric pressure, PhD Thesis, Ecole Centrale Paris, Châtenay-Malabry, France, 2008.

D.Z. Pai, G.D. Stancu, D.A. Lacoste, and C.O. Laux, "Nanosecond Repetitively Pulsed Discharges in Air at Atmospheric Pressure-The Glow Regime," Plasma Sources Science & Technology, Vol. 18, No. 4, 045030, Nov. 2009.

D.Z. Pai, D.A. Lacoste, and C.O. Laux, 'Transitions between corona, glow, and spark regimes of nanosecond repetitively pulsed discharges in air at atmospheric pressure," J. Appl. Phys., 107, 093303, 2010a (15 p).

D.Z. Pai, D.A. Lacoste, and C.O. Laux, "Nanosecond repetitively pulsed discharges in air at atmospheric pressure – the spark regime," Plasma Sources Science and Technology, 19, 065015, 2010b .

Optronic Laboratories, Report of Calibration for One Standard of Spectral Radiance OL550.

S. Pancheshnyi, D A Lacoste, A Bourdon, and C O Laux, Ignition of propane–air mixtures by a repetitively pulsed nanosecond discharge, IEEE Transactions on Plasma Science, vol. 34, 2478-2487, 2006.

L. Peddinghaus, G. Fridman, T. Vinovrski, A. Jah, A. Fridman, M. Balasubramanian, A. Gutsol and G. Friedman, Use of Non-Thermal Atmospheric Pressure Plasma Discharge for Coagulation and Sterilization of Surface Wounds. in 32nd IEEE International Conference on Plasma Science, Monterey, CA, USA, 2005.

G. Pilla ; PhD thesis, Etude experimentale de la stabilisation de flammes propane-air de premelange par decharges nanosecondes impulsionnelles repetitives Ecole Centrale Paris, 2008

G. Pilla, D. Galley, D.A. Lacoste, F. Lacas, D. Veynante, and C.O. Laux, AIAA Paper 2006-3243, 37th AIAA Plasmadynamics and Lasers Conference, San Francisco, CA, 2006.

N. A. Popov, Investigation of the Mechanism for Rapid Heating of Nitrogenand Air in Gas Discharges, Plasma Physics Reports, Vol. 27, No. 10, pp. 886–896. Translated from Fizika Plazmy, Vol. 27, No. 10, 2001, pp. 940–950, 2001.

G.S. Selwyn, H.W. Herrmann, J. Park, and I. Henins, Materials Processing Using an Atmospheric Pressure, RF-Generated Plasma Source, Contrib. Plasma Phys. vol 6, 2001.

A. E. Siegman, Lasers, 1st ed. University Science, Sausalito, Calif. 1986.

S. Spuler and M. Linne, Numerical analysis of beam propagation in pulsed cavity ring-down spectroscopy, Applied Optics, Vol. 41, No. 15,. 2858-2868, 2002

G.D. Stancu, M. Janda, F. Kaddouri, D.A. Lacoste, and C.O. Laux, Time-Resolved CRDS Measurements of N2(A) Density Produced by Nanosecond Discharges in Atmospheric Pressure Nitrogen and Air, J. Phys. Chem. A, , Vol. 114, No. 1), 201-208, 2010.

G D Stancu, F. Kaddouri, D.A. Lacoste, and C.O. Laux, Atmospheric pressure plasma diagnostic by OES, CRDS and TALIF, J. Phys. D.: Appl. Phys., Vol. 43, 124002, 2010.

G.D. Stancu, F. Kaddouri, D.A. Lacoste, C.O. Laux, Investigations of the rapid plasma chemistry induced by nanosecond discharges in atmospheric pressure air using advanced optical diagnostics, AIAA, 40th Plasmadynamics and Lasers Conference, San Antonio TX, 3593, 2009 USA

G.D. Stancu, M. Janda, F. Kaddouri, D. Pai, D.A. Lacoste, J.C. Rolon, and C.O. Laux, Two photon absorption laser induced fluorescence study of repetitively pulsed nanosecond discharges in atmospheric pressure air**,** AIAA, 39th Plasmadynamics and Lasers Conference, Seattle, 3882, 2008 USA

S.M. Starikovskaia, "Plasma assisted ignition and combustion", J. Phys. D: Appl. Phys., 39, R265-299 2006

Y. Starikovskii, Proceedings of the Combustion Institute, vol. 30, 2405-2417, 2005.

C. Tendero, C. Tixier, P. Tristant, J. Desmaison and P. Leprince, Atmospheric pressure plasmas: A review, Spectrochimica Acta Part B, 61, 2006.

Udi M, Jiang N, Mintusov E, Adamovich I V and Lempert W R 2008 Proc. Comb. Inst. 32 929

A. P. Yalin and R. N. Zare, Effect of Laser Lineshape on the Quantitative Analysis of Cavity Ring-Down Signals, Laser physics, Vol. 12, No. 8, numéros de pages, 2002